R. König, A. Bode,
Z. Chen, L. Grunwaldt,
R. Neubert, Ch. Reigber,
P. Schwintzer

The GFZ-1 Mission:
Design, Operations and First Results

Scientific Technical Report STR96/09

H. König, A. Bode,
Z. Chen, L. Grunwaldt,
R. Neubert, Ch. Reigber,
P. Schwintzer

The GFZ-1 Mission:
Design, Operations and First Results

R. König, A. Bode,
Z. Chen, L. Grunwaldt,
R. Neubert, Ch. Reigber,
P. Schwintzer

The GFZ-1 Mission:
Design, Operations and First Results

Scientific Technical Report STR96/09

1. INTRODUCTION

Main objective of the GFZ-1 mission is the improvement of the knowledge of the Earth's gravity field. GFZ-1 was therefore launched into the lowest altitude orbit ever flown by geodetic satellites. The increased benefits of low altitude missions for gravity field restitution stand in contrast to the problems imposed by the increased impact of atmospheric drag which has to be carefully analyzed to separate the gravity signal. On the other hand GFZ-1 data may well be used to recover atmospheric density once the gravity impact can properly be modeled. So atmospheric model studies become naturally a side aspect of the mission objectives.

The GFZ-1 mission is a low budget, fast realization project. At costs of less than 1,000,000 DM GFZ-1 was designed, constructed, tested and launched within one year from signing the contract. On April 19, 1995, GFZ-1 was released into its orbit from the MIR space station. Meanwhile analyses gave proof of the suitability of the concept to fulfill the mission objectives. This booklet compiles the technical background beginning from the design phase and ending with the first promising results. The recent success of the mission is based on the emphasis of the people envolved from various institutions. The main contractor, the Kayser-Threde company in Munich, set the basis by sub-contracting the Russian Institute for Space Device Engineering RNIIKP for design, construction and test of GFZ-1 and by sub-contracting the Russian Space Cooperation RKK Energia for the launch. These days during nominal operation in particular the international SLR community supports the mission by putting increased efforts into GFZ-1 data acquisition. If these efforts can be maintained the GFZ-1 mission will meet and probably go beyond the anticipated scientific objectives.

1

2.   MISSION OBJECTIVES

2.1   Mission Frame

The scientific objective of improving Earth's gravity field models requires low altitude orbits at high inclination with an acceptable mission lifetime. The GFZ-1 realization fell in the time period when cheap transport opportunities were available on Russian launchers. The orbit injection via space station MIR led to an orbit at initially 400 km altitude. This fills a gap in the orbital altitude range of gravity suitable satellites. Before GFZ-1, satellite data exploited for gravity applications came from altitudes above 800 km. GFZ-1's inclination of 51.6° being set by the MIR orbit can be viewed as a medium high inclination which leads to some degradation of sensitiveness of GFZ-1 to gravity constituents at zonal and some higher degree, tesseral harmonics of the spherical expansion.

GFZ-1 is a simple, passive laser reflector satellite. The one and only tracking source is the existing international SLR network. GFZ participates in running an own SLR station in Potsdam and in supporting the station in Santiago de Cuba. With a probable mission lifetime of about 4 years, it should be possible to gather a set of laser range data that effectively enables the recovery of new specific resonant regions in the gravitational spectrum.

It can be assumed that the GFZ-1 mission was highly welcomed in the scientific community. Dedicated gravity field missions were repeatedly requested by national and international resolutions. However gravity mission studies as f.i. ARISTOTELES have never envolved to reality and planned missions as f.i. STEP will not be realized before the year 2000. Therefore GFZ-1 fills also a gap in the timely domain of satellite gravity missions.

Some years of experience in mission management was gained at GFZ in the frame of the ERS-1 mission and other missions. GFZ exploited these fact to realize the GFZ-1 project in the design, launch and nominal operation phase. The experience and the capabilities in gravity recovery available at GFZ generated the idea for the GFZ-1 project and are the basis for the scientific exploitation where of course the international scientific community is asked to participate.

2.2   Gravity Regimes

From an initial altitude of appr. 390 km after the launch in April 1995, the altitude of the satellite will slowly decay. During the expected lifetime of 4 years the satellite moves through various resonance regimes of the gravity field. Recent gravity field models derived from satellite orbit perturbations are known to appr. degree/order 30 of a spherical harmonic expansion of the gravitational potential, plus some distinct information within certain resonant orders. This can be seen in Figure 2.2.1 where the maximum orbit perturbations due to the geopotential (linear perturbations following *Kaula* [1966]) for ERS-1 are depicted. The satellite with the lowest altitude currently being included in gravity field solutions is ERS-1 at an altitude of appr. 800 km.

2
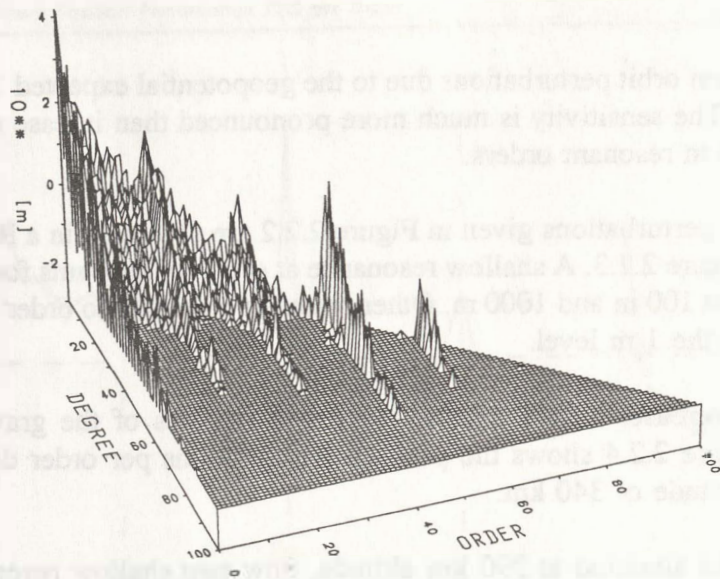
ERS-1 (a=7165.0 km, e=.0014, i=98.50 deg)

Figure 2.2.1: ERS-1 Sensitivity to Gravity
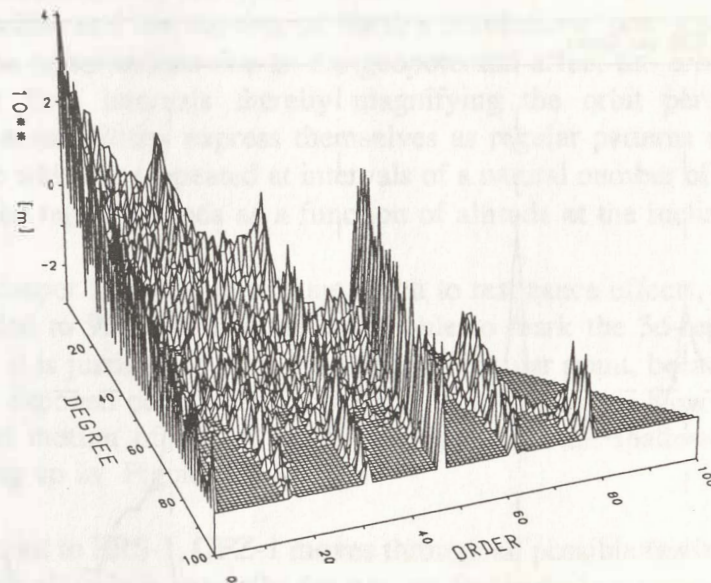
GFZ-1 (a=6768.0 km, e=.0010, i=51.60 deg)

Figure 2.2.2: GFZ-1 Sensitivity to Gravity at 390 km Altitude

3

Figure 2.2.2 tells the maximum orbit perturbations due to the geopotential expected for GFZ-1 at an altitude of 390 km. The sensitivity is much more pronounced than in case of ERS-1 and comes up to degree 100 in resonant orders.

The maximum orbit position perturbations given in Figure 2.2.2 are compiled in a RSS value per order and displayed in Figure 2.2.3. A shallow resonance at order 46 accounts for position perturbations ranging between 100 m and 1000 m. Other resonant orders up to order 77 imply position perturbations above the 1 m level.

As the altitude of GFZ-1 decreases with time, the resonance regimes of the gravity field change accordingly. F.i. Figure 2.2.4 shows the position perturbations per order due to the gravity field impact at an altitude of 340 km.

In comparison to the previous situation at 390 km altitude, now two shallow resonances at orders 31 an 62 show up. Other resonant orders causing orbit perturbations of minimum 1 m can be found up to order 78. So as the altitude of GFZ-1 decreases, its sensitivity to the gravity field increases.

Also a slight change of the resonant orders with decreasing altitude can be noticed. The reason being the fact that resonant order numbers can be found close to multiples of the values of the mean motion of the satellite. During the mission GFZ-1 will increase its mean motion from appr. 15.5 rev/d to nearly 16 rev/d.
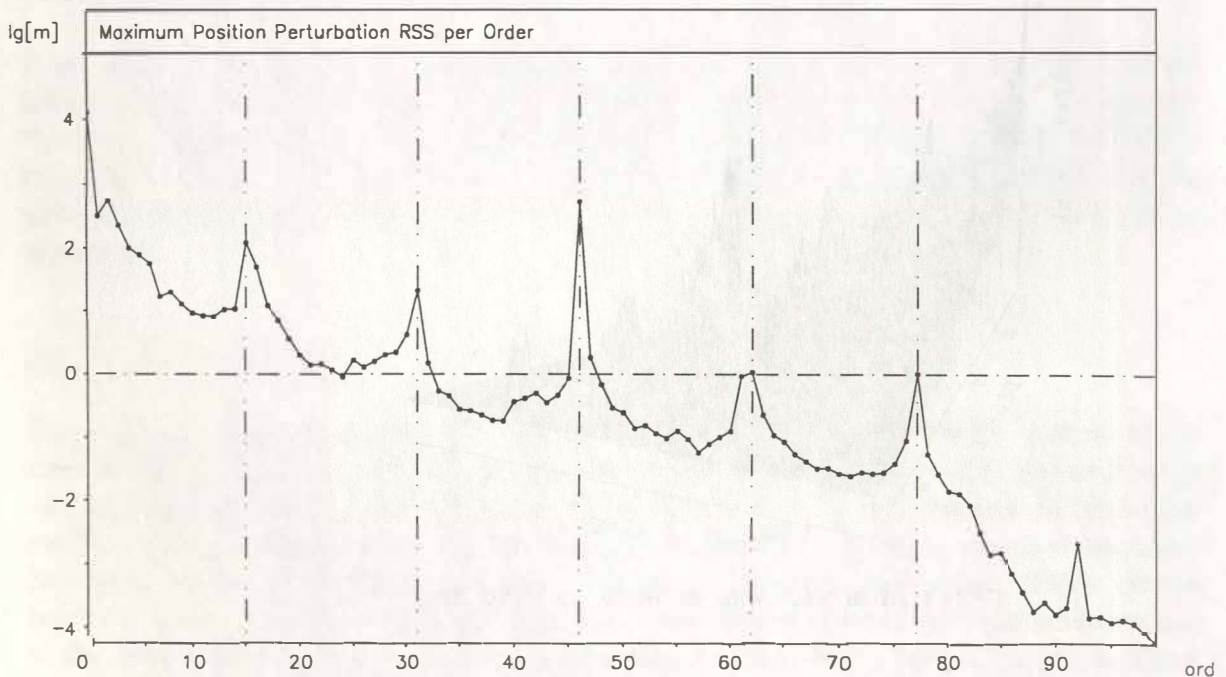
Figure 2.2.3: GFZ-1 Orbit Perturbations per Order at 390 km Altitude

4
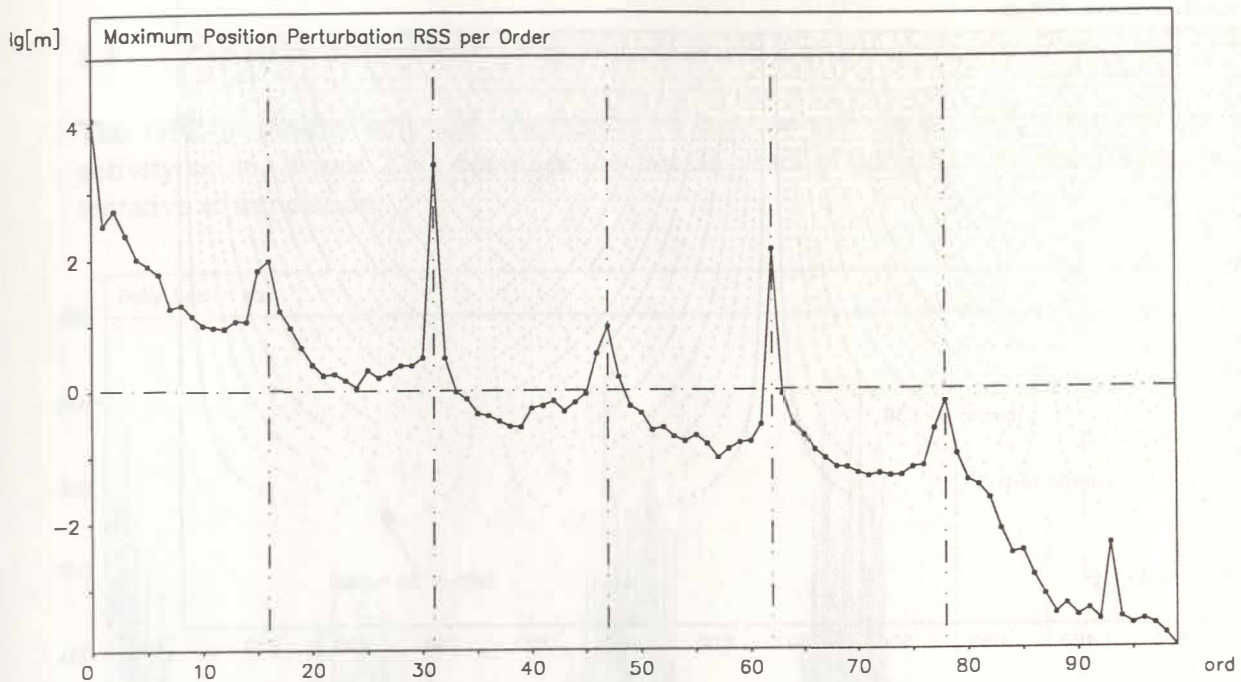
Figure 2.2.4: GFZ-1 Orbit Perturbations per Order at 340 km Altitude

A quite instructive picture of shallow resonances that can be expected, may be gained from a commensurability analysis. Commensurabilities occur when the number of revolutions of the satellite and the number of Earth's revolutions form a ratio of natural numbers. In this case the perturbations due to the geopotential affect the orbit at the same place in space at regular time intervals thereby magnifying the orbit perturbations in a resonant way. Commensurabilities express themselves as regular patterns of ground tracks on the Earth's surface which are repeated at intervals of a natural number of days. Figure 2.2.5 depicts these so-called repeat periods as a function of altitude at the inclination of GFZ-1.

For a deeper insight into this approach to resonance effects, the altitude axis in Fig. 2.2.5 is expanded to 900 km in order to be able to mark the 3d-repeat orbit of ERS-1. In case of ERS-1 it is justified to pick out just this singular point, because the orbit is forced to remain in this exponed condition by timely orbit manoeuvers. Now see that the 3d-repeat cycle at a mean motion of 14 1/3 rev/d accounts for the shallow resonance at order 43 clearly showing up in Figure 2.2.1.

In contrast to ERS-1, GFZ-1 moves through all possible (an infinite number of) repeat periods while its altitude is naturally decreasing. Particularly interesting becomes the mission, where the altitudes imply small repeat periods. There orbit perturbations due to resonant orders at appr.

$$N\text{-}d \; repeat \; cycle \times mean \; motion \qquad\qquad 2.2.1$$

can be expected. Table 2.2.1 compiles the main repeat cycles together with the adjacent altitudes and mean motions.

5
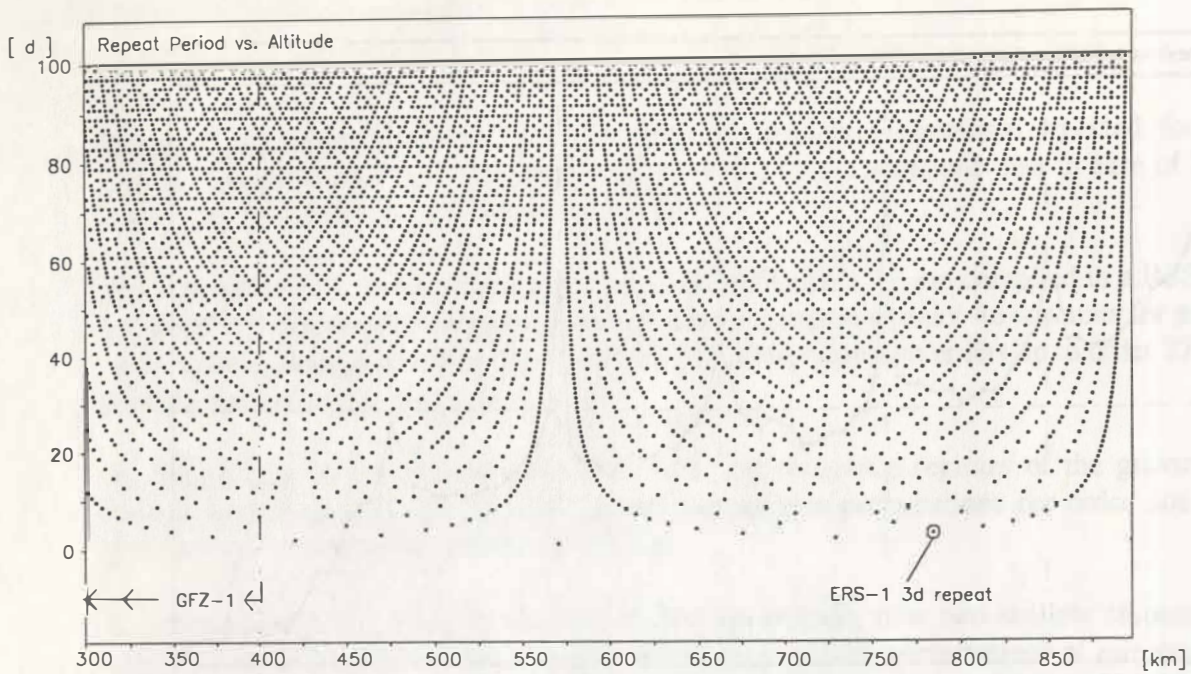
Figure 2.2.5: Commensurabilities at GFZ-1 Inclination

Table 2.2.1: GFZ-1 Repeat Cycles

Repeat Cycle (d)	Altitude (km)	Mean Motion (rev/d)
3	372.116	15.6544
4	348.311	15.7376
5	334.127	15.7875
6	324.714	15.8207
7	358.487	15.7019
7	318.009	15.8445
8	312.993	15.8623
8	384.098	15.6128
9	340.421	15.7653
9	309.097	15.8762
10	305.985	15.8873
10	362.568	15.6877

Concluding the above, GFZ-1 will be sensitive to the gravitational geopotential up to degree 100 and more in certain orders of the spherical harmonic expansion. Various shallow resonances can be expected at interesting orders of appr. $N \times 15.7$ (where $N=1...i$, $i_{max} \approx 8$).

6

The GFZ-1 lifetime will span the period of the low and the ascending part of the solar activity cycle. Figure 2.3.1 compiles the last 36 years of solar flux values together with a tentative extrapolation.
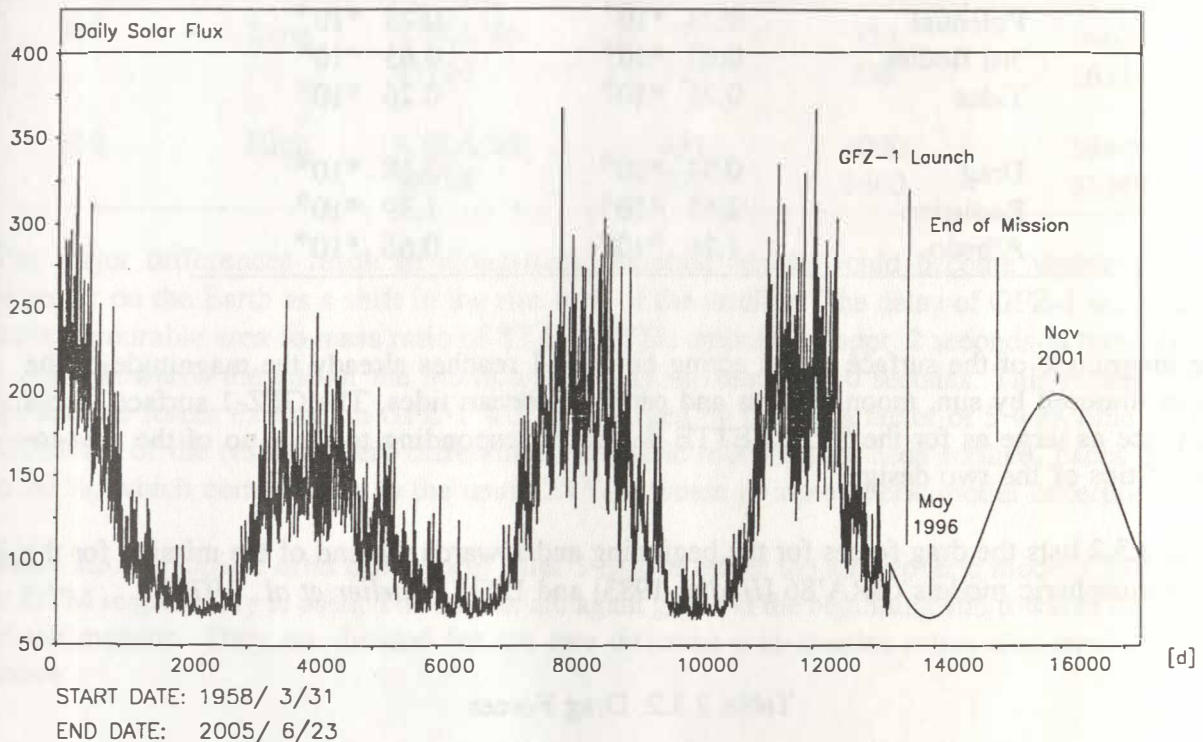
Figure 2.3.1: Solar Flux since 1958 Extrapolated until 2005

At the beginning of the mission, when GFZ-1 obeys its highest altitude, the solar activity is low. In the following years the solar activity will increase whereas the altitude of the satellite will decrease. The two facts will multiply the impact of the surface forces, because high solar activity causes high atmospheric density and because decreasing altitude of the satellite comes along with increasing density of the atmosphere. Therefore the precise orbit determination and gravity field solution process will become more difficult in the course of the mission, though the gravity field models will continuosly be improved and though better atmospheric models may be available later on.

A look at probable conservative and non-conservative forces acting on GFZ-1 may provide a feeling for the physical impacts the satellite will experience. Table 2.3.1 lists some physical forces at an altitude of 400 km during the period of low solar activity i.e. at the beginning of the mission. In order to relate the numbers to an accustomed mission, an additional column is added where the orbital and solar activity characteristics are kept identical to the above, but the area-to-mass ratio (A/M) is taken according to that of the STARLETTE satellite. The area-to-mass ratio of GFZ-1 is 0.00176 m^2/kg, that one of STARLETTE is 0.00096 m^2/kg.

7

Table 2.3.1: Various Forces at One Instant

Source	Acceleration (m/s^2)	
	GFZ-1	A/M STARLETTE
Potential	0.23 $*10^{-3}$	0.23 $*10^{-3}$
3rd Bodies	0.65 $*10^{-6}$	0.65 $*10^{-6}$
Tides	0.26 $*10^{-6}$	0.26 $*10^{-6}$
Drag	0.34 $*10^{-6}$	0.18 $*10^{-6}$
Radiation	2.65 $*10^{-9}$	1.39 $*10^{-9}$
Albedo	1.26 $*10^{-9}$	0.66 $*10^{-9}$

The magnitude of the surface forces acting on GFZ-1 reaches already the magnitude of the forces imposed by sun, moon, planets and earth and ocean tides. The GFZ-1 surface forces are twice as large as for the STARLETTE design corresponding to the ratio of the area-to-mass ratios of the two designs.

Table 2.3.2 lists the drag forces for the beginning and towards the end of the mission for the two atmospheric models CIRA'86 [*Hedin,* 1983] and DTM [*Barlier et al.,* 1978].

Table 2.3.2: Drag Forces

Altitude (km)	Solar Activity	Acceleration (m/s^2)	
		CIRA'86	DTM
400	Low	0.34 $*10^{-6}$	0.30 $*10^{-6}$
350	High	1.52 $*10^{-6}$	1.57 $*10^{-6}$

Towards the end of the mission the drag forces will be 5 times as large as at the beginning. The difference of the two atmospheric models amounts to 3 to 10 % only, though atmospheric model uncertainties are commonly sized up to 25 %. In order to study the effects of different area-to-mass ratios, Table 2.3.3 compiles orbit differences after 3 days if area-to-mass ratios of either GFZ-1 or of STARLETTE are used for orbit modelling. The results are given at the beginning and towards the end of the mission and for the two atmospheric models introduced already above.

8

Table 2.3.3: Area-to-Mass Ratio Effects

Altitude (km)	Solar Activity	Atmospheric Model	Orbit Differences due to Area-to-Mass Ratios		
			Radial (m)	Cross-track (m)	Along-track (m)
400	Low	CIRA'86	97	754	14677
		DTM	113	838	16313
350	High	CIRA'86	551	3000	59449
		DTM	722	3600	71349

The major differences result in along-track direction which would become visible to an observer on the Earth as a shift in the rise time of the satellite. The delay of GFZ-1 w.r.t. the more favourable area-to-mass ratio of STARLETTE amounts to appr. 2 seconds in time after 3 days. Towards the end of the mission the delay increases to 10 seconds. This means that the surface forces exerted on GFZ-1 will be enlarged by at least a factor of 5 with time. The difference of the results where different atmospheric models have been applied, paces at 10 to 20 %, which comes close to the usual 25 % estimate of atmospheric model uncertainties.

Table 2.3.4 compiles orbit differences after 3 days if either the atmospheric model CIRA'86 or DTM respectively is used. The results are again given at the beginning and towards the end of the mission. They are divided for the two different area-to-mass ratios also used in the above.

Table 2.3.4: Atmospheric Model Effects

Altitude (km)	Solar Activity	Area-to-Mass Ratio	Orbit Differences due to Atm. Models		
			Radial (m)	Cross-track (m)	Along-track (m)
400	Low	STARLETTE	15	94	1821
		GFZ-1	28	178	3458
350	High	STARLETTE	86	664	13168
		GFZ-1	186	1263	25070

Again it can be seen that GFZ-1 is influenced twice as much as in case of a STARLETTE-like area-to-mass ratio. Within the lifetime of GFZ-1, the influence of the atmosphere increases by nearly a factor of 10. The considerable differences of the orbits demonstrate the uncertainties of the two atmospheric models.

The inherent errors of atmospheric models can only be accounted for by a proper selection of the parameters solved for in the precise orbit determination task. The optimal parametrization of the least squares problem and the impacts of data availablity are discussed later on in chapter 5.

9

3.   TECHNICAL DESCRIPTION OF THE SATELLITE

3.1   Basic Characteristics

Following approved satellite designs already in orbit as the passive laser satellites LAGEOS, STARLETTE and STELLA, it was decided to give GFZ-1 a spherical shape with laser retro-reflectors distributed regularly over its surface. The size of the satellite was restricted by the dimensions of the airlock in space station MIR to a maximum of 300 mm in diameter. The mass was limited to 20...30 kg in order to keep launch costs low. The most stringent demand on the satellite design was to find an optimum area-to-mass ratio minimizing orbit perturbation by atmospheric drag. The flight model finally built, comprises the following technical characteristics:

-    massive satellite body made from bronze
-    mass 20.630 ± 0.002 kg
-    diameter 215 ± 0.1 mm
-    60 retro-reflectors
-    CoM 58.5 ± 1 mm

A picture of GFZ-1 is given in Figure 3.1.1. The design and properties of the reflector array and the CoM problematic is discussed in more detail in chapter 3.2.
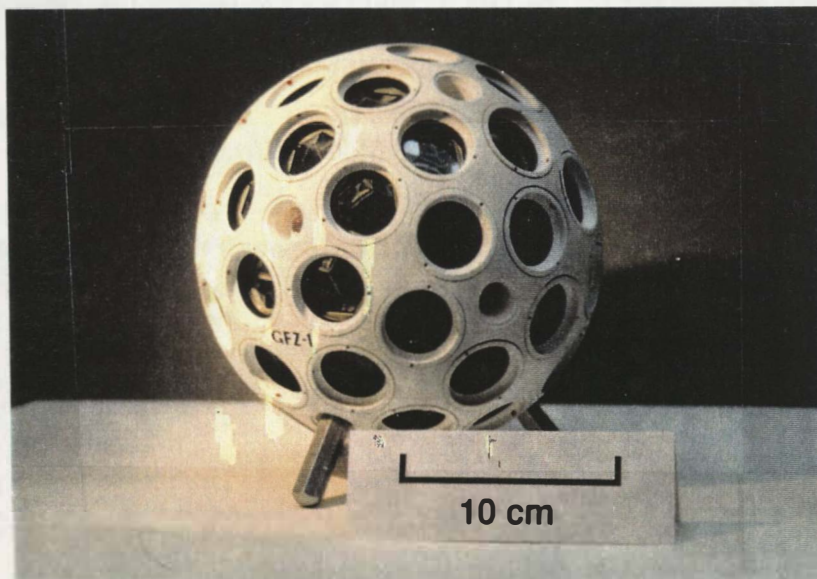
Figure 3.1.1 Picture of GFZ-1

The scientific objective of the mission to improve the accuracy and the resolution of Earth's gravity field models, requires a low altitude orbit at high inclination. The low cost launch opportunity from space station MIR implied a near circular orbit with an initial altitude of appr. 400 km at medium inclination. With an anticipated launch date at the beginning of 1995, the lifetime of GFZ-1 was estimated and displayed graphically as decay of the orbital altitude in Figure 3.1.2. Also the altitude decays under pessimistic and optimistic assumptions

10

on the solar activity are given (see Figure 2.3.1 for examples of low and high solar activity cycles). All in all the life of GFZ-1 will last between 3,5 and 5 years.

GFZ-1 was finally launched from space station MIR on April 19, 19:12 UTC, 1995. A detailed description of the launch scenario follows in chapter 4.2. The orbital parameters of the initial state in space are compiled in Table 3.1.1.

Altitude (km)
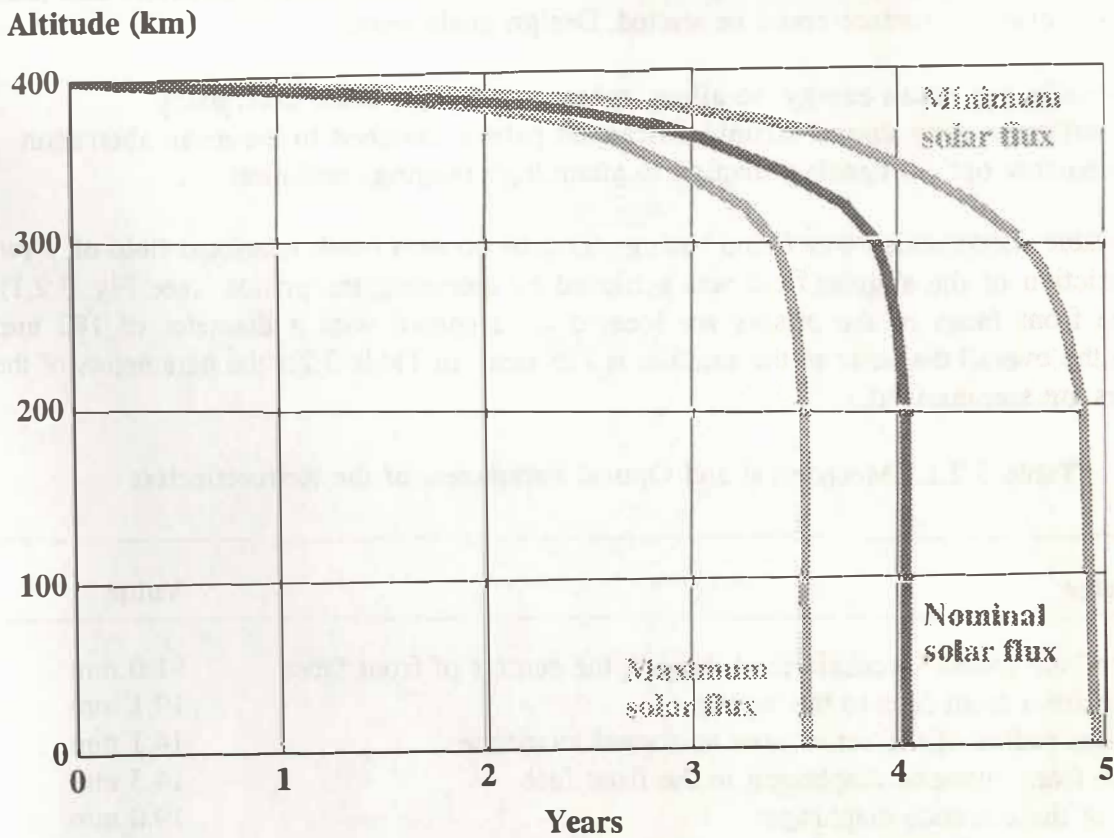
Figure 3.1.2 Lifetime Estimate

Table 3.1.1 Initial Orbital Elements

Element	Brouwer Mean Value
Semi-major axis	6767.67100 km
Eccentricity	0.00063
nclination	51.64853 deg
Perigee	65.76974 deg
Ascending node	90.18861 deg
Mean anomaly	230.71454 deg

11

The retroreflectors were made using standard cube corner prisms and holders which are already used for several successful missions, among others for the ETALON, METEOR-3 and the GPS-35/36 satellites. After the main decisions on the satellite overall diameter, material (mass) were made, the optimization procedure to find the number of reflectors and their distribution over the surface could be started. Design goals were:

- sufficient return energy to allow ranging with high beam divergency
- efficient ring-shaped farfield diffraction pattern matched to the mean aberration
- narrow optical transfer function to attain high ranging resolution

A reasonable compromise was found using 60 cube corners with restricted field of view. The restriction of the angular field was achieved by recessing the prisms (see Fig. 3.2.1). Thus the front faces of the prisms are located on a sphere with a diameter of 182 mm whereas the overall diameter of the satellite is 215 mm. In Table 3.2.1 the parameters of the reflectors are summarized.

Table 3.2.1:   Mechanical and Optical Parameters of the Retroreflectors

Parameter	Value
Radius of the sphere circumscribed through the centers of front faces	91.0 mm
Distance from front face to the vertex	19.1 mm
Equivalent radius of the active area at normal incidence	14.1 mm
Distance from entrance diaphragm to the front face	14.5 mm
Radius of the entrance diaphragm	19.0 mm
Coating of the reflecting surfaces	aluminum
Prism material	fused quartz
Refractive index @ 532 nm wavelength	1.4607

Because of velocity aberration, the beam of a perfect retroreflector is not precisely directed to the laser station on ground. It is deflected sligthly in the direction of the satellite movement. For GFZ-1 the aberration angle is variing between 4.9 and 10.5 arcseconds. Thus it would be ideal if the reflection pattern on ground would be ring-shaped with inner diameter of 4.9" and outer diameter of 10.5". Such a pattern was approximated in the following way: From a large number of cube corners samples were selected showing a two-spot far field with a splitting close to the average aberration angle of 7.7". These prisms were arranged in triads on the surface of the satellite as illustrated in Fig. 3.2.2 . The individual prisms of each triade are oriented in such a way that a six-spot reflection pattern is formed as shown in Fig. 3.2.2. The whole reflector array is formed by 20 triads arranged on the faces of a hypothetical icosaeder. In practice, the reflection patterns of the individual cube corners are more complicated as shown in Fig. 3.2.2. This results in a nonzero intensity in the centre of the pattern of the array.

12

Retroreflector – 60 pcs

Fixation Hole
– 12 pcs

38

14,5

91

215

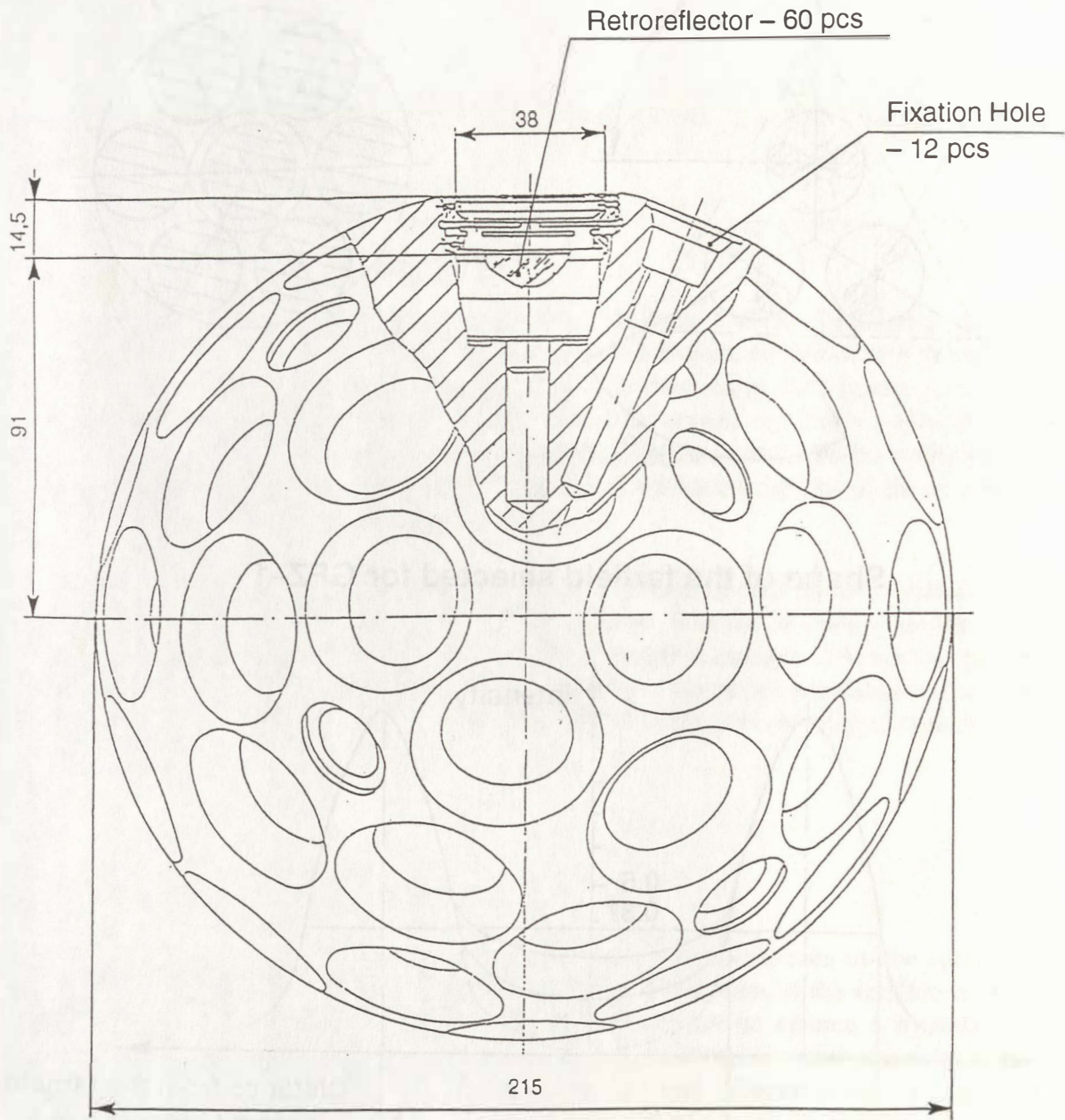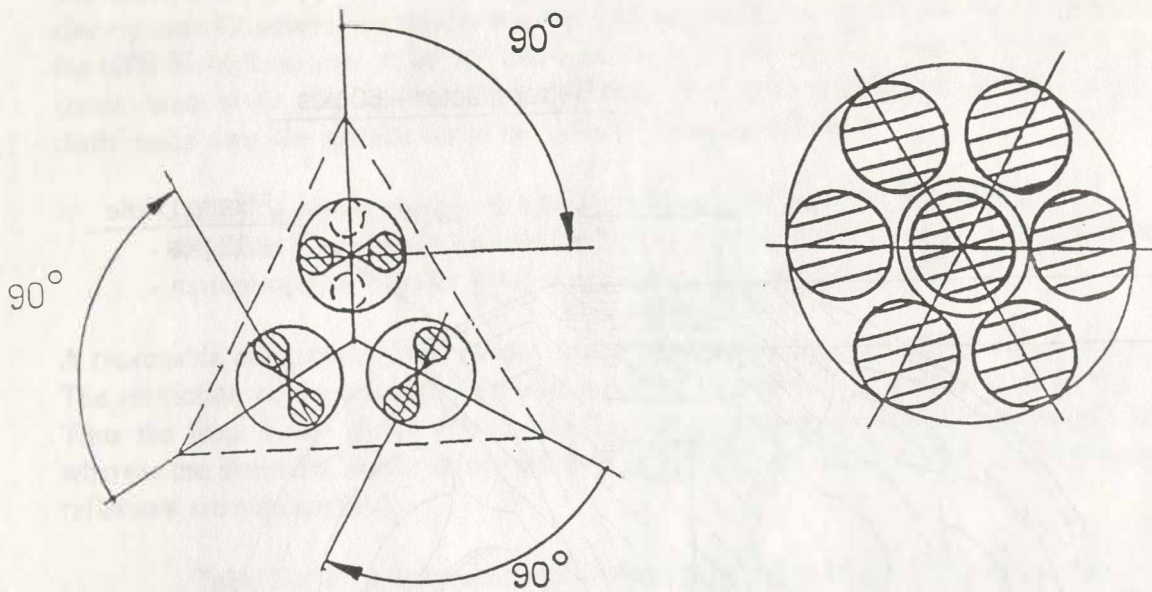Figure 3.2.1: Drawing of the GFZ-1 Satellite

13

Orientation of the reflection patterns in a triad

Resulting reflection pattern of a triad

90°

90°

90°

Shape of the farfield selected for GFZ-1

Intensity

1

0.5
0.37

Distance from the farfield centre (arcseconds)
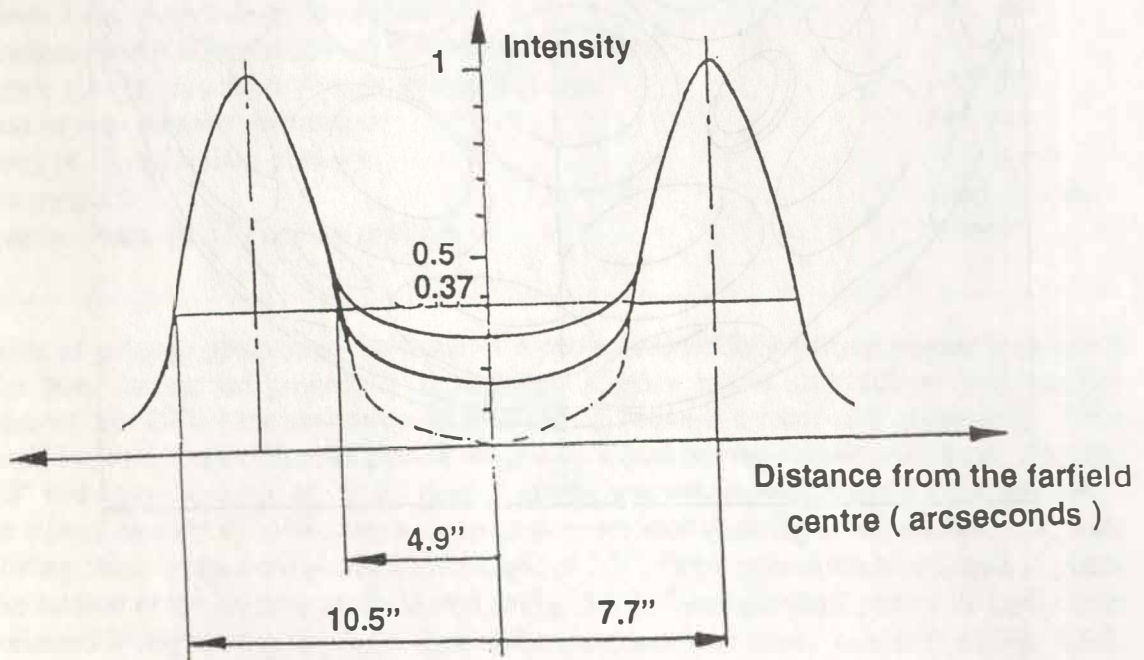
4.9"

10.5"

7.7"

Figure 3.3.2: Formation of the Farfield Diffraction Pattern

14

It was expected that the satellite is rotating in space. Therefore the reflection pattern is changing in time and the number of photons received may vary by a factor of 10 or even more. The changing reflection pattern was tested in the laboratory using a special setup based on a TV system with high angular resolution. It turned out that the average reflection pattern is in qualitative agreement with the theoretical expectation if 3 prisms are contributing. For the two remaining illumination possibilities of 4 and 5 prisms, the following results were obtained:

- 4 prisms : cross-shaped reflection pattern with highest energy density in the inner portions of the field, but with sufficient energy even in the outer regions close to the 10.5" aberration limit.

- 5 prisms : ring-shaped reflection pattern in analogy to the pattern for a triad, but with more homogeneous energy distribution.

In all possible cases (variants with less than 3 or more than 5 prisms illuminated at the same time are not possible due to the small diameter and the selected prism arrangement of the satellite) a sufficient amount of energy for signal detection using wide beams is contained in the ring-shaped area between 4.9" and 10.5" which represents the lower and upper limit of aberration for a satellite orbiting at 400 km altitude. For more details on the reflection pattern including the possibility of a partial compensation of the aberration due to the Fizzeau effect the reader is referred to [*Shargorodsky*, 1995a].

The individual cube corner reflectors were tested to maintain their optical parameters in a vacuum chamber under illumination by a sun simulator. It could be shown that the reflection pattern changed only slightly even during fast temperature changes. The optical parameters of the whole satellite were remeasured after applying mechanical vibrations in the range 20 ... 200 Hz using a spectral density of acceleration of 0.02 g/Hz. No significant change has been detected.

3.3 The Centre of Mass Correction

The laser ranging measurements primarily refer to the active reflectors on the surface of the satellite but for orbital analysis the distance to the centre of mass of the satellite is required. The necessary correction can be determined as follows: Let us assume a hypothetic point reflector in the centre of mass and regard the range measurements which this reflector would produce. The difference to the range produced by the real reflector array is equal to the required correction. This CoM is depending on the orientation of the satellite and therefore changing from shot to shot. In our case of a spherical (rotating) satellite the orientation cannot be predicted. Therefore the orientation is regarded as fully random and some average CoM is applied to each range. This is a good approximation because the existing SLR stations produce a large amount of measurements which are averaged within agreed time windows to produce "normal points". Therefore it can be expected that the orientation dependent effects are averaging out.

15

The calculation of the average CoM has been attacked in two ways:

1. Simulation of the whole ranging process including all effects influencing the return signal (satellite orientation, coherent interference, atmosheric effects, detection process...). The average CoM is determined from a large number of simulated ranges [*Egger*, 1995].

2. Modelling the average optical transfer function analytically [*Neubert*, 1994].

In addition the manufacturer calculated the CoM but did not describe the method used for the computation. The results of all three aproaches agree reasonably well as can be seen from Table 3.3.1.

Table 3.3.1: Centre of Mass Corrections (centroid of reflection)

Method [Source]	Centre of Mass Correction (mm)
Simulation [Egger]	58.5 ± 0.5 *)
Analytical Model [Neubert]	59.9 ± 2.0 *)
Manufacturer [Shargorodsky]	58.2 ± 3.7
Official value	58.5 ± 1.0

*)   the centroid of reflection is defined as the centre of gravity of the optical signals from the individual cube corners averaged over all orientations. This is the quantity computed by the analytical method. CoM values including shifts caused by the detection are reported in chapter 3.3.1. Note that in the simulations a preliminary value for the entrance diameter (39mm) was used .

Basic relation for any method to calculate the centre of mass is the following Eq. 3.3.1, describing the location of the effective plane of reflection of an individual cube corner reflector [*Arnold*, 1978]. In this formula $x(\alpha)$ is the distance from the satellite centre along the line of sight to the effective reflection plane, α is the angle of incidence of the laser beam, Rs is the radius from the satellite centre to the front face, L is the distance from the front face to the vertex of the cube corner and n is the refractive index of the cube corner material (fused quarz) at the laser wavelength.

$$x(\alpha)=Rs \cos \alpha -L\sqrt{n^2-\sin^2\alpha}$$

3.3.1

If more than one cube corner is contributing to the signal, then their relative intensity factors are required to compute the transfer function of the array. The signal at the receiver is a superposition of the reflections from the individual cube corners. It depends on the shape of the laser pulse, the orientation of each reflector, the relative intensities and phases, velocity aberration and atmospheric disturbances. All these effects are modelled in the simulations.

16

The relative phases are taken as fully random. For each simulated realization, the location of centroid is calculated. The centroid given in Table 3.3.1 is the average of a large number of realizations. The advantage of this method is, that it gives a representation of the fluctuations caused by coherent interference.

It can be shown that for unformly distributed phases the expectation value of the centroid is the same as for incoherent treatment of the superposition. This is used by the analytical model. The averaging over all orientations of the satellite is represented in the model by [*Neubert*, 1994] :

$$CoM = \int_0^{\alpha_c} x(\alpha) \ I(\alpha) \ \sin\alpha \ d\alpha$$

3.3.2

In Eq. 3.3.2 $I(\alpha)$ represents the intensity function of an individual cube corner. In general the reflectivity of a cube corner depends on the angle of incidence and the azimuth, especially for uncoated prisms. In our case we have metal coated prisms with circular entrance aperture which show negligible azimuth dependence. $\sin(\alpha)d\alpha$ represents the surface element on the unit sphere and α_c is the cutoff angle where $I(\alpha)$ becomes zero.

The intensity function $I(\alpha)$ is determined mainly by the angular dependence of the active area of a cube corner prism. It can be calculated using the methods given in [*Arnold*, 1978]. Taking into account the shadowing caused by the recession of the prisms the results represented in Fig. 3.3.1 are obtained. This active area function is a basic input for the simulations as well as for the analytical method. The intensity at the observer is furthermore influenced by diffraction. The active area becomes smaller with increasing angle of incidence. This causes an increase of the reflected beam divergency as a result of diffraction. In the simulations this is modelled in the following way: the active area is replaced by a circle of equal size to take advantage of the well known simple equation for the farfield diffraction pattern. For a given simulated pass, the velocity aberration is known for each moment. It determines the location of the observer in the farfield of each contributing prism. In the analytical calculation the effect of diffraction is taken into account approximately using the fact that the intensity in the centre of the far field is itself proportional to the area of the diaphragm. Thus the intensity function is taken to be the square of the active area and then normalized at zero angle.

17
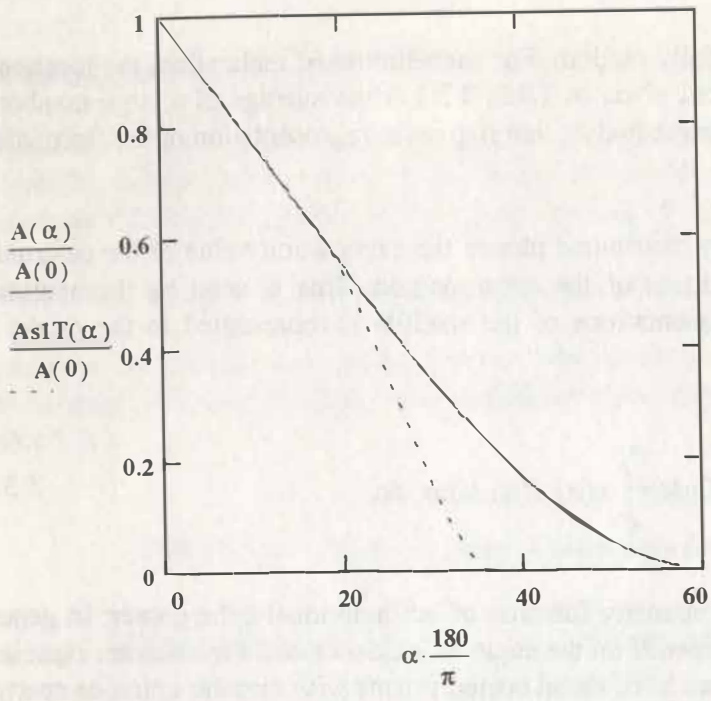
Figure 3.3.1: Dependence of the Active Reflecting Area of a Single Prism from the Angle of Incidence. Upper curve: no recession. Lower curve: recession and reflection loss included
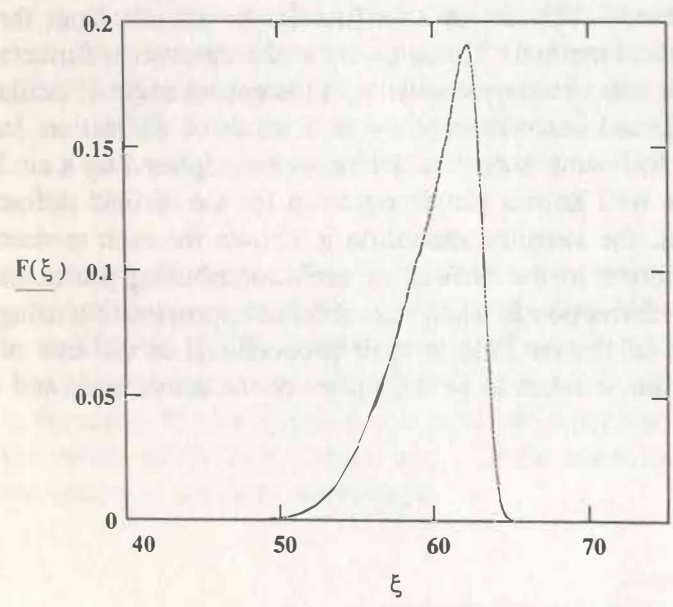
Figure 3.3.2: Optical Transfer Function of the GFZ-1 Satellite for 10 ps Laser Pulse
ξ: Distance from Satellite Centre (mm)

18

3.3.1 Results of Simulations [Egger, 1995]

The simulated measurements were generated for 3 hypothetic passes with maximum elevations of 55°, 75° and nearly 90°. The widths of gaussian laser pulses were assumed to be 10, 30, 50 and 100 ps (FWHM) respectively. The simulation includes the statistical behaviour of the photomultiplier detector as well as the limited bandwidth of the electronic amplifier. It is assumed that the impulse response of the amplifier is gaussian. The overall bandwidth is set to 2 GHz except for the station with 10 ps laser, where 10 GHz bandwidth has been assumed. Triggering at half maximum of the received signal has been assumed throughout. For each pass and laser pulse length about 180 measurements were generated from which the mean and standard deviation was obtained. The results are summarized in the following Tables.

The different signal types can shortly be explained as follows:

- *"optical signal"* means that only the incoming optical signal shape as the result of the reflection pattern (in the coherent case including superposition effects of the laser light reflected from different prisms, in the incoherent case without these effects) plus an "optical" half-amplitude triggering is taken into account for the CoM determination; the practical realization of this case would require an "ideal" detection system with rise time much shorter than the duration of the return pulse;

- *"electronic signal"* includes the quantum processes during signal detection using a photodetector (PMT or MCP) with a follow-on discriminator leading to a change of the shape of the incoming optical signal during the transformation process into an electronic signal; this case is valid for most of the NASA stations;

- *"single photoelectron"* regards the case that the level of the return signal is below one average photoelectron and an appropriate detector (usually an APD) is used; this case is valid for several EUROLAS stations (Graz, Herstmonceux).

Example realizations of signals for the 10 ps laser are reproduced in Fig. 3.3.3 and a full simulation run is represented in Fig. 3.3.4.

19

Table 3.3.2: CoM values obtained by simulation. Incoherent case

Signal Type	Laser pulse width (ps)	Mean CoM (mm)	Standard deviation (mm)
optical signal	10	61.7	1.0
	30	60.7	1.3
	50	60.2	1.2
	100	59.2	0.8
electronic signal	10	60.4	1.5
	30	58.8	1.7
	50	58.3	2.7
	100	58.3	2.3
single photon	10	59.4	3.1
	30	59.0	3.6
	50	58.8	4.3
	100	56.6	7.1

Table 3.3.3: CoM values obtained by simulation. Coherent case

Signal Type	Laser pulse width (ps)	Mean CoM (mm)	Standard deviation (mm)
optical signal	10	61.0	1.7
	30	58.7	2.1
	50	57.9	2.2
	100	55.6	3.4
electronic signal	10	60.3	1.5
	30	58.7	2.0
	50	58.5	3.1
	100	58.3	2.5
single photon	10	59.1	3.1
	30	58.3	3.5
	50	58.4	4.6
	100	57.3	7.2

20
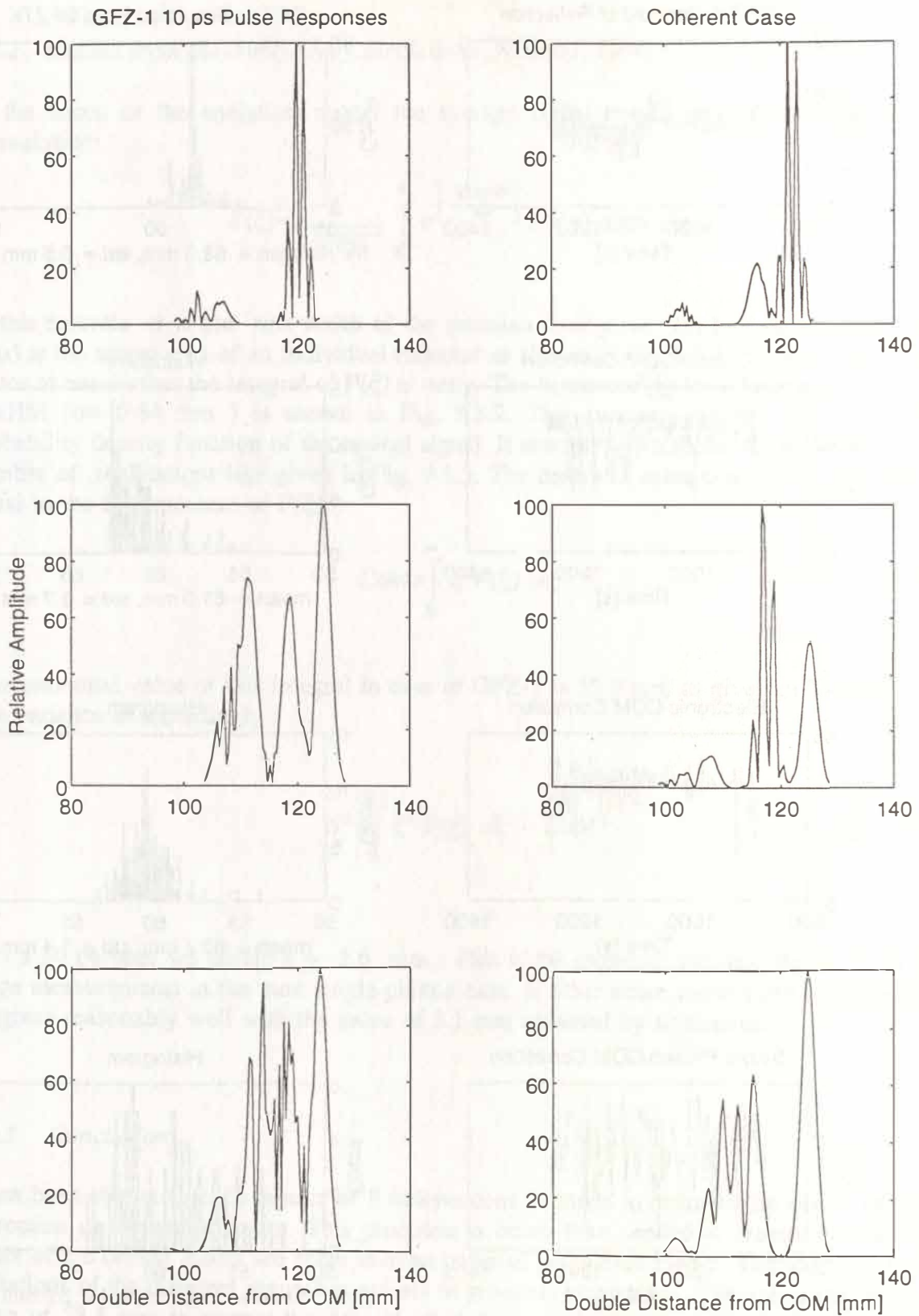
Figure 3.3.3: 10 ps Pulse Responses (coherent case)

21
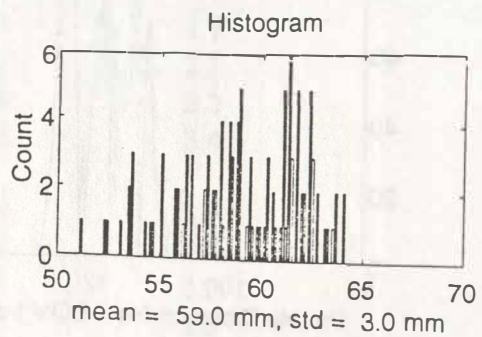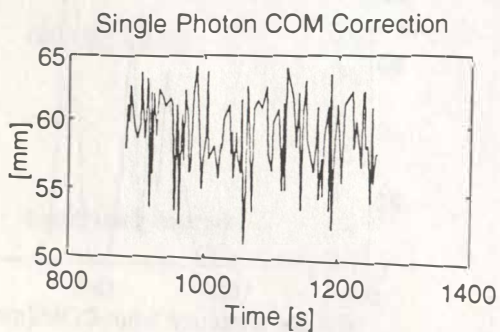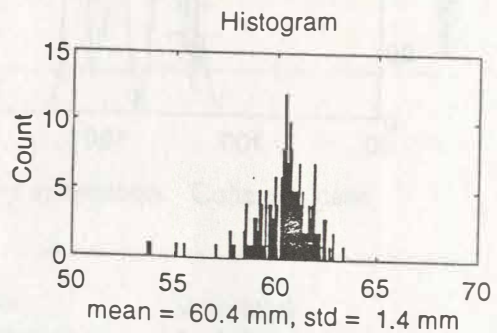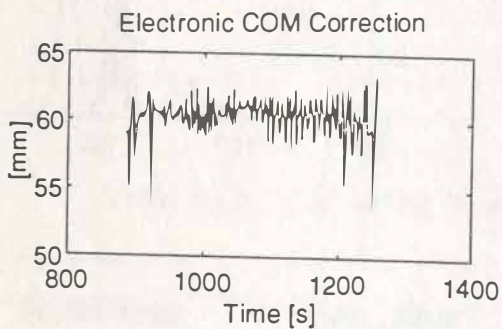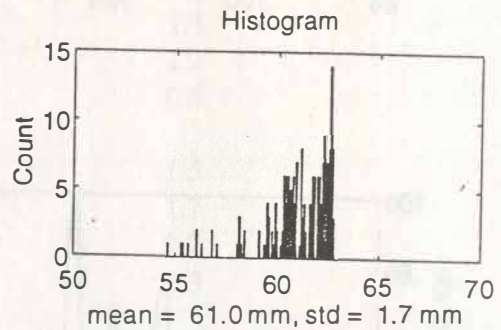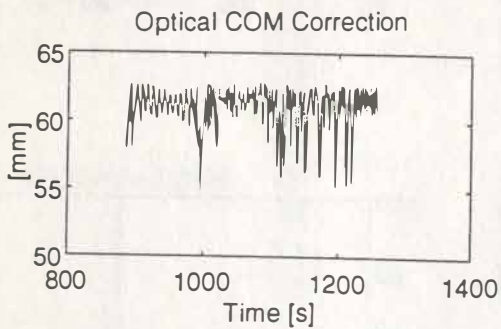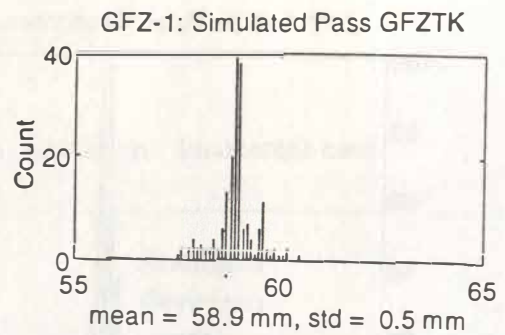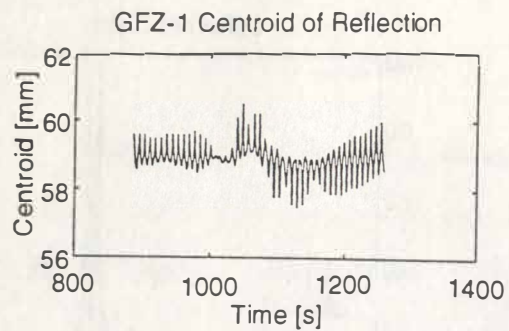
Figure 3.3.4: CoM for the Test Station (coherent case)

22

3.3.2   Results from the Analytical Calculations [Neubert, 1994]

In the frame of the analytical model the average signal shape can be computed by the convolution:

$$F(\xi) = \frac{1}{N\sigma\sqrt{2\pi}} \int_{\alpha_c}^{0} e^{\left[-\frac{(\xi - x(\alpha))^2}{2\sigma^2}\right]} A^2(\alpha) \sin\alpha \; d\alpha \qquad\qquad 3.3.3$$

In this formula σ is the rms width of the gaussian laser pulse (in half range units) and $A(\alpha)$ is the active area of an individual reflector as shown in Fig. 3.3.1. N is a normalizing factor to ensure that the integral of $F(\xi)$ is unity. The function $F(\xi)$ for a laser pulse of 10 ps FWHM ($\sigma = 0.64$ mm) is shown in Fig. 3.3.2. This function can be regarded as the probability density function of the optical signal. It should represent the envelope of a large number of realizations like given in Fig. 3.3.3. The centre of mass correction (centroid) is equal to the first moment of $F(\xi)$:

$$CoM = \int_{0}^{\infty} \xi \; F(\xi) \; d\xi \qquad\qquad 3.3.4$$

The numerical value of this integral in case of GFZ-1 is 59.9 mm as given in Table 3.3.1. The variance is accordingly :

$$S^2 = \int_{0}^{\infty} \xi^2 \; F(\xi) \; d\xi - CoM^2 \qquad\qquad 3.3.5$$

For a 10 ps laser we obtain s = 2.6 mm. This is the expected standard deviation of the range measurements in the pure single photon case if other noise sources can be neglected. It agrees reasonably well with the value of 3.1 mm obtained by simulation.

3.3.3   Conclusion

It has been shown that the results of 3 independent methods to estimate the centre of mass correction agree within 2 mm. This precision is better than needed at present because the errors of the orbital model are more than an order of magnitude higher. Therefore the small deviations of the different aproaches are not of practical importance. The use of the standard value of 58.5 mm to correct the data of all stations neglecting the effects of the different detection systems (single-photon or multi-photon systems) is fully sufficient. Single photon systems should attenuate the return signals to a level below one average photoelectron to avoid power dependent shifts caused by the detector (this could be up to 20 mm).

23

GFZ-1 is the smallest cannon ball satellite at present. According to the calculations it has the most narrow optical transfer function (RMS width of about 3 mm). This is confirmed by the laser observations at the Potsdam station. The RMS width of the histogram of range residuals is about 10 mm. The same value is obtained when ranging to the flat calibration target on ground. This shows that the spreading of the return pulse by the reflector array can not be resolved by this laser system.

3.4   Laser Station Requirements

3.4.1   General Requirements

The low altitude of GFZ-1 (400 km) introduces a much higher apparent angular velocity than for the adopted laser satellites. The orbital velocity v_s of a satellite in a circular orbit can be derived from

$$v_s = \sqrt{G \frac{m_E}{R_E + H_0}} \qquad\qquad 3.4.1$$

where

R_E - mean radius of Earth   (6378 km)
H_0 - orbital height of satellite
G - gravitational constant
m_E - mass of Earth

For GFZ-1 one obtains an orbital velocity of 7658 ms^{-1}. The apparent angular velocity ω can be obtained using

$$\omega = \frac{v_s}{H_0} \frac{180^0}{\pi} \sin \delta \qquad\qquad 3.4.2$$

where

δ - elevation above horizon at culmination

A comparison for the satellites GFZ-1 (H_0= 400 km), ERS-1 (H_0= 770 km) and AJISAI (H_0= 1500 km) is given in Table 3.4.1.

24

Table 3.4.1: Apparent Angular Velocities for Different Satellites

Elevation (deg)	GFZ-1 (deg/s)	ERS-1 (deg/s)	AJISAI (deg/s)
90	1.10	0.55	0.27
70	1.03	0.52	0.25
60	0.95	0.48	0.23
50	0.84	0.42	0.21
40	0.71	0.36	0.17
30	0.55	0.28	0.14
20	0.38	0.19	0.09

As can be seen here, the angular velocity is about twice the value for the "fastest" laser satellites so far (ERS-1 and ERS-2). This implies several problems the laser stations have to face:

a) Near culmination, both velocity and acceleration for the azimuth drive of an alt-azimuthal mount become very large and can exceed the maximum possible values for several mounts already at culmination heights which are uncritical for satellites orbiting at higher altitude. This leads to a zone around culmination where no observations are possible.

b) Stations which are using common transmit-receive paths can get problems with insufficient speed of the rotating transmit-receive switch, because the minimum time of flight for GFZ-1 signals is in the order of only 2.7...3 ms which is half the value for the ERS-satellites.

c) The tracking of GFZ-1 has to be carried out at larger divergency angles for the transmitting telescope than usual to enhance the probability to access the satellite rapidly even under conditions of non visibility (shadow, daylight); satellite acquisition has to be fast, because the useful transit time of GFZ-1 over a laser station is rather short (3...4 minutes in comparison to 6...8 minutes for ERS-1/-2 or STARLETTE).

The items a) and b) are (at least partially) subject to station engineering. To meet the requirements mentioned in item b), at SLR station 7836 Potsdam a newly developed system of rotating transmit-/receive switches was installed which can be operated at 20 Hz rotation frequency for tracking of GFZ-1 instead of the 10 Hz used for satellites with higher orbital altitude.

Requirement c) can be fulfilled only in case that the GFZ-1 satellite is delivering a sufficiently high return signal for SLR stations using a wide angle laser beam. Particularly for daylight tracking multi-photoelectron returns from GFZ-1 are desirable to have a suffcient

25

contrast against the background of the sunlit sky. Special care was taken in the design of the satellite to meet this specification (see sections 3.2 and 3.3).

3.4.2   Signal Strength Estimations for GFZ-1

Let us consider the energy budget for ranging to the GFZ-1 target. Neglecting effects like signal fluctuations due to atmospheric turbulence and coherence effects of the laser light as well as the different location of the receiver in the farfield diffraction pattern of the satellite due to velocity aberration, the well-known radar equation (see e.g. [*Jelalian*, 1992]) can be rewritten in the following form to have access to the parameters used in satellite laser ranging:

$$N_{PE} = \frac{4}{\pi} \frac{E\lambda\eta}{hc} A_{SAT} D^2 \frac{T_{ATM}^{2\cos^{-1}Z} T_{TR} T_{REC} T_{SAT}}{H^4 \theta_{TR}^2 \theta_{SAT}^2} \cos^4 Z \qquad 3.4.3$$

where

N_{PE}	-	number of photoelectrons generated in the receiver
η	-	quantum efficiency of the detector
A_{SAT}	-	effective reflecting area of the satellite
H	-	orbital height of the satellite
T_{ATM}	-	atmospheric transmission at laser wavelength
T_{TR}	-	transmission of the transmitting system
T_{REC}	-	transmission of the receiving system
T_{SAT}	-	transmission of the retroreflectors
D	-	diameter of the receiving telescope
Z	-	zenithal distance of the satellite
θ_{TR}	-	divergency angle of the transmitter after telescope
θ_{SAT}	-	divergency angle of the retroreflectors
E	-	output energy of the laser per pulse
λ	-	laser wavelength
c	-	velocity of light
h	-	Planck's constant

A more detailed approach can be found in [*Shargorodsky*, 1995b] taking into account the farfield distribution of the reflected pattern due to aberration:

$$N_{PE} = \frac{E\lambda\eta}{hc} \frac{A_{SAT} D^2 T_{ATM}^{2\cos^{-1}Z} T_{TR} T_{REC} T_{SAT}}{H^4 \Theta_{TR}^2} P_{SAT} K \cos^4 Z \qquad 3.4.4$$

26

where

$$P_{SAT} = P_{MAx} \; e^{-0.1265(\gamma-\gamma_{AVE})^2}$$

$P_{MAX} = 8.26 \cdot 10^8$

$\gamma - \gamma_{AVE}$ - location of the receiver in the reflection pattern of the satellite with γ_{AVE}=7.7"
(mean value of aberration)

K - factor lowering the efficiency of the reflector due to deviation from an ideal reflector

The above mentioned formula is valid for γ ranging from 4.9"... 10.5" (lower and upper limit of the velocity aberration for GFZ-1) .

Let us consider 3 SLR station types to estimate the expected signal level for passes of GFZ-1 at different culmination heights:

Station 1: E = 100 mJ, D= 0.6 m (MOBLAS type)
Station 2: E = 50 mJ, D= 0.3 m (TLRS type)
Station 3: E = 10 mJ, D= 1.0 m (Potsdam)

The other parameters were selected to : A_{SAT}=5.14$\cdot$10^{-4}m^2 (GFZ-1), H=400km, T_{ATM}=0.7, T_{TR}=0.25, T_{REC}=0.12, T_{SAT}=0.54, θ_{TR}=1 mrad, θ_{SAT}= 15 µrad, λ= 0.532 µm, K=0.7. In case of the more detailed Eq. 3.4.4, the value for P_{SAT} can vary between 0.37P_{MAX} and P_{MAX} for 4.9"<γ<10.5", being maximum for γ=γ_{AVE} (7.7"). The value for γ at culmination (azimuth le of satellite velocity vector = 90^0) is determined by:

$$\gamma = \frac{2 \, v_s}{c} \sqrt{\left(1 - \left(\frac{R_E}{R_E + H_o}\right)^2 \sin^2 Z\right)} \qquad \text{3.4.5}$$

The computation of expected signal strength (number of photoelectrons) for GFZ-1 according to Eq. 3.4.4 gives the results as shown in Table 3.4.2:

Table 3.4.2: Theoretical Number of Photoelectrons from GFZ-1

Elevation	Station		
	1	2	3
(deg)	(N_{PE})	(N_{PE})	(N_{PE})
90	321	40	89
80	333	42	93
70	360	45	100
60	362	45	100
50	288	36	80
40	133	19	41
30	40	5	11
20	5	1	1

It should be pointed out again that for the signal strength computations several simplifications (like neglection of signal fluctuation effects and assumption of a homogenous laser energy distribution over the entire beam diameter) were made. In reality, this leads to somewhat weaker signals than computed, but in any case it turns out that the signal strength of GFZ-1 is fully sufficient for all station types mentioned to perform tracking even at divergency angles larger than 1 mrad. This enables reliable daylight tracking at multi-photoelectron level using wide beams particularly in case of a not perfectly known timebias for GFZ-1.

3.4.3 Signal Strength Determinations

Several stations tracking GFZ-1 reported that according to their experience the signal is about one order of magnitude stronger than for STARLETTE under the same ranging conditions. This can be expected due to the parameters of STARLETTE (higher orbitalaltitudebymorethan a factor of 2, but higher effective cross-section and reflectivity than GFZ-1).

Real measurements of the signal strength of GFZ-1 are reported in [Shargorodsky , 1995b] for 3 passes tracked by the station 1864 Maidanak. The results show a reasonable agreement between theory and experiment, but it should be pointed out that the measurements for all 3 reported passes were done at very low elevation angles of the satellite where atmospheric effects strongly influence the returns. No details about experimental setup and statistical significance of the results are given. Thus, it would be interesting to carry out similar experiments at other SLR stations as well.

4. MISSION CONTROL

4.1 *Preparatories*

4.1.1 *Milestones and Trade-offs*

Only a few meetings took place between the project teams of GFZ and of the main contractor, the KT company, partly accompanied by the sub-contractor for the satellite design, RNIIKP, and the sub-contractor for the satellite launch, RKK Energia. Table 4.1.1 gives an overview of the meetings.

Table 4.1.1 Project Meetings

Purpose	Date	Place	Participants
Kick-Off	Feb 14, 1994	Munich	GFZ, KT, RNIIKP
Signing of Contract	May 31, 1994	Berlin	GFZ, KT
Working Meeting	Dec 12, 1994	Munich	GFZ, KT, RNIIKP
Acceptance	Feb 23, 1995	Moscow	GFZ, KT, RNIIKP
Working Meeting	Feb 24, 1995	Moscow	GFZ, KT, RKK Energia

The main path of exchanging informations, questions and analyses was set up between GFZ and KT via phone and fax. All input from the Russian side was formulated in Russian and first went to KT for translation. Despite of this drag, in general all informations arrived at GFZ in time. The closeby location of the mission control center of GFZ in Oberpfaffenhofen (D-PAF) near Munich and the KT company in Munich offered a nearly personal link for the project teams. KT also operates a bureau in Moscow, which provided a fast and reliable contact to the Russian sub-contractors. These environments caused a quite effective information flow.

Nevertheless the minimum number of meetings set the milestones in the course of the pre-launch mission. Already in February 1994, before the R&D contract was signed, a team of GFZ, KT and RNIIKP discussed first design issues. A first preference was given to near sperically shaped, massive bodies made from steel or bronze with diameters of 190 mm and 260 mm and 60 retroreflectors on the surface. An optimal launch opportunity was considered to be an ejection from space station MIR at altitudes between 350 km and 425 km. Investigations were initiated to analyse the drag effect of the different area-to-mass ratios and possible lifetimes. Also the possibilities of the global SLR network for tracking such a difficult object should be elaborated in more detail. At that time it was known that NASA had the intention to start a few month long SLR campaign on the 425 km altitude, military satellite MSTI-2 to be launched in June 1994. For the GFZ-1 mission this turned out to become a first check-out of the SLR network perfomance and of the POD procedures at GFZ.

At the Air and Space Exhibition in May, 1994, in Berlin, GFZ signed the contract with KT for the design, contruction and launch of GFZ-1. The project was to be realized from design

29

to injection into orbit within a time frame of not more than one year and an available budget of less than 700.000 US $ including launch cost. In the following KT made agreements with RNIIKP for the design, construction and test of the satellite and with NPO Energia for the transport of the satellite to space station MIR and the deployment into orbit.

In July, 1994, RNIIKP delivered the draft version of the design documents, where the anticipated final characteristics of GFZ-1 were layed down. A detailed discussion of the technical concept can be found in chapter 3 above.

In the December 1994 meeting, KT reported on status and schedule of the project. All 60 two-spot reflectors had been selected, however the installation into the satellite body was slightly delayed by a few days with no impact on the schedule. The design of the separation mechanism, of the adapter for the MIR airlock and of the transport-container was fixed after the GFZ-1 project team decided to deploy GFZ-1 in space with no dedicated rotation.

The LAGEOS and other geodetic satellites rotate at defined rates in order to avoid orbit perturbations effected by large thermal gradients in the satellite body. As bronze, the material of the body of GFZ-1, and the enamel coating of the surface are expected to provide moderate temperature gradients, the initial concept of dedicated in-orbit rotation of GFZ-1 was dropped. An additional reason came from the fact, that the Poynting-Robertson effect shows up in along-track direction with or w/o rotation and can be taken care of by the drag parameters in the POD process.

Other foreseeable physical nuisance effects as those of Yorkovsky and Schach will act mainly in direction of the Sun. W/o rotation a nearly constant effect can be assumed sizing at appr. 5% of the radiation parameter anyway estimated in the POD process. A deeper insight into Poynting-Robertson, Yarkovsky and Schach effects can be gained in *Reigber et.al.* [1982]. All in all it was concluded that the modelling accuracy of the orbit can be enhanced if the satellite would not rotate. However it was quite clear that a small rotation can not be avoided due to a limited accuracy of the construction of the separation mechanism.

Also in the December meeting, GFZ reported on new SLR acquisition procedures becoming necessary due to the low altitude of GFZ-1. Experience showed that tuning of IRVs alone could not anymore account for the missing drag models in the SLR station orbit integrators. The idea was born to extend the time bias function, which had become a standard after its introduction by GFZ appr. 3 years before for ERS orbit predictions. A detailed discussion of this matter, namely the so-called drag function follows in chapter 4.1.4.

For the training of the SLR network, an optical campaign on space station MIR was foreseen. The performance and outcome of the campaign are described in chapter 4.1.3.

On request by RKK Energia, the first iteration of the requirements for the scenario of the orbit deployment of GFZ-1 were specified. The final scenario follows in chapter 4.2 in more detail.

A major point of concern expressed in the December meeting, was layed on backup solutions in case the SLR network looses acquisition of GFZ-1 due to bad weather, daylight tracking periods, poor orbit prediction accuracies etc.. Independently GFZ and KT had contacted

different persons and institutions to find out possible support from radar tracking facilities. Interest into the GFZ-1 mission came from the German FGAN radar facility near Bonn, but under the unfortunate circumstances of a shutdown for upgrading during the first half year of the mission. The Russian Anti-Satellite-Radar network offered radar tracking backup, but at unacceptable high budget charges. Of no charge, twoline orbital elements generated by USSpaceCom will be posted in the public catalogue of AFIT by request from GFZ. Chapter 4.1.5 is dedicated to the conversion of twoline elements.

As the construction of the satellite was well in schedule, the next meeting was foreseen for beginning of 1995 in Moscow. Indeed on February 23rd, 1995, the satellite was formally handed over to GFZ, accepted by GFZ, and then passed to RKK Energia for transport and space deployment. The next day a quite informative discussion with RKK Energia took place on the separation scenario. The final scenario was fixed later on via fax communications.

With GFZ-1 in space on April 19th, 1995, only 11 months elapsed since the signing of the contract. A low budget, fast realization project resulted in a fine, little device having meanwhile proofed its careful design and its usefulness for achieving the scientific objectives.

4.1.2 Information of the SLR Network

The exclusive tracking system of GFZ-1 is SLR. As the SLR community operates on a no-exchange-of-funds basis, new campaigns can only succeed if

- a sufficient number of SLR stations is able and is willing to track the new target;

- the data centers CDDIS and EDC agree to archive acquisition and tracking data;

- a dedicated analysis center provides the acquisition data, i.e. orbit predictions.

The ability to track GFZ-1 is dependent on the H/W configuration of the individual stations (see f.i. chapter 3.2). During the MSTI-2 campaign in summer, 1994, the MOBLAS stations had proofed their low altitude target tracking capabilities. The MTLRS systems and many of the fixed systems were rated beforehand as possible tracking partners. In order to get support from the network, tracking requests went out to the NASA SLR network, to the EUROLAS stations, and to the stations in Japan, Australia, China, and Russia. The reactions were positive in general. CDDIS and EDC were contacted, both confirmed their support. The responsibility of generating and distributing orbit predictions was taken by GFZ/D-PAF. Also the merging of data from the data centers remained with GFZ/D-PAF following the procedures running successfully for the ERS-1, ERS-2 and METEOR-3 satellites.

A good chance to promote the mission further more in the community was given at the 9th International Workshop on Laser Ranging Instrumentation in Canberra, Australia, November 1994. The main objective of the mission (i.e. gravity field improvement) and the dramatic impact of the atmosphere on orbit perturbations were presented in a paper by *Reigber and König* [1994]. A second paper by *König and Chen* [1994] explained the difficulties in predicting the orbit for GFZ-1. It was particularly outlined that time bias values of seconds

31

can occur within a few days due to unforeseeable solar activities.

In the CSTG subcommission meeting held during the Workshop, the GFZ-1 mission along with the upcoming ERS-2 and the ERS-1/ERS-2 TANDEM mission got special attention (see *Reigber et. al., 1994*). The EUROLAS meeting in Munich in March 1995 including participants from NASA, ATSC and from the US Naval Research Laboratory provided a furhter platform to inform the stations about the status of the mission [*Reigber and König*, 1995a]. The almost final version of the newly designed drag function (see chapter 4.1.4) was introduced by *Chen and König* [1995]. All stations expressed their willingness in tracking GFZ-1 as far as H/W permits.

A detailed support plan was prepared by NASA beginning of 1995 [*Jessie*, 1995]. A meeting in March 1995 with NASA and ATSC representatives at GFZ/D-PAF showed a breakdown of upcoming NASA SLR activities and the problems they had to face in view of an immense budget cut. The high priority given to GFZ-1 in NASA SLR operations [*Bosworth et.al.*, 1995] however was fully satisfying.

Concluding the above, before launch the course was set for a successful SLR campaign. This led to a remarkable good tracking record already from the very beginning when GFZ-1 was in orbit.

4.1.3 MIR Optical Campaign

The MIR optical tracking campaign was initiated in view of the GFZ-1 mission as a SLR net training campaign. The goals were:

- to make the SLR stations get used to this low altitude target;
- to test the processing chain from radar tracking derived orbital elements via tuned IRVs to updated orbit predictions on the basis of optical measurements by the SLR stations;
- to have the best orbit predictions available for GFZ-1 at the time of its ejection from MIR end of April.

GFZ/D-PAF generated tuned IRVs for MIR from radar tracking based NORAD twoline elements. IRVs and time bias functions were stored in the CDDIS and EDC data bases under the usual conventions and were also send directly to the stations according to the ERS-1 and METEOR-3 distribution procedure.

The stations were asked to optically track MIR on the basis of the IRVs and report to GFZ/D-PAF on time bias and other prediction quality estimates as available. The stations were encouraged to measure azimuth and elevation angles and forward those to the data centers in the form of Q/L format engineering data records. The nighttime visibility periods for MIR were distributed dependent on the locations of the stations. A raw overview can be gained from Table 4.1.3.1.

32

Table 4.1.3.1: Visibility Intervals for Some Selected Stations

Station	Longitude (deg)	Latitude (deg)	Visibility Periods (day.month.)		
Graz	15.5 E	47.1 N	01.3.-07.3.	24.3.-12.4.	17.4.-30.4.
Yarragadee	115.3 E	29.0 S	13.3.-19.3.	05.4.-10.4.	20.4.-24.4.
Shanghai	121.2 E	31.1 N	07.3.-09.3.	22.3.-29.3.	12.4.-17.4.
Monument Peak	116.4 W	32.9 N	04.3.-09.3.	23.3.-01.4.	11.4.-16.4.
Greenbelt	76.8 W	39.0 N	01.3.-07.3.	23.3.-01.4.	08.4.-19.4.
Santiago de Cuba	75.8 W	20.0 N	08.3.-10.3.	19.3.-23.3.	13.4.-17.4.

The official tracking request went out to the global network beginning of March, 1995. However GFZ/D-PAF started a pre-campaign with Graz, Herstmonceux and Potsdam for the period January 26 to February 6 and got the first observed pass by Graz on February 1. Santiago de Cuba joined the campaign with a good observational window starting February 11. Shortly later the NASA stations located further to the west joined the campaign also. So 12 passes have been observed already in February. The tracking statistics of the overall campaign is depicted in Figure 4.1.3.1.

Number of Passes per Day
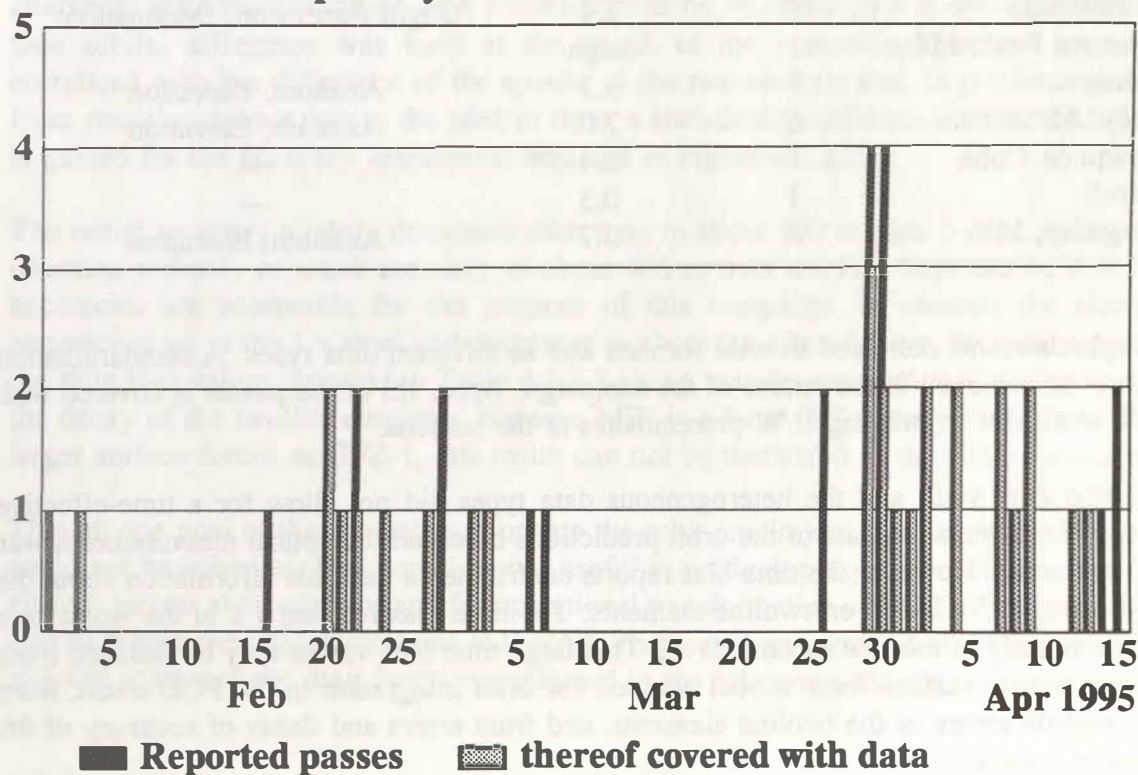
Figure 4.1.3.1: MIR Optical Acquisitions

33

Figure 4.1.3.1 reveals the inherent disadvantage of optical campaigns. Due to the unequal geographical distribution of the stations, visible passes can only be observed during certain periods. The tracking record shows better or poor outcome distributed periodically in time. A similar performance could be expected for the GFZ-1 campaign if the orbit predictions would not provide the accuracy required and therefore the acquisition would have to be based on optical search procedures (refer to chapters 4.2.3 and 5.1 for GFZ-1 visibilities and to chapter 5.1 for GFZ-1 tracking statistics).

In the MIR optical campaign 9 stations reported on 42 passes over a period of 74 days. The number of passes per station are compiled in Table 4.1.3.2. The table includes also the maximum time bias values reported and the data types delivered.

Table 4.1.3.2: Station Reports and Data

Station	No. of Passes	Max. Time Bias (s)	Angle Data Type
Graz	3	1.5	---
Greenbelt, M7	6	5.6	Azimuth, Elevation
Herstmonceux	14	2.4	Right Ascension, Declination
Monument Peak, M4	1	large	---
Potsdam	7	3.3	Azimuth, Elevation
Quincy, M8	6	7.0	Azimuth, Elevation
Santiago de Cuba	1	2.4	---
Wettzell	1	0.3	---
Yarragadee, M5	3	2.7	Azimuth, Elevation

The angle data was delivered in wild formats and as different data types. A standardization could not be achieved in the course of the campaign. Appr. 1/3 of the passes is covered with no data at all due to missing H/W prerequisites at the stations.

The sparse data yield and the heterogeneous data types did not allow for a time-effective analysis. Therefore an update of the orbit predictions based on the optical measurements was never conducted. However the time bias reports contributed a valuable information about the quality of the IRVs based on twoline elements. The time bias reached 7 s in the worst case and sized mainly in the few seconds level. This large time bias values may be deduced from the rather simple surface force model adopted for orbit integration in the POD chain, from transformation errors of the twoline elements, and from errors and decay of accuracy of the twolines elements.

In order to assess the quality of the MIR twoline elements, differences of orbits generated from successive twoline element sets were analyzed. The orbits were computed with the
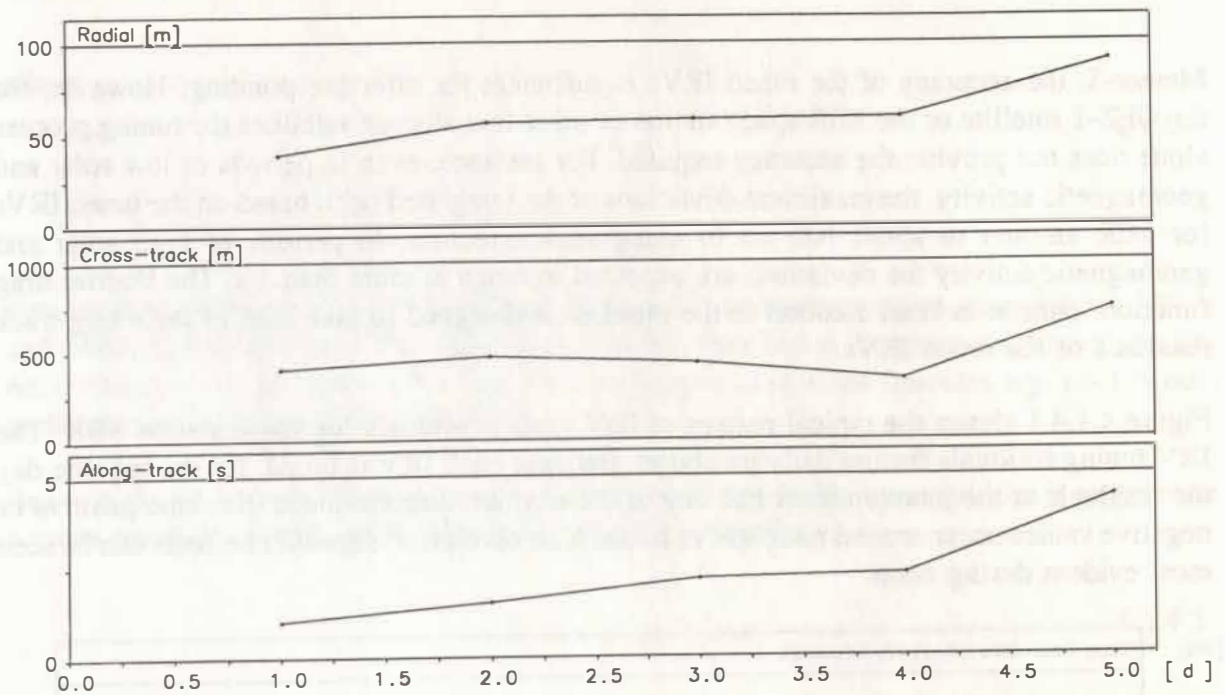
Figure 4.1.3.2: Twoline Elements Accuracy for MIR

analytical orbit reconstruction S/W recommended by NORAD [*Hoots and Reohrich, 1980*]. One orbital difference was built at the epoch of the succeeding element set and then correlated with the difference of the epochs of the two element sets. In proceeding stepwise from one element set pair to the next in time, a statistically sufficient number of differences is gained for the accuracy assessment depicted in Figure 4.1.3.2.

The radial accuracy slightly decreases with time to about 100 m after 5 days. In cross-track direction a timely constant accuracy of about 400 m over the first days can be noted. Both accuracies are acceptable for the purpose of this campaign. In contrast the along-track accuracy sizes at the 1 s level and decreases to about 5 s after 5 days. So quite a portion of the time bias values reported in Table 4.1.3.2 above may be assigned to the accuracy and to the decay of the twoline elements. Because MIR is a huge S/C experiencing appr. 20 times larger surface forces as GFZ-1, this result can not be transfered to the GFZ-1 mission.

Though one goal of the campaign to update the orbit predictions from optical measurements could not be achieved, the campaign was useful in producing experience for tracking of low altitude targets at the stations and for operational transformation of NORAD twoline elements into SLR suitable orbit predictions at D-PAF. The campaign provided also the opportunity to test and introduce the drag function explained in the following chapter.

4.1.4   Design of the Drag Function

Tuning of IRVs is a means to account for the missing drag model in the orbit integration program at satellite tracking stations. For satellites at certain altitudes, e.g. ERS-1 and

35

Meteor-3, the accuracy of the tuned IRVs is sufficient for effective pointing. However, for the GFZ-1 satellite or the MIR space station or other low altitude satellites the tuning process alone does not provide the accuracy required. For instance, even in periods of low solar and geomagnetic activity, the maximum deviations of the integrated orbit based on the tuned IRVs for MIR amount to about 100 ms in along-track direction. In periods of high solar and geomagnetic activity the deviations are expected to range at more than 1 s. The Fourier drag function chosen as final solution to the problem is designed to take care of the along-track residuals of the tuned IRVs.

Figure 4.1.4.1 shows the typical pattern of IRV tuning residuals for space station MIR. The IRV tuning residuals feature daily parabolas. Because each IRV is tuned for the specific day the residuals at the junction from one day to the next are discontinuous. Extreme positive or negative values occur around midnight or noon. Also revolution dependent effects can be seen most evident during noon.
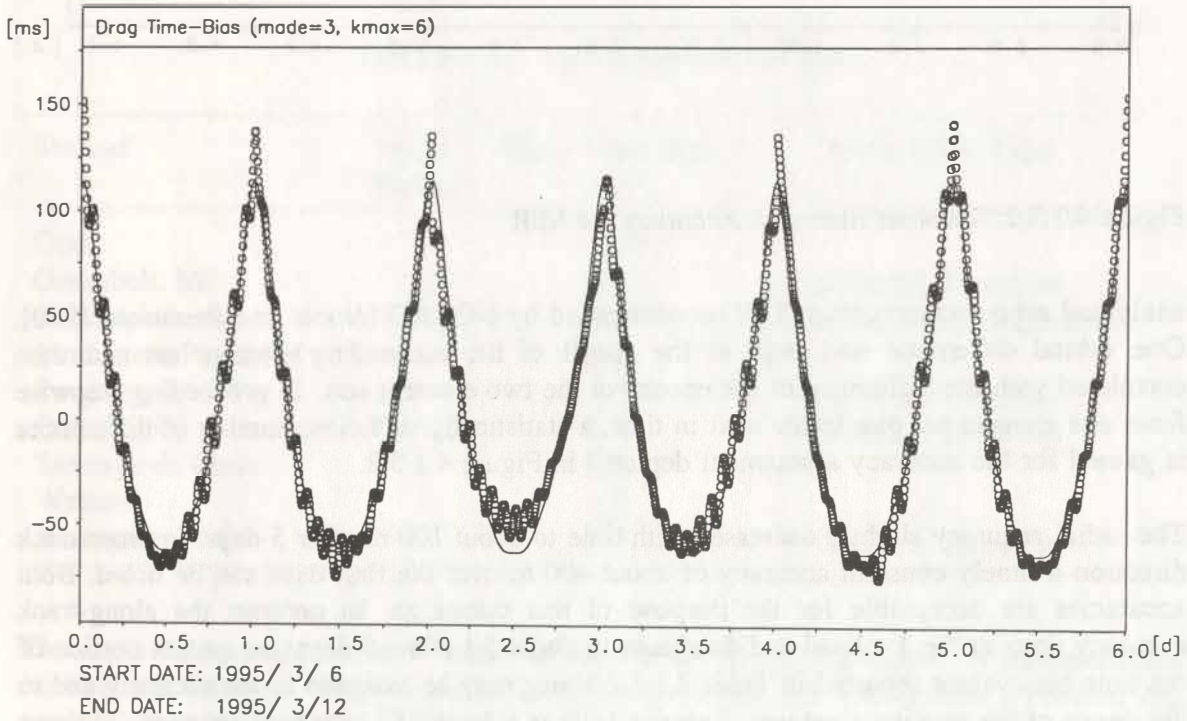
Figure 4.1.4.1: Example of IRV Tuning Residuals for MIR

The first approach for a function approximating the drag residuals is a daily parabolic function:

$$y = a + bt + ct \qquad\qquad 4.1.4.1$$

where

$$0 < t \leq 1 \qquad \qquad 4.1.4.2$$

similar to the time bias function adopted by the SLR community since years for the ERS-1 and METEOR-3 satellites. The disadvantage of this function is it's short validity of one day only. t must never get larger than 1, an incorrect application of the function, e.g. t > 1, would yield hazardous wrong drag corrections.

Because the IRV residuals obey similar patterns from day to day a second idea is to generate a mean parabolic function for the whole prediction period, i.e.

$$y = a + b\, dt + c\, dt \qquad \qquad 4.1.4.3$$

where

$$0 < dt \leq 1 \qquad \qquad 4.1.4.4$$

The disadvantage of this function is the discontinuity of dt at t = 1, 2, ..., N (see Figure 4.1.4.2). dt is allowed to vary between 0 and 1. Just like in case of the above daily parabolic functions, an incorrect application, e.g. dt > 1, would yield wrong drag corrections.
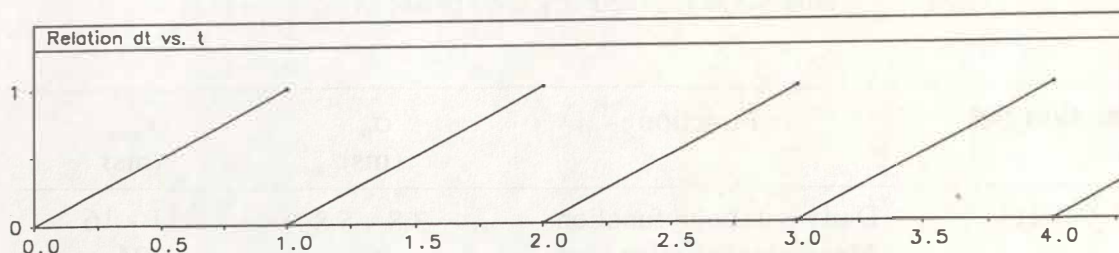
Figure 4.1.4.2: The Relation of dt and t

The third and final approach is the Fourier function

$$y = a + b \sum_{k=1}^{kmax} (-1)^k \, coskx \,/\, k^2 + c \sum_{k=1}^{kmax} (-1)^k \, sinkx \,/\, k \qquad 4.1.4.5$$

37

where

$$x = 2\pi \, (t - 0.5)$$

4.1.4.6

and

$$0 < t \le N$$

4.1.4.7

for the whole prediction period. For kmax equal to infinity, the Fourier function and the mean parabolic function are equivalent. The advantage of this function is that t is valid for the whole prediction period and therefore the discontinuity problem vanishes. In comparison to the mean parabolic function, the evaluation of the Fourier function at kmax less than 30 needs hardly more computation time.

Examples of the fitting accuracy of the presented drag functions for two MIR orbit predictions can be seen in Table 4.1.4.1. Taking into account anyone of these drag functions, the IRV tuning accuracy can be improved to better than 10 ms. The daily parabolic function yields the best fitting accuracy due to the large number of function terms. The accuracies of the mean parabolic function and of the Fourier function are of comparable size. An example of the residual distribution of the Fourier drag function with an expansion degree of 6 is displayed in Figure 4.1.4.3. Maximum residuals occur mostly around midnight. The residuals can mainly be deduced from the differences of the daily varying atmospheric models.

Table 4.1.4.1: Accuracy Comparisons

Prediction Set	Function	σ_0 (ms)	v_{max} (ms)
pred_950214	Daily parabolic function	3.8 - 5.8	11 - 16
	Mean parabolic function	7.6	24
	Fourier function	7.6	23
pred_950223	Daily parabolic function	4.1 - 6.2	12-18
	Mean parabolic function	8.0	37
	Fourier function	8.0	34

After the consideration of the advantages, of the disadvantages, of the fitting accuracies and of the convenience of application, the Fourier function was finally chosen as the new tool to accomodate drag in SLR low altitude target acquisition.

Further investigations with the Fourier drag function reveal that in case of low solar and geomagnetic activity a maximum expansion degree of 6 is sufficient. In case of high solar and

38

geomagnetic activity, the application of more than 1 drag function for the prediction period could become necessary and a higher degree of expansion will be required.

START DATE: 1995/ 3/ 6
END DATE: 1995/ 3/12
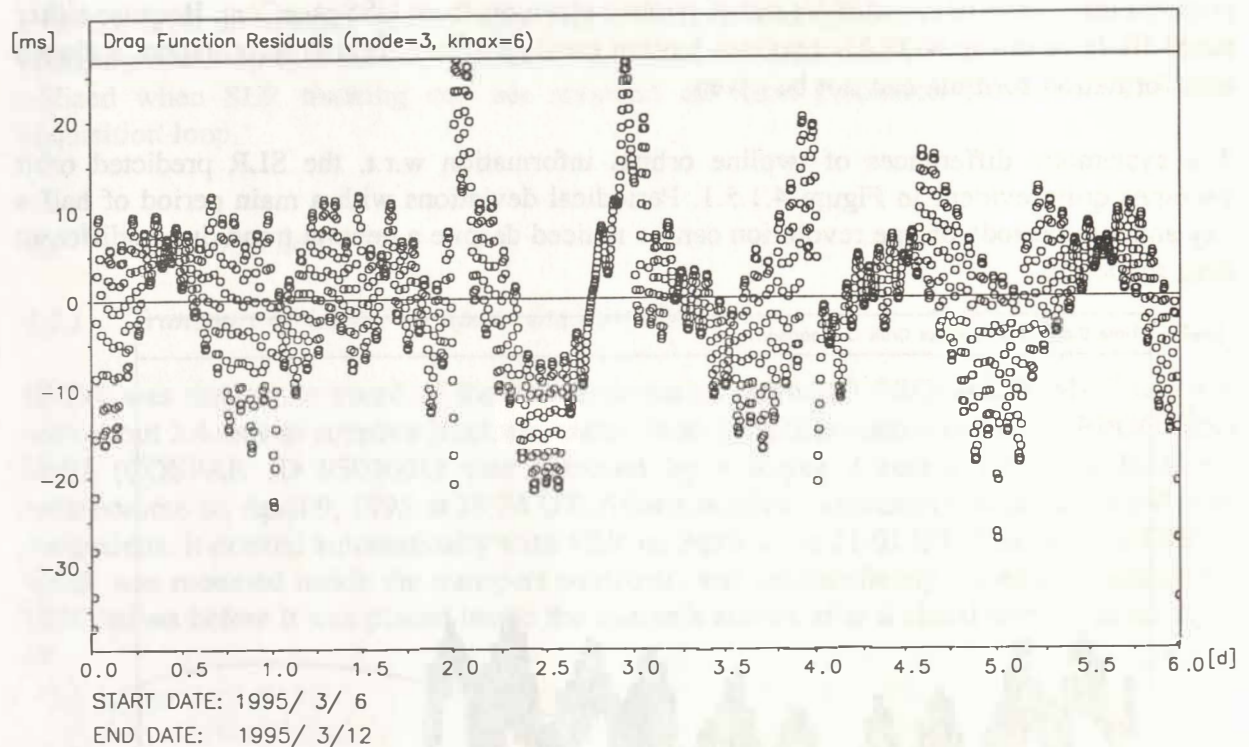
Figure 4.1.4.3: IRV Tuning Residuals after Application of the Fourier Function

The application of the new drag function for SLR acquisition is very simple: there is no change in the adopted usage of the time bias function in conjunction with the tuned IRVs. The drag function comes in addition, that means:

actual orbit = IRV orbit integration + drag function + time bias function

So the time bias computed from the drag function can simply be added to the time bias computed from the time bias function.

4.1.5 Transformation of Twoline Elements

The so-called twoline elements or NORAD elements generated by USSpaceCom (formerly NORAD) can be used to predict position and velocity of satellites. In order to do so a prediction method has to be used which is compatible with the way of generating the elements. The twoline elements consist of mean orbital elements where certain periodic variations have been removed. The analytical theory is mainly based on the solution of *Brouwer* [1959]. A detailed formulation and FORTRAN routines are compiled in *Hoots and Roehrich* [1980].

GFZ/D-PAF has gained experience in generating twoline elements on demand by the German mobile SAR station in the course of the ERS-1 mission. As a by-product in form of Brouwer mean elements generated in the SLR orbit prediction chain, the quality of appropriate, ERS-1

39

dedicated twolines could be validated by comparison with the original NORAD elements. For the GFZ-1 mission the procedure has to go the other way around: to generate SLR orbit predictions in form of tuned IRVs out of twoline elements from USSpaceCom. Because either tuned IRVs or either NORAD twolines feature totally different orbital information, a closed transformation formula can not be given.

The systematic differences of twoline orbital information w.r.t. the SLR predicted orbit becomes quite evident in Figure 4.1.5.1. Periodical deviations with a main period of half a day and sub-periods of one revolution can be noticed despite a general trend due to different drag modeling.
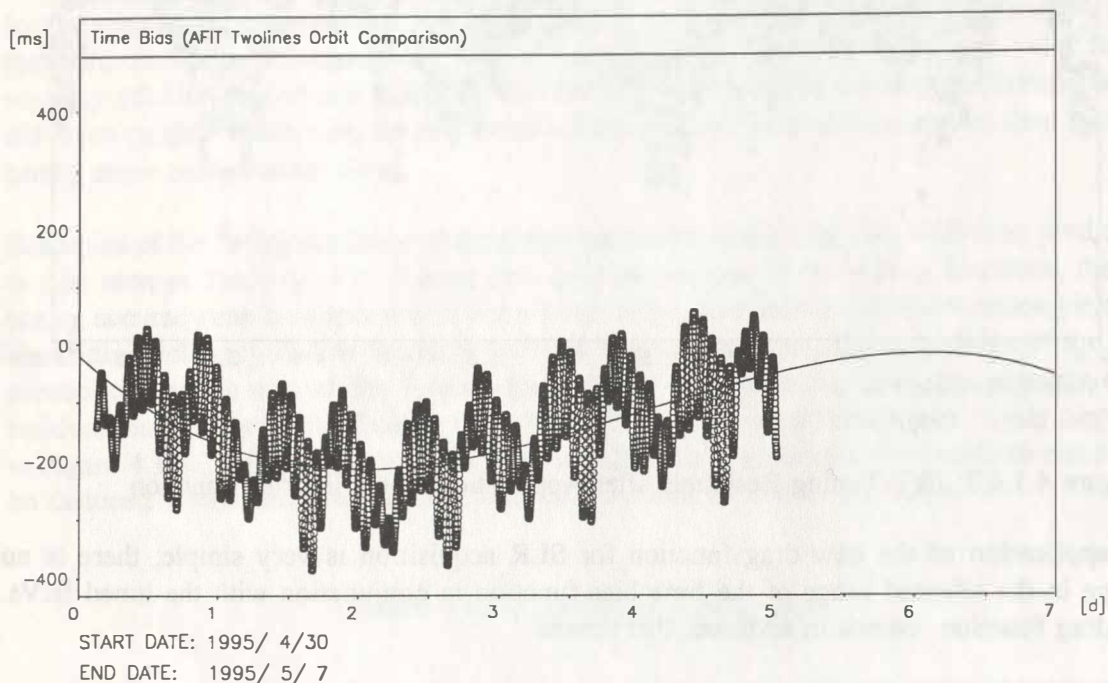
Figure 4.1.5.1: Along-track Differences of Twoline and SLR Orbit Predictions

In order to minimize systematic effects induced by different orbit modeling, the transformation of twoline elements into IRVs proceeds in the following way:

1. generation of position and velocity vectors for at least one day from twoline elements based on the twoline analytical model;

2. generation of position and velocity vectors for the same period based on the SLR orbit model in a first approximation;

3. minimization of the differences of the two orbits in the least squares sense by differential improvement of the initial state vector of the SLR orbit;

4. optimization of the global drag coefficient of the fitted SLR orbit for long-term atmospheric drag compensation;

5. generation of tuned IRVs in the usual way from the drag adjusted, fitted SLR orbit.

40

One public catalogue countaining GFZ-1 twoline elements is provided by AFIT. The elements can be accessed via "ftp" in batch mode processing. This is regularly performed at GFZ/D-PAF for orbit predictions quality assurance. A second catalogue is held at GSFC, which is probably more up-to-date, but has to be accessed in interactive mode. This way is only utilized when SLR tracking can not maintain the orbit prediction generation and data acquisition loop.

4.2   Orbit Injection

4.2.1   Transport of GFZ-1 to Space Station MIR

GFZ-1 was carried on board of the automatic cargo spacecraft PROGRESS M-27 together with about 2.4 tons of supplies (fuel, air, water, food, scientific instrumentation). PROGRESS M-27 (COSPAR ID 9502001) was launched by a Soyuz-V rocket from the Baikonur cosmodrome on April 9, 1995 at 19:34 UT. After a nominal approach including several orbit corrections, it docked automatically with MIR on April 11 at 21:01 UT. The satellite GFZ-1, which was mounted inside the transport container, was intermediately stored on board of the MIR station before it was placed inside the station's airlock after a visual inspection on April 19.

4.2.2   Separation Mechanism

To enable the controlled orbit injection of GFZ-1 from the MIR airlock, a special separation mechanism with the following features was constructed:

- mechanically simple and robust construction suited for reliable operation in space
- avoidance of electronical and pyrotechnical components
- "soft" release of GFZ-1 from MIR with low relative velocity and a controlled velocity vector
- low weight

The release mechanism consisted of a sliding carriage and guide rail for attitude control during release from the airlock, two spring-loaded head mechanisms connected by a fixation strap around the satellite body of GFZ-1 and a mechanical timer/cutter mounted on the lower head mechanism.

The function principle was simple: immediately after the spring-induced release of the unit GFZ-1+separation mechanism, the preset timer became automatically activated . This timer cut the fixation strap after the time interval chosen (60 seconds) and the head mechanisms were ejected away from GFZ-1 by the force of their suddenly unloaded springs, leaving GFZ-1 flying free from that very moment.

Special care was taken to avoid possible collisions of fragments from the release mechanism with the MIR station: the force of the load springs for the head mechanisms was selected such that the maximum velocity of the fragments relative to GFZ-1 could not exceed $0.8 \ ms^{-1}$. Thus, by giving GFZ-1 itself a separation velocity of $1.7...1.8 \ ms^{-1}$ relative to MIR, even in

41

the worst case of an accidental release of one of the mechanism fragments directly into the direction of the space station they were unable to collide with it.

The proper function of this mechanism was proven in several ground tests including training sessions for the new crew of the MIR station using a technological model of the MIR base module which contains the airlock.

4.2.3 Separation Scenario

4.2.3.1 Choosing the Proper Date and Time

During the planning of the GFZ-1 mission, special care was taken of the critical separation phase of the satellite from the MIR station. By choosing the proper conditions for this, the early acquisition of the entirely passive satellite by the international network of SLR stations could be drastically promoted. To choose the date of release, a compromise had to be found between the optimum visibility conditions for the SLR station network and the technological requirements on board the MIR station.

From the point of view of laser tracking, an as long as possible nighttime visibility period for as many as possible SLR stations was desirable at least for the first weeks of tracking. Due to the extremely low orbit of GFZ-1, a longer period with night passes illuminated by sun and practically without shadow could be expected for the stations in the northern hemisphere with latitudes >30° only during northern summer. In all other seasons the following sequence of visibility is taking place:

    a) evening visibility: satellite is illuminated during ascending parts of the pass, entering into shadow later;

    b) midnight shadow: there are no visible passes at all, the satellite is fully in shadow during all passes;

    c) morning visibility: the satellite enters into illumination during the pass, being in shadow at the beginning;

    d) daylight period: there are no visible passes at all, the satellite is in daylight during all passes;

    e) evening visibility: see above;

    f) a.s.o..

In spring and fall, the duration of such a cycle is roughly one month. For the period of first acquisition and orbit determination, besides the rare summer periods without shadow, the evening visibility is more desirable, because a satellite once guided visually in the beginning of the pass can be tracked into Earth' shadow without problems by a trained SLR observer thus maximising the time available for ranging. A morning visibility is less suited for this purpose, and especially during the first days of the mission a sufficiently high accuracy of

42

orbital modelling for fully blind or even daylight tracking could not yet be expected. In the spring of 1995, there was an evening visibility for the European laser tracking stations from mid to end of April and a full-night visibility period during June.

On the other hand, several technological restrictions from the point of view of the MIR mission had to be taken into account. The Russian side presented the following timetable of scheduled activities concerning the MIR station the release of GFZ-1 had to be synchronized with:

- 9.4.95: launch of PROGRESS M-27 with GFZ-1 on board;
- 11.4.95: docking of PROGRESS, start of unloading the transporter;
- 19.4.95: earliest possible date of separation;
- 28.4.95: start of several EVA's of the MIR crew; end of evening visibility over Europe;
- 18.5.95: docking of the SPEKTR module with MIR, start of a sequence of module rearrangements to prepare the docking manoeuvre of the Space Shuttle mission STS-71 in summer 1995;
- 12.6.95: docking of Space Shuttle.

The Shuttle mission was finally delayed for several weeks, but in any case a release of GFZ-1 had to be considered only for the time between April 19 and 28, 1995 or for a time after July which seemed unreasonable.

4.2.3.2 Separation Strategy

Whereas an evening visibility was desirable for easy acquisition of GFZ-1 by a laser station, it was the opposite case for the release from MIR. This is due to the selected strategy of the separation which is routinely used to deploy trash containers from the station's airlock to decay later in the upper atmosphere during reentry. For this procedure the attitude of the MIR station is changed in such a way that the vector of the relative velocity of the separated object is anti-parallel to the velocity vector of MIR. In this way, the satellite and the separated components of the launch mechanism will loose orbital height due to the small difference in orbital velocity during separation (loss of energy!) and will be directed into a transient orbit several kilometers below MIR; in this lower orbit, the orbital velocity increases again, and the satellite will "overtake" the MIR station after a short time. This procedure avoids the risk of a later collision of fragments of the separated bodies with MIR. The further separation of MIR and the released objects will take place according to their different ballistic coefficients.

In principle, the deployment of the satellite could be carried out at any given moment, but for some reasons it is favourable to do this under the visual control of the MIR crew being in direct radio contact with the Mission Control Center (MCC):

- any unexpected situation can be discussed with specialists on the ground;
- the success of the release can be controlled directly, it can be recorded on video tape for later evaluation;
- additional information about the relative velocity of the separated object can be gained

43

by the station crew using an on-board laser distance meter; this enables the generation of more precise orbit data.

To control the procedure of separation, it is desirable for the station crew to have the sun in their back and to have a maximum contrast of the satellite against the background. These requirements are fulfilled best immediately after the exit of the MIR station from the Earth' shadow ("morning terminator"), the illumination conditions are still acceptable until the "midday point" (sun about 90° "over" the station) and get critical near the evening terminator, when the crew would have to face the sun directly.

Taking into account all these facts, the separation scenario for GFZ-1 was scheduled in the following way:

- separation on April 19, 1995 near the morning terminator which was reached by MIR around 18:45 UT (approximate coordinates 11° S, 150° E near the east coast of Australia); spare dates for separation were agreed for April 22, 24 and 26, but they were finally cancelled to maximise the tracking period;
- first visibility of the satellite for the European laser tracking stations starting at 19:43 UT with at least two consecutive passes illuminated at the beginning.

In any case the contact with the MIR crew during the release of GFZ-1 would have to be carried out via a transponder satellite because the station was far outside the zone of direct radio contact with the MCC. A few days prior to the scheduled release it turned out that the ground station for contact via the foreseen transponder satellite "LUTSCH-2" (deployed at 95° E) failed totally due to an antenna fault which was unrecoverable until April 19. For this reason, it was agreed to shift the moment of separation by about 20...30 minutes into the direction of the evening terminator and to release GFZ-1 near the midday point at 19:12 UT. Here the communication satellite "LUTSCH-1" would be accessible.

To test all the routines once more and to give some training to the station crew, a trash container (COSPAR ID 86017JD) was released from MIR in the morning of April 17, 1995. The crew was able to track this object for about 7 minutes with the on-board laser distance meter and to perform video recordings.

4.2.4 Separation and Early Acquisition of GFZ-1

GFZ-1 was separated from the MIR space station on April 19, 1995 at 19:12 UT (approximate coordinates were 44.6° S, 96.5° W) shortly before crossing the west coast of South America . The laser distance measurements carried out by the station crew showed a separation velocity relative to MIR of about 1.76...1.79 ms^{-1}. A live video transmission of the session was performed as well. There was originally some confusion about the proper work of the separation mechanism: in the transmitted video sequence it seemed at first that after about 60 seconds only one of the head mechanisms was ejected, but the cosmonaut Dezhurov who controlled the separation confirmed the nominal state after a visual control of the situation through a station window. GFZ-1 showed almost no rotation after the release.

Due to the delayed separation with respect to the original schedule, GFZ-1 was not yet

of laser shots directly on the MIR station despite a high veil of cirrus clouds and got a short trace of returns of somewhat unusual shape (a double trace with about 20 cm separation). Later it turned out that these returns were probably from the laser reflectors of the MIR station itself. These reflectors are not intended to be used for laser tracking from the ground, but only for the last phase of approach during a docking manoeuvre by a cargo transporter and are normally not directed to the ground.

During the second pass over Europe that night, GFZ-1 was seen for a short moment in a cloud hole very close to the predicted position by the SLR station Grasse (France). Bad weather prevented any successful laser tracking from Europe during the first hours after separation. The first confirmed laser returns were obtained on April 20, 1995 at 00:21 UT by the U.S. station Greenbelt. During the following days, the stations Graz, Herstmonceux, Santiago de Cuba, Potsdam, Quincy, Maidanak, Monument Peak, Riga, Haleakala und Arequipa joined the tracking. By the end of April, a total of 29 passes was obtained. It turned out that the quality of the predictions generated for tracking after the separation was much higher than previously anticipated.

4.3   Orbit Predictions

4.3.1   Generation of Orbit Predictions

Orbit predictions for GFZ-1 are generated based on

- laser tracking data,
- NORAD twoline-elements,
- state vector information from external sources.

GFZ/D-PAF has gained a good experience in SLR orbit predictions for low altitude targets. Since the Launch of ERS-1 in 1991, GFZ/D-PAF produces high quality acquisition data for the ERS-1, ERS-2, and METEOR-3 satellites.

The generation of orbit predictions (for fundamentals see *König*, [1989]) proceeds in three stages:

- estimation of the orbital model parameters,
- numerical integration for orbit prediction,
- generation of tuned IRVs, SAO-elements, drag functions and twoline-elements.

For orbit prediction generation from laser tracking data, the orbital model parameters are estimated using the dynamic orbit computation program EPOS-OC (Earth Parameter & Orbit System - Orbit Computation). The forces causing orbit perturbations are deduced from Earth's gravity field models, ocean tide models, Earth tide models, solar radiation and air drag models. Earth's high atmosphere is represented by the CIRA'86 model [*Hedin*, 1983], where solar and geomagnetic activity is needed as input. Using 2 ... 4 days worth of laser data as observations, a least squares adjustment process is performed in order to gain a solution for the initial orbit parameters and a global drag coefficient. Occasionally, a global coefficient for the solar radiation pressure is also solved for. In most cases the solar radiation factor is

45

kept fixed if the estimated value looks unreasonable.

The predicted orbit is then computed by forward integration using the parameters derived before and the dynamic modeling as before. Adopted are predicted values for the solar and geomagnetic activity, and for Earth rotation for the prediction period. The inaccuracy of the solar and geomagnetic activity predictions is the major error source for the rapid quality degradation of GFZ-1 orbit predictions. At the higher altitude of ERS-1/2 this effect is 5 to 10 times smaller.

In the third stage, the huge orbit file is compressed and transformed to special forms which are accepted by the international SLR community. The special forms consist of the so-called tuned IRVs, the corresponding drag functions, tuned SAO-elements, and D-PAF twoline-elements. As prediction products the tuned IRVs and the drag functions are delivered to the SLR community. The SAO-elements are sent to users on request only, the D-PAF twoline-elements are for internal purposes only.

The orbit predictions are based on USSpaceCom twoline-elements if no laser tracking data are available, as was the case in May 1995. A description of the twoline-element conversion is given in chapter 5.1.5. The accuracy of thus derived orbit predictions is worse than as if based on laser tracking data.

Orbit predictions based on state vector information from external sources was practiced only before and at the very beginning of the GFZ-1 mission where naturally neither appropriate laser tracking data nor twoline-elements were available.

The IRVs, drag functions etc. are generated and disseminated for the whole prediction period, i.e. 7 ... 10 days in advance. However, due to the high sensitivity of the GFZ-1 orbit to atmospheric drag, the predictions loose accuracy very rapidly. The major errors occur in along-track direction which is known to the SLR stations as time bias, i.e. the satellite rises too late or too early. The GFZ-1 time bias increases very fast. The daily rate of time bias increase is comparable to the weekly rate of ERS-1/2. A polynomial function up to degree 3, known as the time bias function, is generated in order to update the orbit prediction as quickly and frequently as possible and necessary. The parameters of the function are determined in a least squares adjustment using available laser tracking data from the recent days. Some accuracy considerations related to ERS-1 may be found in *König et al.* [1993]. Detailed investigations on the accuracy of GFZ-1 orbit predictions follow in chapter 5.1.3.

4.3.2 Orbit Prediction Products

IRV parameters: Position and velocity of the spacecraft in the pseudo body-fixed system at dedicated epochs (usually 0:00 UTC). One IRV is given for each day. The predicted orbit trajectory can be recovered by running a dedicated orbit integration program using the given IRV set. The IRVs are tuned in order to account for the missing drag model in the integration program.

Drag function: Fourier function accounting for the residuals of the tuned IRV in along-

46

track direction (see chapter 4.1.5). In case of low solar and geomagnetic activity, one drag function is valid during the whole prediction period. In case of high solar and geomagnetic activity, more than one drag function will be required for the whole prediction period.

SAO-elements: Mean orbital elements and long periodic perturbations for the whole prediction period distributed as constant terms, their rates of change and coefficients of trigonometric functions. The reference system is the true equator and mean equinox of date. The orbit trajectory can be recovered by running a dedicated analytical program using the tuned SAO-elements.

D-PAF twolines: Format and meaning according to the NORAD, radar tracking based twoline-elements, generated from the laser tracking based orbit predictions.

Time Bias Function: Polynomial function up to degree 3. As update of the orbit predictions, the time bias function serves as prediction for the deviation in along-track direction of the real orbit trajectory from the predicted orbit trajectory due to mismodelling in the gravity field model and in the atmospheric model.

Examples and format description of the prediction products can be found in Appendix A.

4.3.3 Station Time Bias

At the beginning of the mission the time bias function was generated based on SLR data being about 1 day old due to adopted data transfer procedures. Because of the fast and chaotic evolution of the time bias in some cases, the time bias function lost already pretty much of accuracy at the time of being made available to the SLR stations. Therefore the idea was born for an independent procedure that transfers the time biases observed by the stations themselves around the world as fast as possible. In cooperation with EDC a mail tool has been installed since July 1995 serving for the quick transfer of the station time bias.

Stations which have tracked GFZ-1 send the observed time bias immediately after the pass via e-mail to EDC. The e-mail has the fixed subject "GFZ-1 station time bias" and contains a concise message comprising satellite name, ephemeris number, observation time, observed time bias and observing station name. At EDC a process searches every 15 minutes for e-mails with the appropriate subject and updates a file containing the most recent station time bias reports. The updated file is then immediately sent to all interested stations via e-mail.

In this way, the information of the observed time bias from one station can be forwarded to other parties within very short time, e.g. within one revolution of the satellite. The station time bias adds more information to the time bias function and therefore should give a better estimate of the expected time bias of an upcoming pass to the observer at the SLR station.

47

Due to operational constraints the time bias messages sent by the NASA stations differ from the requested form in that the ephemeris-no is missing. Also the reported time bias comprises the time bias relating to the drag function in contrast to the European reports where the drag function time bias is removed. Currently improvements are in preparation on the NASA side. Nevertheless, since June 1995, the tracking record could be kept sufficiently high by help of the quick station time bias transfer procedure even in daylight tracking phases or in winter.

4.4   The GFZ-1 Post

GFZ/D-PAF also produces and distributes a weekly report named "GFZ-1 Post" to the SLR community. The report contains two permanent topics and other topics as required. One permanent topic is the SLR tracking status. It gives an overview of the acquired passes during the previous week. Passes which don't have the nominal normal point window of 5 s bins are flagged and commented. The overview serves as encouragement and promotion to the SLR stations to give more efforts at tracking GFZ-1. It also gives the stations the possibility to check if all passes tracked are listed. Some passes which disappeared on the way to the data centers could be recovered thanks to the comparison with the overview. The second permanent topic is the status of orbit predictions. Predictions and time bias functions distributed since the previous week are listed. Stations can check if they have received all prediction informations.

Other topics are depending on opportunity. News (e.g. informations on the separation of GFZ-1 from MIR) or changes (e.g. numerical adaptation of the COSPAR satellite ID) are contents of the "GFZ-1 Post". Also errata go into other topics. In the following, four important topics are summarized.

The Fourier drag function (see chapter 4.1.4) was first presented at the EUROLAS meeting in March 1995. At the end of March 1995, it was introduced to the SLR community via the "GFZ-1 Post". After receiving some comments, the description of the drag function has been improved and two FORTRAN subroutines for the evaluation of the time bias from the Fourier drag function were sent to the community.

Around GFZ-1's COSPAR-No. there were brisk discussions which were compiled in the reports. The original COSPAR-No. given for GFZ-1 is 86017JE which considers GFZ-1 being a part of the MIR space station, but this does not reflect the correct circumstances of the GFZ-1 launch. Due to SLR data format specifications this number has to be transformed into a pure, 7-digit numerical number. The NASA network initially used the number 8601799 which did not find the complete agreement by the SLR community. GFZ proposed to use 8601795 which preserves the launch year of GFZ-1 and leaves options free for any satellites separated from the MIR space station in the future. Finally the community agreed upon 8601795, the number being applied throughout the SLR world since May 11, 1995.

In May 1995, GFZ-1 went through the first daylight tracking period for all stations on the Northern hemisphere. Due to the poor accuracy of the orbit predictions and due to the lack of experience in tracking GFZ-1 in daylight, tracking amount decreased to zero. Under coordination of GFZ/D-PAF, on May 4, a small search campaign with a few European stations was executed. Although the experiment was not successful, this was the first attempt

48

ever to coordinate and share search procedures among different institutions.

The quick station time bias transfer (see chapter 4.3.3) was realised in July 1995. In the first two months, the procedur was in test mode with a few European stations participating. The success in acquiring nearly 100 passes in July when GFZ-1 was in daylight on the Northern hemisphere, was mainly a result of this campaign. End of August, the tool was announced to the SLR community. Riga and several NASA stations with Internet connection joined in this net.

5. LASER TRACKING AND PRECISE ORBIT DETERMINATION

5.1 Tracking Issues

5.1.1 Immanent Tracking Problems

The time of the separation of GFZ-1 from the MIR space station was chosen so, that the European SLR stations were able to visually acquire the satellite in case the orbit predictions would have been of insufficient accuracy. For more than a week GFZ-1 was crossing the evening terminator while overflying Europe meaning the stations had optimal dusk/ nighttime ranging conditions and in addition the satellite was lit by the sun. On the Northern hemisphere in general all GFZ-1 passes occured during nighttime providing good tracking conditions.

During May 1995, GFZ-1 was in daylight most of the time at all stations in the Northern hemisphere. In June 1995, the passes occured at night again. The day/nighttime tracking schedule for 1995 is shown in Figures 5.1.1.1 and 5.1.1.2 for the SLR stations Potsdam and Yarragadee as examples.

In Figures 5.1.1.1 and 5.1.1.2, nighttime is shaded. The passes are marked by crosses or squares, where the squares indicate passes being illuminated at least partly by the Sun and thus visually accessible.

The figures show that there are monthly periods between day and nighttime tracking. The acquisition becomes particularly difficult during the daylight. A good orbit prediction accuracy required to support daylight ranging can only be maintained if the SLR network acquires an adequate number of passes. Figure 5.1.1.2 shows opposite day/nighttime periods with respect to Figure 5.1.1.1. Thus, nighttime acquisition periods alternate between the stations in the Northern and Southern hemispheres. Therefore, the Southern stations play an important role in the mission.
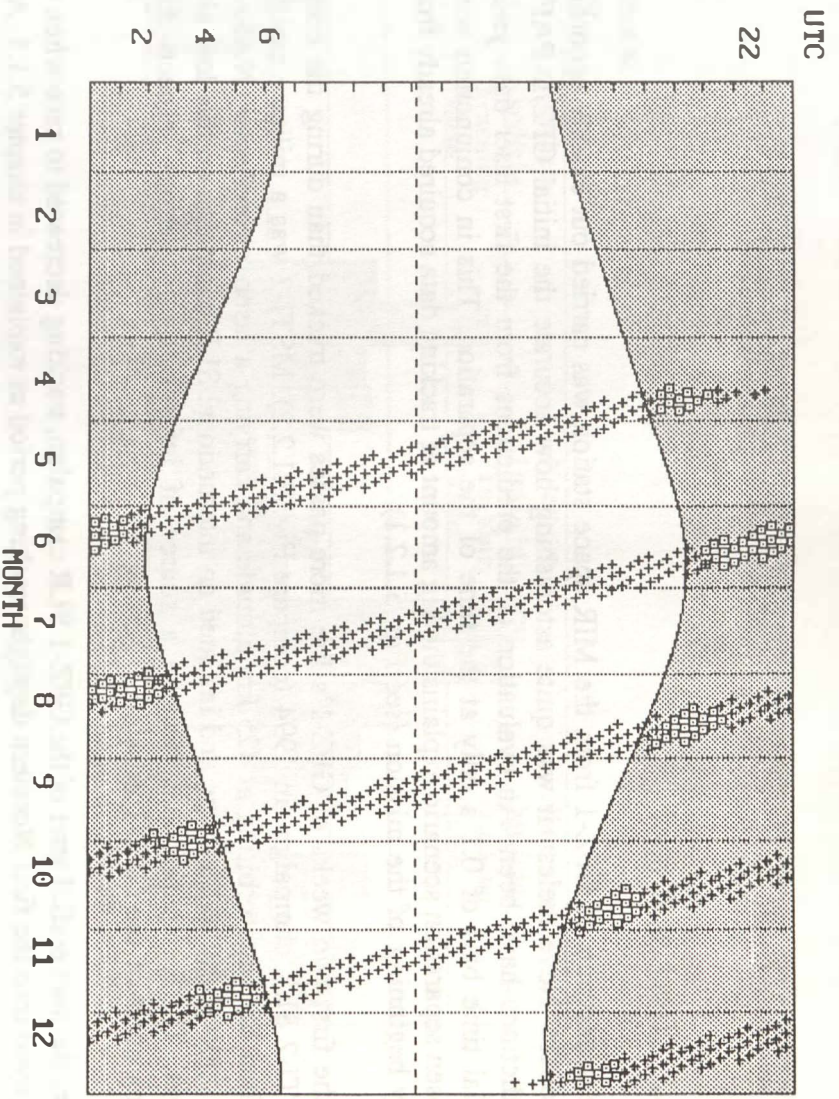
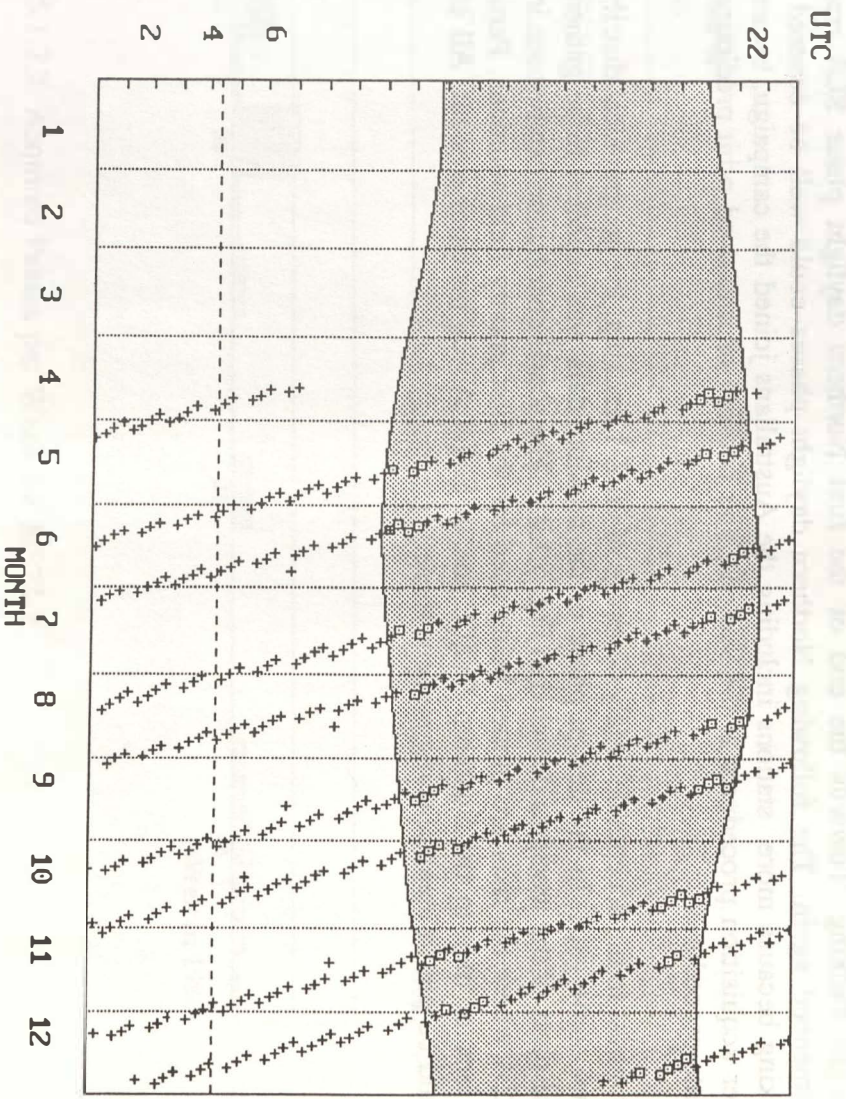50

Figure 5.1.1.1: Day/Nighttime Passes over Potsdam in 1995

Figure 5.1.1.2: Day/Nighttime Passes over Yaragadee in 1995

51

5.1.2   Tracking Record

The separation of GFZ-1 from the MIR space station was carried out exactly according to schedule. Nevertheless it was quite astonishing how accurate the initial GFZ/D-PAF orbit predictions have been. An evaluation of the predictions from the first laser data yields an initial time bias of 0.1 s only at the time of the separation. This in conjunction with the chosen separation scenario explains the big amount of tracking data acquired already from the very beginning of the mission (see Fig. 5.1.2.1).

In the first two weeks of GFZ-1's life more passes were tracked than during the complete MSTI-2 SLR campaign in 1994 (compare Fig. 5.1.2.2). MSTI-2 was a military satellite of limited life time orbiting at 425 km altitude and carrying a laser retroreflector. NASA took the opportunity at that time and initiated an international SLR campaign on this low altitude target. The campaign thus became a source of information in various respects for the preparation of the GFZ-1 mission.

After the successfull start of the GFZ-1 SLR campaign, tracking decreased to zero when GFZ-1 moved into the first Northern daylight tracking period as explained in chapter 5.1.1. At that time the Australian government had not yet given the allowance for GFZ-1 tracking on the Australian continent. Therefore supporting tracking data from the Southern hemisphere was missing and the orbit predictions could not be generated with an accuracy nesessary for daylight tracking. Towards the end of the first Northern daylight phase SLR tracking commenced again. The following Northern daylight phases could well be covered with tracking because more stations including the Australians joined the campaign, because of better acquisition procedures at the stations, and because of improved orbit prediction and update procedures.

In contrast to the acceptable timely coverage of GFZ-1 tracking, the geographical distribution shows some gaps. In the design phase of the mission, data was expected to be gathered in those parts of the world as depicted in Fig. 5.1.2.3. The actual distribution can be seen in Fig. 5.1.2.4 where the data are plotted being used for the first gravity field solutions. Particular the lack of data in the Southern Pacific and in South Africa becomes evident. All efforts should be put in reestablishing stations there.

52

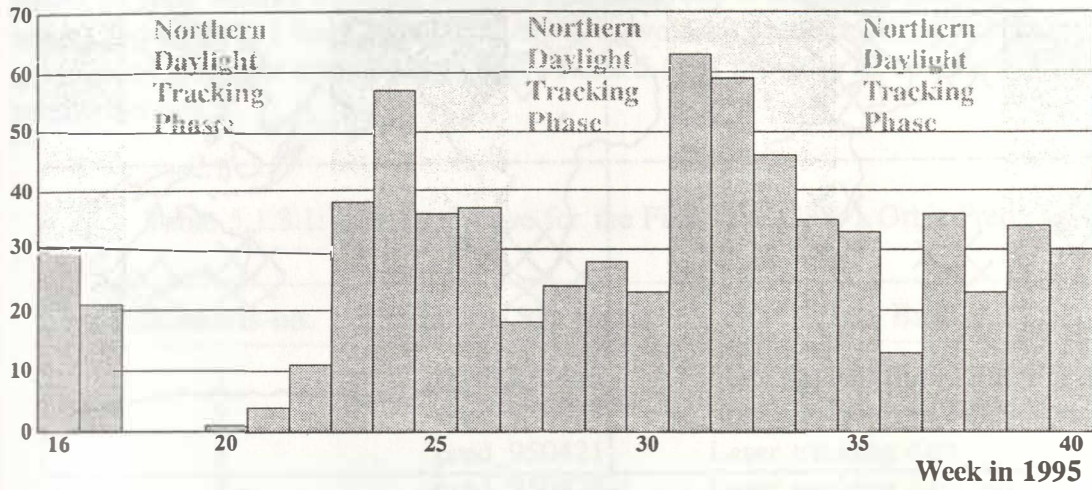Figure 5.1.2.1: Acquired Passes per Week for GFZ-1
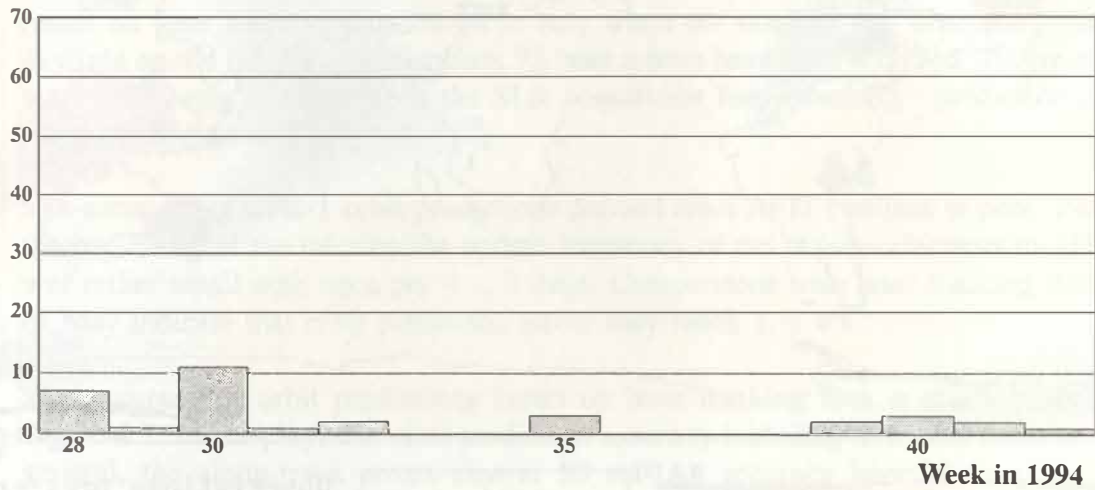

Figure 5.1.2.2: Acquired Passes per Week for MSTI-2

53
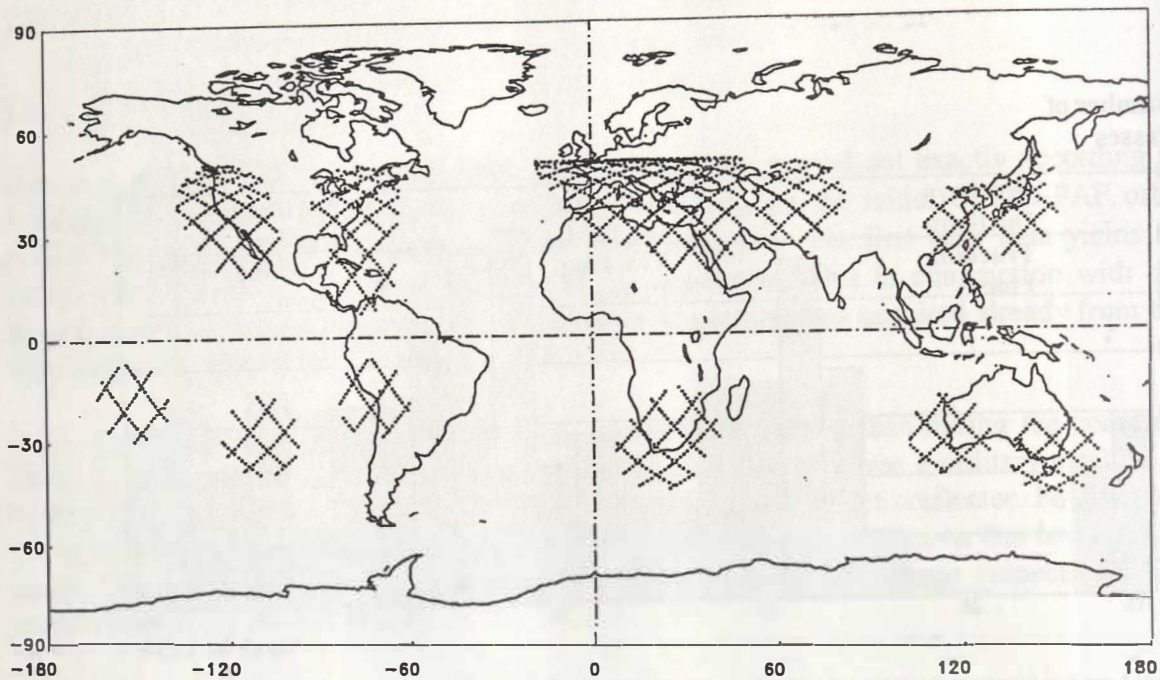
Figure 5.1.2.3: Expected Geographical Tracking Distribution

Observations prc1-prc8
DATA: grim4s4_10do
TIME: Wed Nov 8 19:12:37 MET
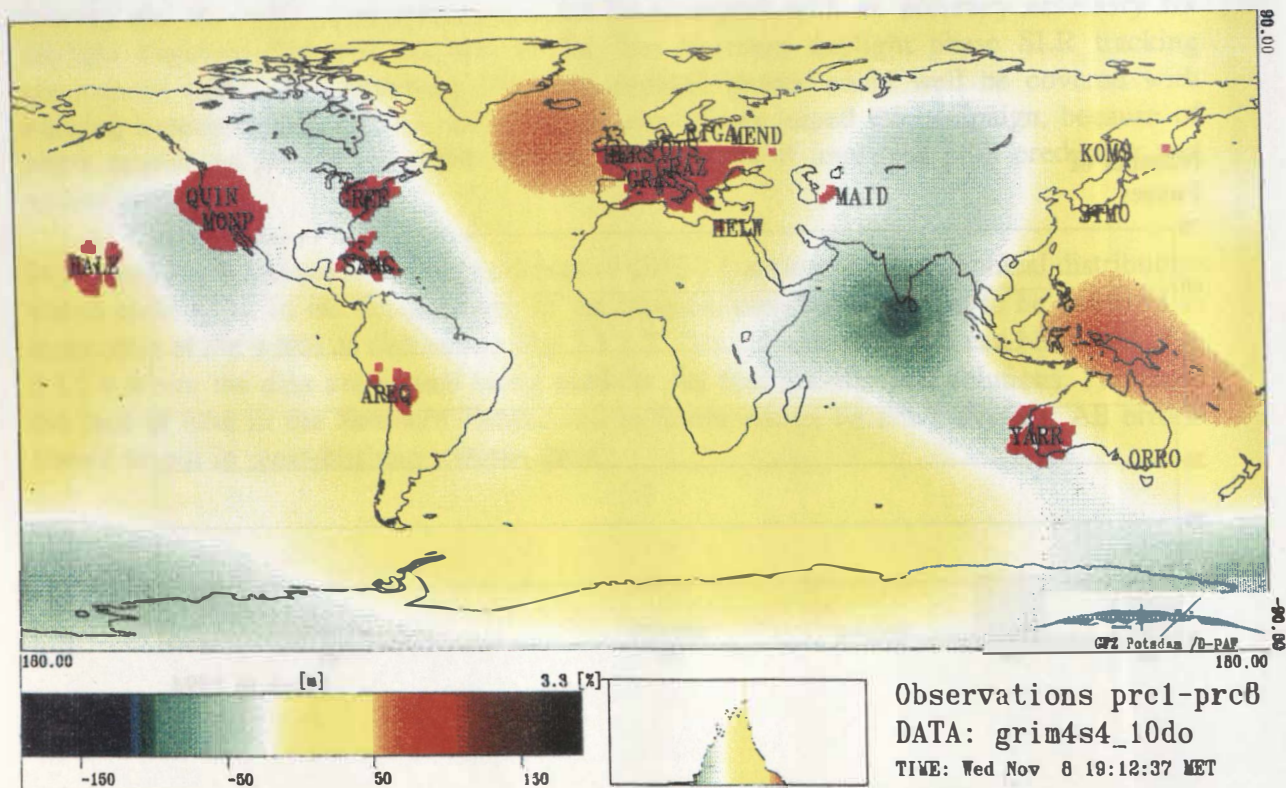
Figure 5.1.2.4: Achieved Geographical Tracking Distribution for the first 8 Precise Orbits
Observations in pink, geoid heights underlying according to colour table

54

5.1.3 Prediction Accuracy

The first two orbit predictions sets for GFZ-1 sent out to the SLR community were generated based on state vectors from the Russian ballistic group at RKK Energia. After the successfull separation of GFZ-1 from space station MIR, two orbit predictions (ephemeris-no. 3,4) were generated from laser tracking data only. Table 5.1.3.1 provides an overview of the first few prediction sets.

Table 5.1.3.1: The Data Base for the First Five GFZ-1 Orbit Predictions

Ephemeris-no.	Prediction Set Name	Data Base
1	pred_950418	State vector from RKK Energia
2	pred_950419	State vector from RKK Energia
3	pred_950421	Laser tracking data
4	pred_950428	Laser tracking data
5	pred_950505	AFIT twoline elements

In May the satellite was observable during daylight only on the Northern hemisphere. 10 passes were tracked, most of them at the end of the month (see tracking statistics in chapter 5.1.2 above). So during May all orbit predictions (ephemeris-no. 5-12) were generated based on AFIT twoline elements.

In June the acquirable passes occured in the night again on the Northern hemisphere. The amount of tracked passes increased largely. Since then all orbit predictions are generated based on laser tracking data. Even in July when the satellite was observable solely during daylight on the Northern hemisphere, 98 laser passes have been acquired. This tracking record was sufficiently dense to keep the SLR acquisition loop (tracking - prediction generation - tracking etc.) going.

The accuracy of GFZ-1 orbit predictions derived from AFIT twolines is poor. Particularly at the beginning of the mission the update frequency of the twoline elements by USSpaceCom was rather small with once per 4 ... 8 days. Comparisons with laser tracking data at the end of May indicate that orbit prediction errors may reach 1 ... 4 s.

The accuracy of orbit predictions based on laser tracking data is much better in general. Figure 5.1.3.1 displays the orbit prediction accuracy including time bias function updates. In general, the along-track errors size at 50 ms. An accuracy improvement can be noticed starting July when the frequency of orbit prediction generation has been increased from one to two or three times per week. Also the gravity model was changed from GRIM4S4 to JGM3 or PGM056 or PGM057 (the first gravity field solutions from GFZ-1 data).

The errors of GFZ-1 orbit predictions are mainly caused by errors of the gravity field models and errors of the predicted atmospheric models. Whereas the gravity field models will be steadily improved, the dominant factor for the limited quality of orbit predictions derives from

55

the uncertainties of the atmospheric models. In the following, the influence of the atmospheric models on GFZ-1 orbit predictions in July and August 1995 are investigated.
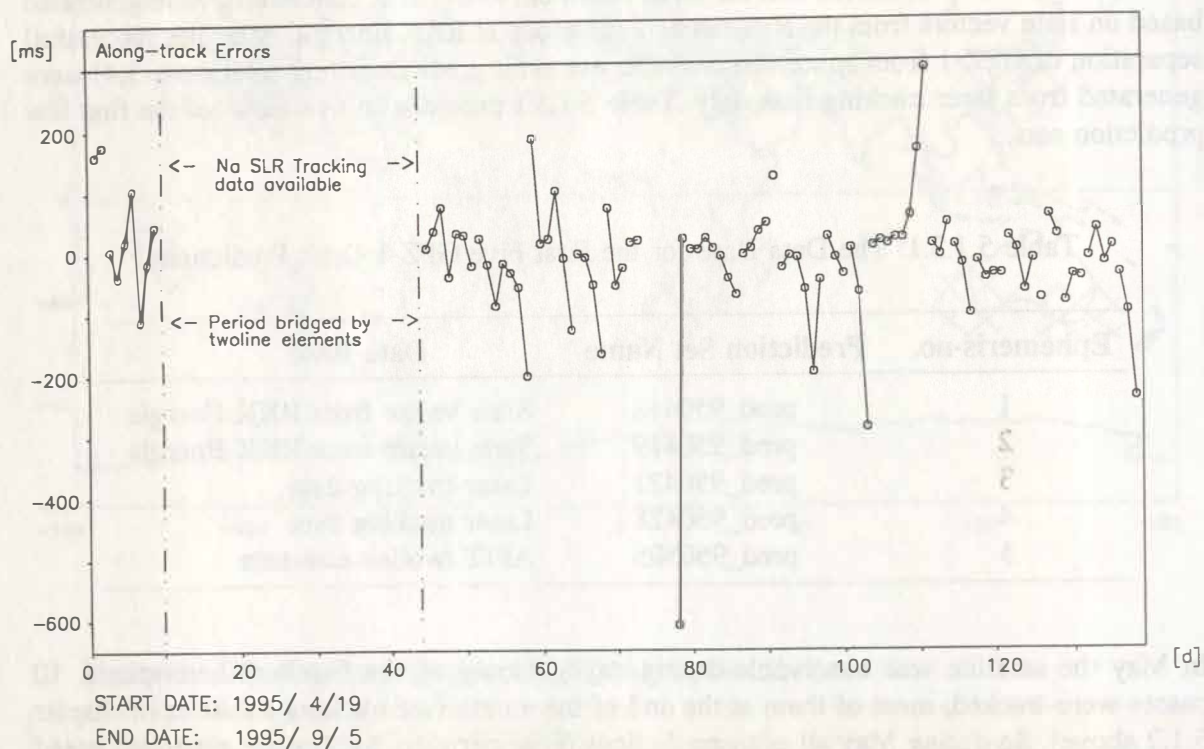
Figure 5.1.3.1: Accuracy of Orbit Predictions

Figure 5.1.3.2 shows the geomagnetic and solar activity in terms of a_p values and daily solar fluxes as well as their prediction accuracies during the investigation period. These activities are part of the low phase of the solar cycle. In July only two peaks showed up in the a_p values whereas in August the a_p time series is more rugged. The a_p errors are almost as large as the a_p values itself. Also large a_p errors are strongly correlated with large a_p values. The solar flux errors are relatively small and the errors in July appear smaller than in August. The accuracies of the activity predictions are good from the viewpoint of orbit prediction accuracy for satellites at higher altitudes like ERS-1/2 or Meteor-3. In case of GFZ-1 this causes serious problems in orbit prediction generation.

Figure 5.1.3.3 shows the GFZ-1 orbit prediction accuracies where the daily time bias function updates are not considered together with the a_p and flux prediction errors. A correlation between the swift increase of the time bias on one side and the errors of the a_p values and the errors of the flux data on the other side can be found. This is the reason why the time biases in July are smaller than in August.

Figure 5.1.3.4 shows the effect of the uncertainties of the predicted a_p values and flux data on the time bias development more distinct. The time biases developing from predicted a_p and flux are drawn in black and those developing from final observed values in grey. Using the final values leads to reduced time biases in most cases. Particularly for ephemeris-no. 25 and 32 the improvements are drastic.

56
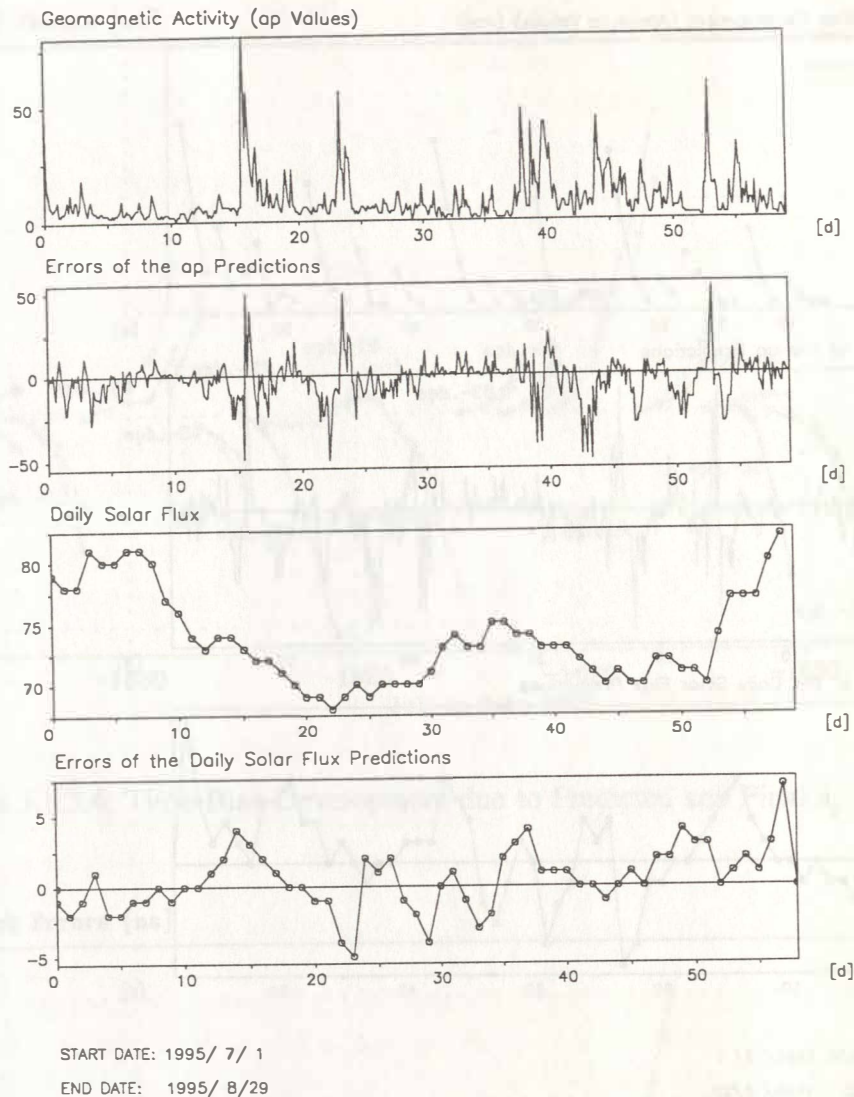
Figure 5.1.3.2: Geomagnetic and Solar Activity and Their Prediction Errors

For some emphemeris, e.g. no. 36 and 37, the final a_p and flux parameters driving the atmospheric model do not lead to better results. The reason comes from the strong fluctuations of the a_p values either in the period where the laser tracking data is used to derive the parameters for the orbit prediction or in the prediction period itself. Thus the global coefficient for atmosphere drag (c_d) estimated from the laser tracking data is no more representative for the prediction period. A few examples can be found in Figure 5.1.3.4. F.i. a geomagnetic storm occured in the period of laser data adjustment of ephemeris-no. 36 and in the prediction period of ephemeris-no. 37, yielding exceptional large time bias developments.

However, there is a way to reduce the time bias for cases like in ephemeris-no. 37. Simply by starting the laser arc one day later the geomagnetic storm at the beginning of the laser arc can be avoided. Figure 5.1.3.5 shows the time bias development depending on laser arc length. The solid black lines represent the time biases of the original orbit predictions based on 3 ... 4 days worth of laser tracking data. The dashed grey lines represent time biases of

57
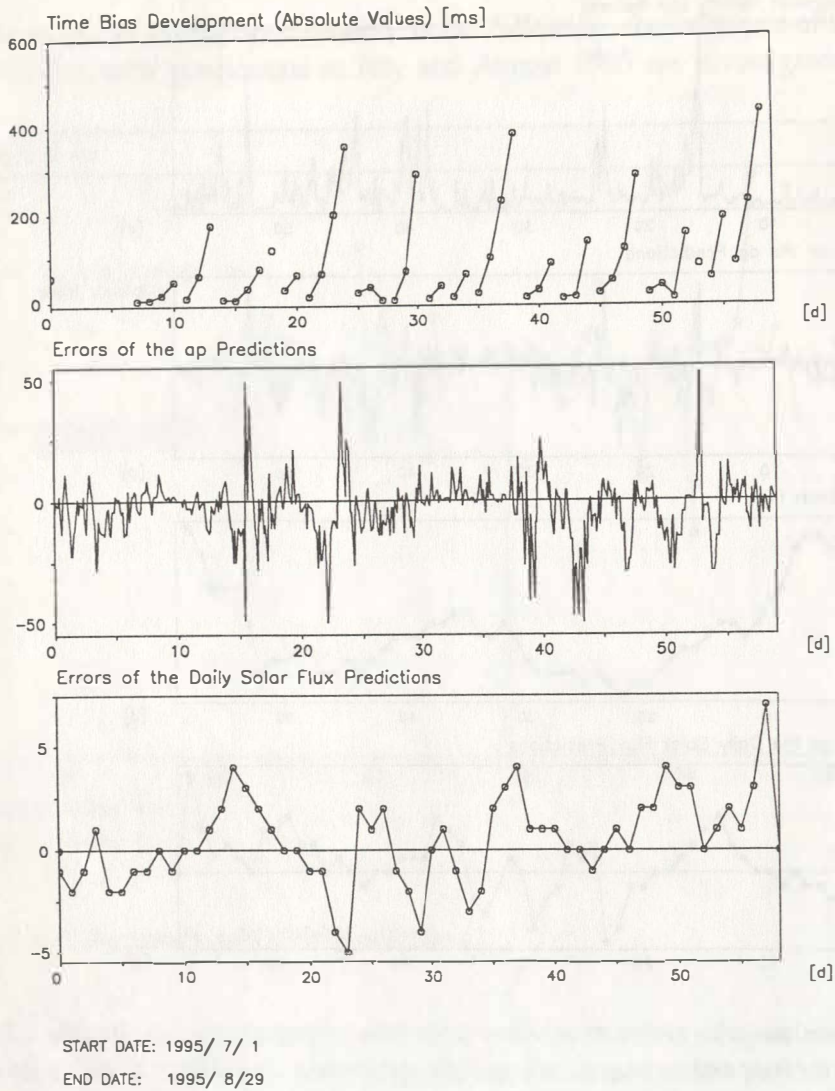
Figure 5.1.3.3: Time Bias Development and Activity Prediction Errors

orbit predictions from 2 ... 2.5 days laser arcs where the first day of the original data set has been cut off. For ephemeris-no. 23, 35, and 37, smaller time biases are achieved, because peaks of geomagnetic activity in the period of laser data adjustment could be escaped.

All in all, GFZ-1 orbit predictions are extremely sensitive to fluctuations of the a_p values and to the prediction errors of the a_p values and of the solar flux. Any peaks in the a_p series as well as small errors can give rise to large time biases. A practical way to keep the time bias within certain limits is to keep the orbit prediction period short and to update the predictions as frequent as possible.

58

Along-track Errors [ms]
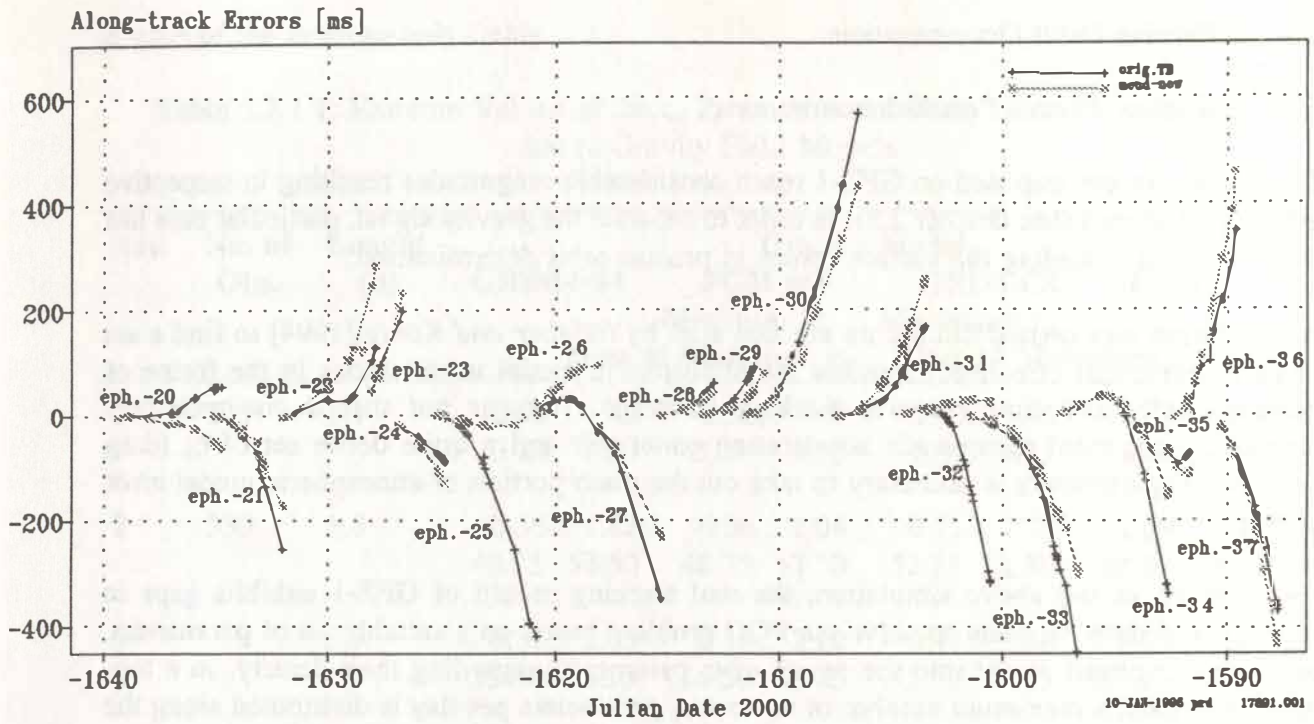
Figure 5.1.3.4: Time Bias Development due to Predicted and Final a_p

Along-track Errors [ms]
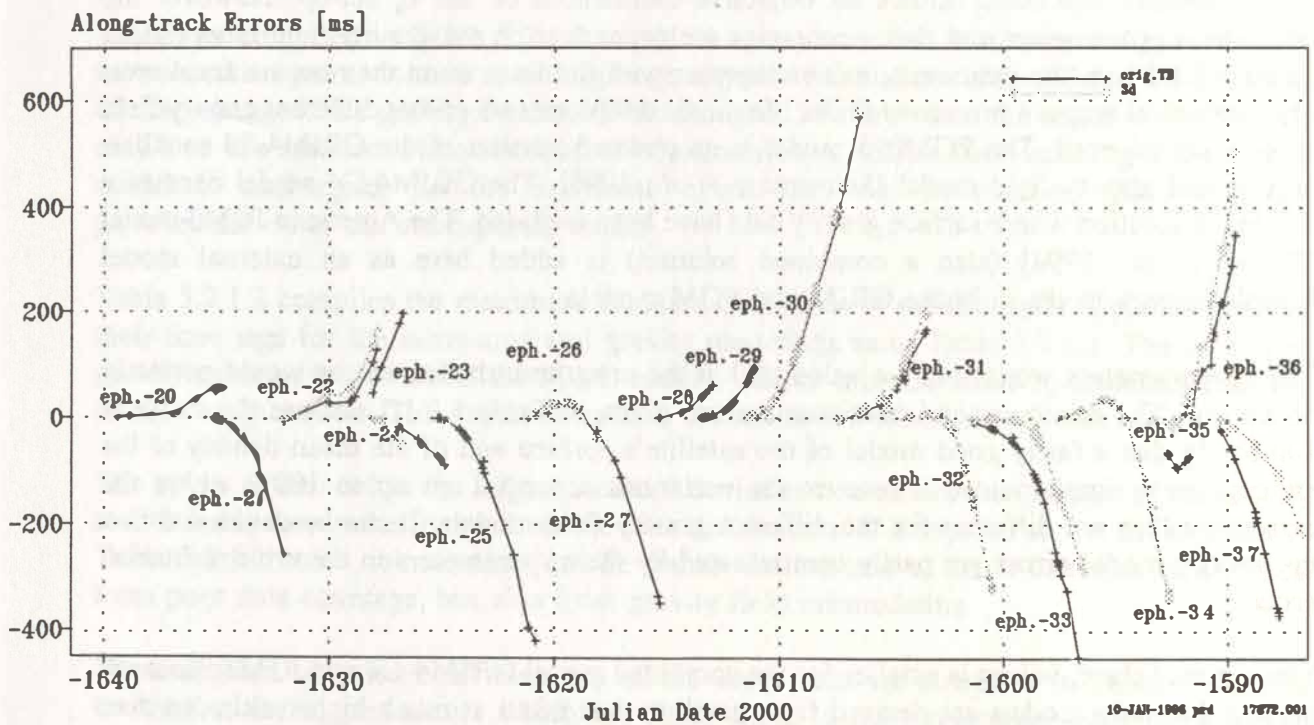
Figure 5.1.3.5: Time Bias Development due to Laser Arc Length

59

5.2   Precise Orbit Determination

5.2.1   Surface Forces Parametrization

The surface forces imposed on GFZ-1 reach considerable magnitudes resulting in respective orbit perturbations (see chapter 2.3). In order to separate the gravity signal, particular care has to be taken in modeling the surface forces in precise orbit determination.

A simulation was carried out before mission start by *Reigber and König* [1994] to find a set of parameters that effectively handles the atmospheric model uncertainties in the frame of geographically and timely sparse tracking coverage. It turns out that a one-cycle-per-revolution empirical along-track acceleration parameter and a quite dense set of c_d (drag coefficient) parameters is necessary to take out the main portion of atmospheric model error effects.

As expected in the above simulation, the real tracking record of GFZ-1 exhibits gaps in location and time. In order to solve the POD problem based on a suitable set of parameters, particular emphasis is put into the set-up of c_d parameters regarding their density. In a top-down approach a maximum number of up to 4 c_d parameters per day is distributed along the arc where observations guarantee the solveability. After the first solution the c_d parameters are checked for significance and accuracy. The most spurious c_d is cancelled and the process repeated until an optimal solution in terms of accuracy and orbital fit is found.

The procedure described allows an objective assessment of the c_d set-up. However the estimated c_d parameters and their accuracies are dependent on the gravity field model used. Table 5.2.1.1 lists the extreme c_d values together with the time when they occure for 4 arcs. The individual arcs are processed under identical conditions except that different gravity field models are adopted. The PGM055 model is an updated version of the GRIM4-S4 satellite-only global gravity field model [*Schwintzer et al., 1995*]. The GRIM4-C4 model denotes a combined solution where surface gravity data have been included. The American JGM3 model [*Tapley et al.,* 1994] (also a combined solution) is added here as an external model complementary to the in-house GRIM and PGM models.

The c_d parameters would obey a value of 1 if the orbit perturbation forces would perfectly be known. The minimum and maximum values given in Table 5.2.1.1 enclose the value of 1 showing that a fairly good model of the satellite's surface and of the mean density of the atmosphere is implemented. However the variations around 1 go up to 100% where the extreme values are different for the different gravity field models. It can be concluded that the gravity model errors are partly compensated by the c_d parameters in the orbit restitution process.

The range of the c_d values is smaller for the combined model GRIM4-C4 and JGM3. Because the satellite-only models are derived from satellite data taken at much higher altitudes than GFZ-1's altitude and because the combined models include gravity data from the Earth's surface, the combined models should better reflect the gravitational impact on GFZ-1's orbit. Therefore the c_d parameters have to compensate less of the gravity model error effect than in case of the satellite-only fields.

60

in case of the satellite-only fields.

Table 5.2.1.1: Extreme Values of the c_d Parameters and Their Time of Occurence
due to Gravity Field Models

Arc	No. of Obs.	Lenght (d)	Gravity Model			
			GRIM4-S4	PGM 055	GRIM-C4	JGM3
			Minimum c_d ... Maximum c_d			
			Time of Minimum c_d		Time of Maximum c_d *)	
1	775	6.1	0.56... 1.46	0.56... 1.49	0.90... 1.36	0.92... 1.31
			3.25 3.50	3.25 3.50	2.50 2.25	6.00 4.00
2	530	5.8	0.56... 1.82	0.56... 2.04	0.71... 1.78	1.09... 1.42
			48.75 53.50	48.75 53.50	52.75 52.50	48.00 53.50
3	759	5.9	0.31... 2.03	0.18... 2.12	0.71... 1.58	0.95... 1.42
			55.50 55.25	55.50 55.25	55.50 55.25	57.75 54.25
4	723	5.8	0.09... 2.07	0.06... 2.18	0.64... 2.00	0.69... 1.62
			65.50 61.25	65.50 61.25	65.75 61.25	65.75 61.75

*) The times are given in days since JD 2449826.5

The times compiled in Table 5.2.1.1 reveal in some cases that minimum and maximum c_d are successive points in time revealing large negative correlations among them. These points of time change if the gravity field model is changed. In a few cases the negative correlations may lead to a saw-tooth like distribution of successive c_d values also vanishing if the gravity model is exchanged. So the saw-tooth effect may not be deduced from an over-parametrization of the atmospheric model.

Table 5.2.1.2 compiles the maximum standard deviations of the estimated c_d parameters and their time tags for the same arcs and gravity modelings as in Table 5.2.1.1. The combined gravity models, in particular the JGM3 model, deliver more accurate c_d estimates than the satellite-only models. This result completes the statements made already above.

The points of time when the largest standard deviation occurs, are independent of the gravity model used, they rather depend on the data distribution. If compared to the times given in Table 5.2.1.1 some coincidences can be found. An extreme c_d could therefore be deduced from poor data coverage, but also from gravity field mismodeling.

The estimated radiation coefficients c_r of the above runs are compiled in Table 5.2.1.3. In contrast to the c_d parameters which are fairly close to the expectation value of 1, the c_r parameters deviate largely from 1 and vary from arc to arc and from gravity model to gravity model. Most values are significant estimates. So it can be concluded that the c_r parameters are influenced by errors of the gravity field models as is the case for the c_d parameters. For POD purposes it might be necessary to abandon the estimation of a c_r parameter in case large or negative values show up. Trials show that the orbital fit is hardly affected by fixing

61

c_r to 1. The gravity model error effect is then shifted into the estimates of the initial orbital elements.

Table 5.2.1.2: Maximum Standard Deviations of the c_d Parameters and Their Time of Occurence due to Gravity Field Models

Arc	No. of Obs.	Lenght (d)	Gravity Model			
			GRIM4-S4	PGM055	GRIM4-C4	JGM3
			Maximum Standard Deviation of c_d			
			Time of Maximum Standard Deviation of c_d *)			
1	775	6.1	0.049	0.056	0.021	0.011
			2.50	2.50	2.50	2.50
2	530	5.8	0.093	0.098	0.086	0.034
			52.75	52.75	52.75	52.75
3	759	5.9	0.107	0.083	0.039	0.027
			56.25	59.75	59.75	59.75
4	723	5.8	0.141	0.151	0.082	0.039
			61.25	61.25	61.25	61.25

*) The times are given in days since JD 2449826.5

Table 5.2.1.3: Estimates of c_r and Their Standard Deviations due to Gravity Field Models

Arc	No. of Obs.	Length (d)	Gravity Model			
			GRIM4-S4	PGM055	GRIM4-C4	JGM3
			Estimate of c_r			
			Standard Deviation of c_r			
1	775	6.1	0.9	2.1	5.0	7.5
			±1.7	±1.9	±0.7	±0.3
2	530	5.8	-11.6	-11.2	2.6	4.7
			±0.5	±0.6	±0.5	±0.2
3	759	5.9	17.4	20.2	11.0	10.8
			±1.4	±1.5	±0.7	±0.4
4	723	5.8	-16.0	-15.8	2.1	-1.7
			±0.6	±0.7	±0.4	±0.3

The conclusions drawn above may not be transfered to the gravity solution process. In this case the gravity field coefficients are also solved for. These parameters should then account for the gravity model errors and therefore take away the effect on c_d and c_r estimates.

5.2.2   Atmospheric Models

It was shown in chapter 2.3 that atmospheric models adopted for POD purposes are accurate to only about 25%. A priori simulations by *Reigber and König* [1994] gave confidence in that the atmospheric model errors can effectively be taken into account by a proper set-up of the parameters in the GFZ-1 POD task.

Table 5.2.2.1 summarizes the orbital fits in terms of RMS values of the laser observations for the arcs and the gravity field models already introduced in chapter 5.2.1 above. All runs are carried out under identical conditions except that either the atmospheric model CIRA'86 [*Hedin*, 1983] or either the atmospheric model DTM [*Barlier et al.*, 1978] is adopted.

As in the previous chapter, the combined gravity field models perfom better, now in terms of orbital fit. A more detailed discussion on this follows in chapter 5.2.3. Here particular emphasis is drawn on the differences of orbital fits due to different atmospheric models. In general the CIRA'86 models deliveres slightly smaller RMS values than DTM does. Because the differences of the RMS values between the different atmospheric model implementations are in the centimeter level, the adjacent restituted orbits are essentially identical where observations are given. So the chosen parameter set indeed takes care of the atmospheric model errors.

Table 5.2.2.1: Orbital Fits due to Atmospheric Models

Arc	No of Obs.	Lenght (d)	GRIM4-S4	PGM055	GRIM4-C4	JGM3
			Gravity Model			
			Laser RMS (cm) from CIRA'86			
			Laser RMS (cm) from DTM			
1	775	6.1	259.5	294.1	112.9	47.7
			258.9	294.4	110.7	46.9
2	530	5.8	106.5	111.8	98.3	37.6
			111.0	116.7	99.2	35.0
3	759	5.9	228.9	259.8	121.2	72.7
			233.4	264.8	124.8	72.9
4	723	5.8	128.5	137.5	74.9	51.9
			127.2	136.8	73.7	51.9
1-4			192.1	215.3	103.3	54.0
			193.6	217.4	103.8	53.5

Of course the estimated c_d parameters are not of the same value for the different atmospheric model implementations. Figure 5.2.2.1 displays the c_d values for the CIRA'86 and for the DTM case computed most accurately on the basis of the JGM3 gravity model. The results of arc 1 fill the plot at the beginning of the time axis. A gap of about 40 days follows and at last the results of arcs 2 ... 4. The c_d series from CIRA'86 and from DTM show similar behaviour over some parts in time which can numerically be confirmed by a correlation coefficient of 0.5. So the density variations of the atmosphere are modeled similar in both applications. The c_d estimates from CIRA'86 are larger by about 25% in general than those from DTM which denotes the overall disagreement between both atmospheric models regarding a mean atmospheric density.
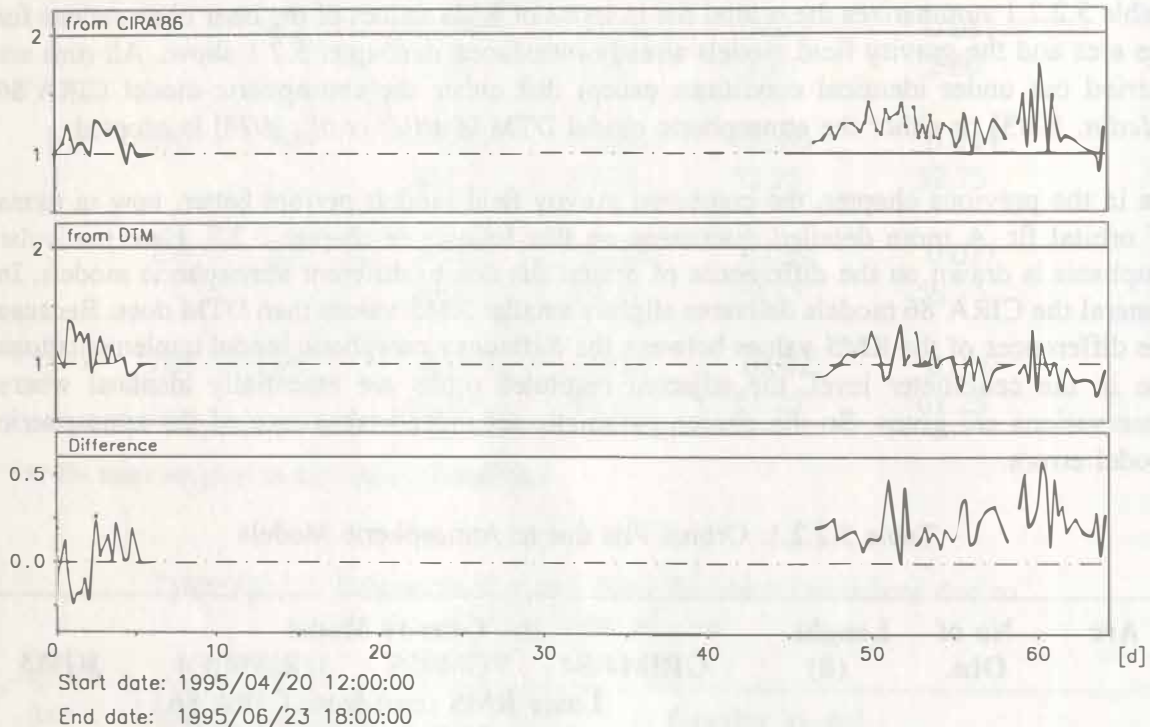
Figure 5.2.2.1: c_d Estimates due to Atmospheric Models

Summarizing the above, either atmospheric model is suitable in the POD task as long as a sufficiently dense tracking record provides the data required for a proper adjustment of the surface forces parameters. Particularly if the c_d parameters are carefully set up, a degradation of the orbit restitution induced by atmospheric model errors may not be expected.

5.2.3 Gravity Field Models

Up-to-date satellite-only gravity field models, as f.i. the GRIM4-S4 model already introduced in chapter 5.2.2 above, are derived from satellite data above 800 km altitude. Combined gravity field models, as f.i. GRIM4-C4 (see also above), are additionally based on gravity data taken on the Earth's surface. The GFZ-1 mission delivers data from an altitude of 400 km which is right in between the Earth's surface and the lowest altitude of satellites included

64

in recent gravity field models.

In POD the available gravity field models will therefore not provide the correct gravitational orbit perturbations exerted on GFZ-1. It may be expected that the combined gravity models will yield better orbital fits than the satellite-only models will. This feature flashed up in chapter 5.2.2 above. A more thorough compilation is given in Table 5.2.3.1. All together 11 arcs are processed based on data over the period April to August 1995 where tracking coverage is sufficiently dense.

Table 5.2.3.1: Orbital Fits due to Gravity Field Models

Arc	Gravity Model			
	GRIM-4-S4	JGM2-S	GRIM4-C4	JGM3
	Overall Laser RMS (cm)			
1-11	201.4	148.0	106.1	51.2

The arcs are 3.1 ... 6.6 days long. The parameters solved for in each arc are the initial state, one c_r parameter, 1 ... 4 c_d parameters per day, and two empirical once-per-revolution along-track parameters. Appr. 8,100 laser range observations contribute to the solutions. The RMS values are derived from the residuals of the ranges to the adjusted orbits.

Table 5.2.3.1 comprises in addition to the gravity field models introduced already above, the American JGM2-S satellite-only model. As can be seen, the combined models perform much better than the satellite-only models. Also the external JGM models provide better orbital fits than the in-house GRIM models. In particular JGM3, which is widely considered to be the state-of-the-art model in geodesy these days, turns out best at the half meter level. The gravity models investigated are independent of GFZ-1. In chapter 6 below GFZ-1 data have been included in a first new satellite-only gravity field solution resulting in a drastic improvement of orbital fits from formerly 2 m to the meter level.

Because the combined gravity models show better results in POD, an attempt is made to make use of high resolution models: the external American OSU91a model [Rapp et al., 1991] and the in-house GFZ95a model [Gruber et al., 1996]. In order to compare the results to those above, the long-wavelenght part only, i.e. up to degree/order 70 of the gravitational spectrum, is extracted. In proceeding so, the correlations with the short-wavelength part of the models are neglected.

In order to get a feeling for the impact of these correlations, Table 5.2.3.2 also compiles the results for degree/order 100 and 150 adoptions. An extension of the investigations to the full resolution of degree/order 360 is omitted due to processing restrictions.

65

Table 5.2.3.2: Orbital Fits due to High Resolution Gravity Fields

Arc	Gravity Model		
	Spherical Expansion Degree × Order	GFZ 95a	OSU 91a
		Overall Laser RMS (cm)	
1-8	70 × 70	109.1	94.7
	100 × 100	111.9	95.6
	150 × 150	113.9	99.4

The degree/order 70 application yields results comparable to those of Table 5.2.3.1 before. The reason can be deduced from the fact that the high resolution models are based on low degree/order gravity fields in the long-wavelenght part comparable to the gravity fields used in Table 5.2.3.1.

As the extraction of the gravitational spectrum is increased to higher degrees/orders, the orbital fit gets worse. Obviously now errors build up due to the neglection of the correlations among high degree/order constituents and due to a deminishing influence of the long-wavelength basis. The full spherical expansion of degree/order 360 should be adopted to get adefinite number of orbital fits obtainable by high resolution gravity models.

66

6. GLOBAL GRAVITY FIELD MODEL IMPROVEMENT WITH GFZ-1 LASER DATA: FIRST RESULTS

In order to evaluate GFZ-1's potential to improve state-of-the-art global gravity field models, GFZ-1 laser ranging data obtained during the period April 19 to July 27, 1995, were processed and incorporated into the latest GRIM4-S satellite-only global gravity field model PGM055 to yield a new model enhanced by the GFZ-1 contribution: PGM061.

This study is restricted to give an idea of the impact of GFZ-1 data on satellite-only gravity field solutions, i.e. being derived solely from satellite tracking data and not employing surface gravity data and altimeter sea surface observations. The rationale for this procedure is to get a better insight into the contribution of GFZ-1 data, especially within the spectral domain of the gravitational geopotential, and the need of satellite-only geoid models for sea surface topography modelling using altimeter data.

6.1 Data Basis, Solution Strategy and Solve-For Parameters

About 2.8 millions micro-wave, laser, camera and altimeter cross-over observations of a total of 34 satellites are exploited to generate the latest pre-GFZ-1 version of the GRIM4 satellite-only global gravity field model series, accomplished by a joint German/French effort [*Schwintzer et al.*, 1991, 1992]. This solution is internally called PGM055 and differs from the GRIM4-S4 model [*Schwintzer et al.*, 1995] by the inclusion of more ERS-1 laser and altimeter cross-over data. Table 6.1 gives a complete summary of the satellite tracking data actually being used for GRIM4 global gravity field modelling.

The tracking data are processed arc-by-arc with arc-lengths ranging from 2 days (e.g. TOPEX GPS satellite-to-satellite tracking) to 30 days (e.g. LAGEOS) depending on data type, satellites shape, altitude and principal resonance period. The resulting individual normal equation systems are, after being reduced for arc-dependent (state vector, etc.) and nuisance parameters, accumulated for each of the 34 satellites. When combining these normal equation systems to an overall system, relative weights in addition to the initial "realistic" weigths are introduced for an optimal solution. It turned out empirically that e.g. the optical data have to be overweighted for a better algebraic separation of the gravitational coefficients to be solved for and that especially the LAGEOS and SPOT-2 data have to be downweighted in order not to overload the whole system.

For a stable solution of the satellite-only normal equation system stochastic a-priori-information has to be introduced w.r.t. each individual harmonic gravitational coefficient. The (pseudo-) observation equation for a coefficient of degree l and order m with standard deviation σ_l following Kaula's degree variance model [*Kaula*, 1966] reads:

$$\begin{bmatrix} \overline{C}_{l,m} \\ \overline{S}_{l,m} \end{bmatrix} = 0 \quad , \ \sigma_l = 10^{-5}/l^2 \qquad\qquad 6.1$$

Table 6.1: GRIM-4 Tracking Data Summary (October 1995)

Satellite Name	I (deg.)	a (km)	e Ecc.	No. of Arcs x length(w)	O	L	M	A/X	Observ. Period (Y-1900)
PEOPLE	15.0	7006	.016	5	78	588	-	-	71
COURIER-1B	28.3	7469	.016	11	2844	-	-	-	66-67
VANGUARD-2	32.9	8298	.164	10	2082	-	-	-	66
EXPLORER-9	38.8	7960	.108	10	3568	-	-	-	62
D1-D	39.5	7622	.085	11	5832	1983	-	-	67/71
D1-C	40.0	7341	.053	13	2364	3773	-	-	67/71
BEACON-C	41.2	7507	.026	20	-	35999	-	-	79/83
TELSTAR-1	44.8	9669	.243	12x2	3828	-	-	-	62-64
ECHO-1RB	47.2	7966	.012	6x3	1804	-	-	-	65
STARLETTE	49.8	7331	.020	122	-	58521	-	-	83-84,86-88
AJISAI	50.0	7869	.001	70	-	42716	-	-	86-88
ANNA-1B	50.1	7501	.008	16	3194	-	-	-	66
GFZ-1	51.6	6968	.001	8	-	5086	-	-	95
LAGEOS-2	52.0	12278	.078	8	-	30908	-	-	92/93
GEOS-1	59.4	8075	.072	39	-	41910	-	-	77-78
ETALON-1	65.0	26400	.001	16x4	-	5032	-	-	89/90
ETALON-2	65.0	26400	.001	3x4	-	1975	-	-	90
TOPEX	66.0	7714	.001	7	-	7213	143585	-	92
				6	-	10417	178615	8278	93
TOPEX-(GPS)				1x1day	-	-	2x5955	-	92
				5x2 days	-	-	2x73983	-	93
GEOS-3	114.9	7226	.001	25	-	17698	-	-	75-77
GEOS-3-(ATS-6)				-	-	-	36730	-	75-78
TRANSIT-4A	66.8	7300	.008	8	512	-	-	-	62
AGENA	69.9	7295	.001	3x2	472	-	-	-	64
LAGEOS-1	109.8	12273	.004	52x4	-	292414	-	-	83-87
GEOSAT	108.0	7163	.001	20x.5	-	-	443426	-	86/87
				3	-	-	37336	-	86
GEOS-2	105.8	7711	.033	54	-	37265	-	-	75-77
EXPLORER-19	78.7	7800	.100	27	3280	-	-	-	65
BEACON-B	79.7	7354	.014	21	1542	1157	-	-	64-71
STELLA	98.7	7178	.001	15	-	4280	-	-	93
ERS-1	98.5	7153	.001	21	-	16468	-	-	92
				56	-	57680	-	37936	93/94
ERS-1/TOPEX				6	-	2462	-	12032	93
SPOT-2	98.2	7210	.001	23x.5	-	-	249392	-	91
METEOR3	82.6	7573	.002	12	-	20335	-	-	94
MIDAS-4	95.8	9995	.011	48x2	46814	-	-	-	64-65
OGO-2	87.4	7341	.075	11	774	-	-	-	66
OSCAR-19	90.2	7460	.018	18	-	-	125241	-	84
NOVA-1	90.0	7557	.001	16	-	-	123596	-	84
NOVA-3	90.0	7571	.003	55	-	-	439266	-	87
n_{sat}= 35				893	78,988	695,880	1,937,063	25,670	
						2,770,177			

I - inclination, a - semi-major axis, Ecc. - eccentricity, w - week
O - optical, L - laser, M - microwave (Tranet-, Doris-Doppler, GPS), A/X - altimeter crossover

68

These equations eventually have to be overweighted by 100 ($p = 100\ \sigma_1^{-2}$) when added to the overall system to be inverted for the solution.

To evaluate the effect of GFZ-1 laser data in combination with the existing satellite tracking data for global gravity field modelling, eight GFZ-1 laser arcs have been processed with a total of 5086 data points (mainly 5s normal points) from 262 passes observed by 13 laser ranging stations. The arc-lengths vary between three and six days according to the temporal data distribution. Only sparse observations were obtained during the month of May 1995.

Table 6.2 GFZ Tracking Data Statistics for the PGM061 Model

Arc	Epoch 1995	Length [d]	Normal Points (5s)	Passes	Stations
1	19 April	6	757	38	10
2	6 June	6	594	32	6
3	12 June	6	887	43	11
4	18 June	6	796	44	11
5	26 June	5	778	36	9
6	7 July	7	446	32	9
7	20 July	3	379	19	6
8	25 July	3	449	18	7
Σ		42	5086	262	

Table 6.2 gives the statistics of the 8 GFZ-1 arcs processed for a first tentative solution. Partial derivatives were generated for the following unknowns within the orbit integration computation to form the single arc normal equation systems:

- **global unknowns**
    - static gravitational potential: spherical harmonic coefficients $\overline{C}_{l,m}$, $\overline{S}_{l,m}$ complete to degree and order 70 (5036 unknowns, including $C_{o,o}$ and excluding degree 1 terms and $\overline{C}_{2,1}$, $\overline{S}_{2,1}$),
    - dynamic gravitational potential: secular rate in $\overline{C}_{2,0}$ and ocean tide potential coefficients $C_{s,l,m}^+$ and $S_{s,l,m}^+$ for 8 diurnal and semi-diurnal tides (77 unknowns),
    - geocentric tracking station coordinates (epoch values) plus horizontal rates of change to account for plate tectonic movements (5 unknowns per station)
- **arc-dependent unknowns**
    - GFZ-1's position and velocity at initial epoch (6 unknowns per arc),
    - surface force modelling: 1 scaling factor (c_r) per arc for solar radiation force, 1 to 4 scaling factors (c_d) per day for air drag depending on the actual data distribution along the arc; and amplitude and phase of a periodic along track acceleration to absorb an once per revolution disturbance.

69

The eight GFZ-1 single arc normal equation systems were reduced for the arc-dependent parameters, accumulated, weighted according to a standard deviation of $\sigma_i = 40$ cm, and finally combined with the PGM055 normal equation system containing the accumulated normals from all the other 34 satellites listed in Table 6.1. The stochastic a-priori-information was extended to cover all coefficients up to degree/order 70, as the PGM055 model is only complete up to degree/order 60 plus some terms up to maximum degree 69 within the zonals and ERS-1 resonant orders 13 and 57. The GFZ-1 data weighting was found iteratively to yield an optimum and stable solution. An initial higher weighting according to $\sigma_i = 12.5$ cm for the GFZ-1 laser normal points led to a singular normal equation system requiring an increased weighting of the stochastic a-priori-information for an inversion of the overall normal equation system.

6.2   PGM061 Model Evaluation: Gain of Information in the Spectral Domain of the Geopotential

For each pseudo-observation according to Eq. 6.1 the partial redundancy

$$f_i = 1 - q_a \ (100 \ \sigma_i^{-2}) \qquad\qquad 6.2$$

can easily be computed a posteriori with the diagonal terms q_{ii} of the cofactor matrix $Q_{\hat{p}}$ of the adjusted gravitational unknowns $p_1 = \{\overline{C}_{l,m}, \overline{S}_{l,m}\}$. The partial redundancy with

$$0 \le f_i \le 1 \qquad\qquad 6.3$$

is a measure for the degree of contribution of the stochastic a priori information to the determination of the associated solve-for parameter p_1 with respect to the contribution coming from the real observation data:

$f_i = 0$ p_1 estimated to 100 % from stochastic a priori information
        and to 0 % from real observations
$f_i = 1$ p_1 estimated to 0 % from stochastic a priori information
        and to 100 % from real satellite tracking observations

The value f_i therefore is a measure for the sensitivity of the totality of the analyzed satellite data to the disturbing gravitational potential. In case of $f_i = 0$ the associated unknown can be deleted from the system and in case $f_i = 1$ the additional stochastic a priori observation equation can be omitted without changing the adjustment results. The lower the value f_i the more the associated gravity coefficient is constrained to zero because of Eq. 6.1 [*Schwintzer*, 1990].

Figure 6.1 shows the partial redundancies f_i as resulting from the PGM061 solution with its typical pattern for a satellite-only solution: complete coverage of the very long-wavelength part of the gravitational spectrum and higher resolution only for certain bands of orders associated with (near-) resonant orbit perturbations of near-Earth satellites. Figure 6.2 depicts

70

the increase in the f_i values of the PGM061 solution w.r.t. to the PGM055 solution, i.e. the contribution coming from the first eight arcs of GFZ-1. The result clearly shows the increase in information for the terms around the orders 31 and 46 in accordance with the analytical perturbation computations (c.f. Figure 2.2.3); the first two orbit perturbation peaks in Figure 2.2.3 occuring at order 0 (zonal terms) and order 15 are visible but less pronounced in GFZ-1's real data sensitivity matrix. The reason is that the low order terms are already covered quite well for low and intermediate degrees also by the higher altitude satellites being in the solution.
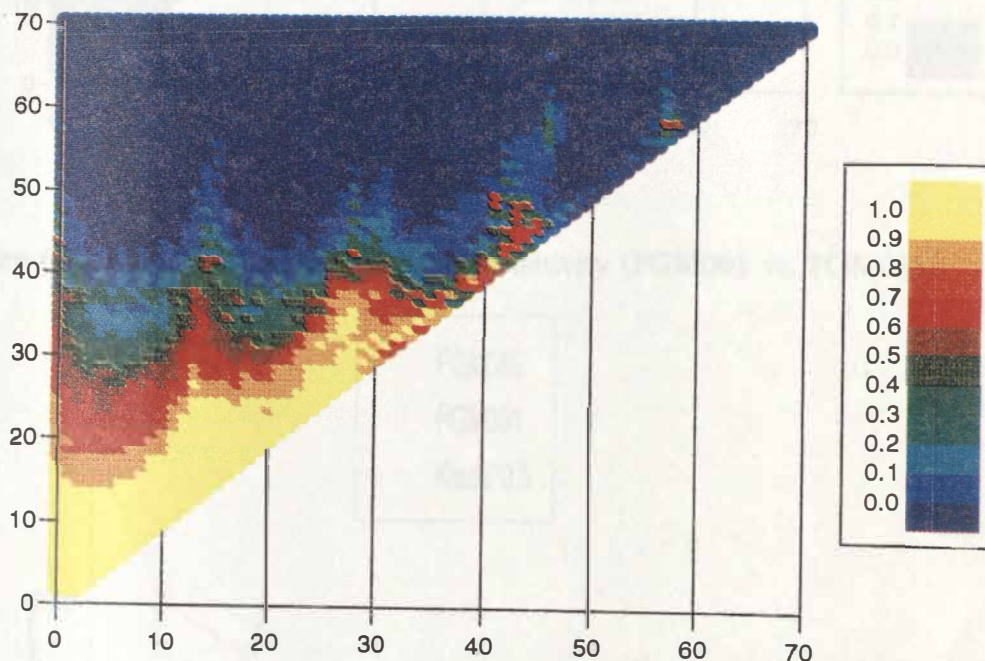

Figure 6.1: Sensitivity Matrix for the PGM061 Gravity Field Model Solution

71
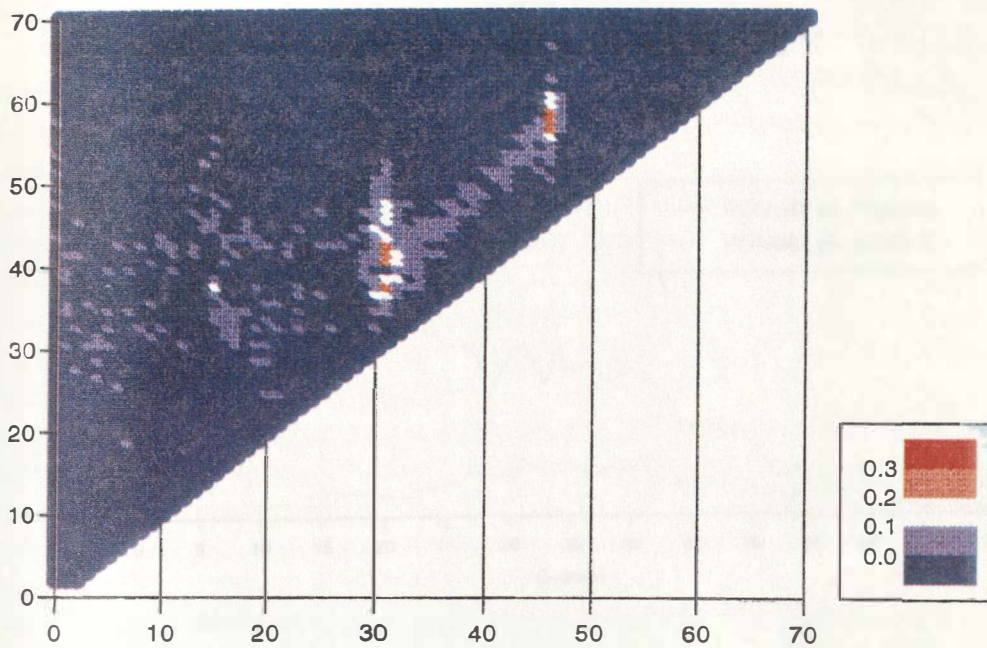
Figure 6.2: GFZ-1 Induced Increase in Sensitivity (PGM061 vs. PGM055)
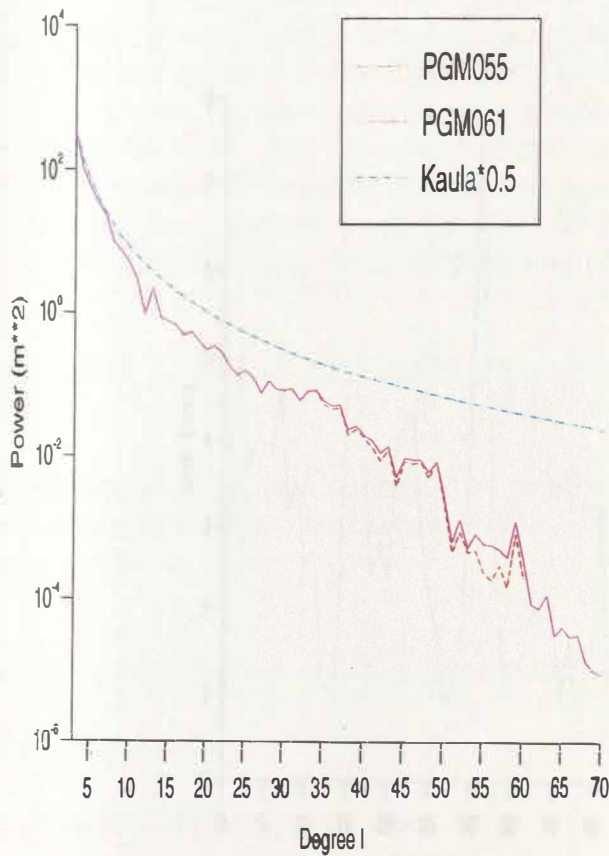
Figure 6.3: Geoid Signal Variances per Degree for PGM055 and PGM061 Gravity Field
Models, and Kaula's Degree Variance Model (scaled by 0.5)

72
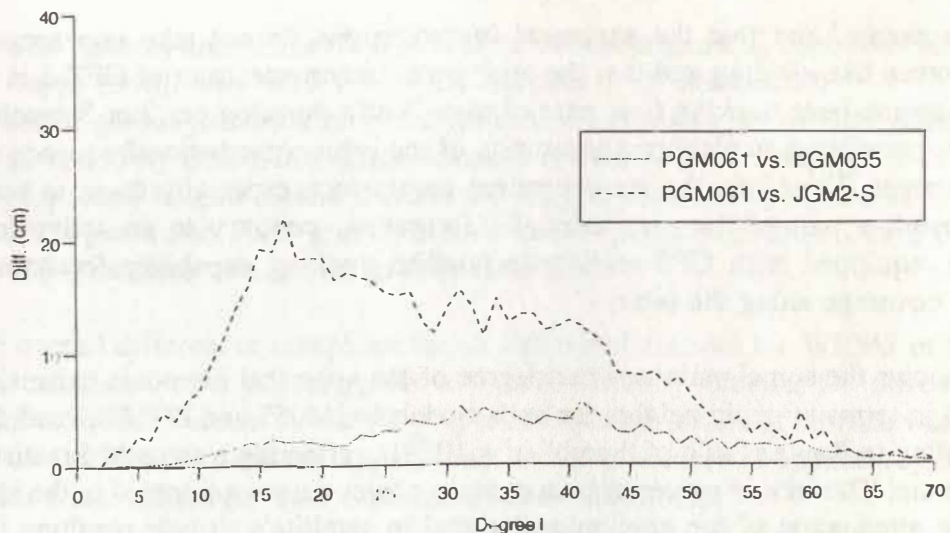
Figure 6.4: RSS of Gravitational Coefficient Differences per Degree in Terms of Geoid Heights for the PGM061 w.r.t. the PGM055 and JGM2-S Gravity Field Models, respectively.

Figure 6.5: RSS of Gravitational Coefficient Differences per Order in Terms of Geoid Heights for the PGM061 w.r.t. the PGM055 Gravity Field Model

73

It has to be pointed out that the analytical investigations do not take into account other disturbing forces like air drag and that the orbit perturbation spectrum of GFZ-1 is observed only by the sparse laser tracking (one pass of max. 5 min duration per 2 or 3 revolutions on average), not permitting an algebraic separation of the orbit perturbation frequency spectrum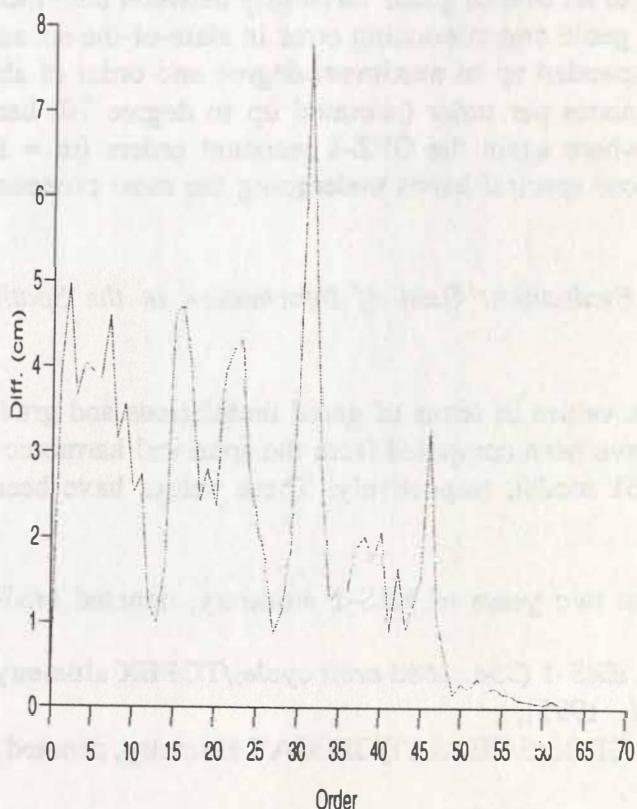 in the adjustment. Therefore, the arc-dependent parameters, especially those to account for air drag, absorb a part of the gravitational information, contrary to an active low-flying satellite e.g. equipped with GPS-satellite-to-satellite tracking capability for uninterrupted observation coverage along the orbit.

Figure 6.3 shows the signal variances per degree of the spherical harmonic expansion of the geopotential in terms of geoid heights for both models PGM055 and PGM061 and the power curve according to Kaula's "rule of thumb" $\sigma_l^2 = 10^{-10}/l^4$, reflecting a smoothed realistic geoid power spectrum. The lack of power of both model's power curves compared to the ideal curve is due to the attenuation of the gravitational signal in satellite's altitude resulting in a rapid decrease of the signal to noise ratio with increasing degree. As can be seen from Figure 6.3, adding the eight GFZ-1 normals to the overall satellite-only normal equation system increases the power content significantly from degree 30 onwards and particularly in between degree 53 and 58 due to the gain of information for the order 46 terms (c.f. Figure 6.2). Figure 6.4 shows the RSS of differences in the harmonic coefficients per degree in terms of geoid heights for the PGM061 model w.r.t. the PGM055 model, accumulating to an overall geoid variability of 21 cm, and w.r.t. the external American JGM2-S [*Nerem et. al.,* 1994] satellite-only model, accumulating to an overall geoid variability between both models of 89 cm. The latter value represents the geoid commissioning error in state-of-the-art satellite-only gravity field models which are expanded up to maximum degree and order of about 70. Figure 6.5 shows the difference variances per order (summed up to degree 70) between the models PGM055 and PGM061, where again the GFZ-1 resonant orders (m = 15, 31, 46) can be identified, lying within those spectral bands undergoing the most pronounced change.

6.3 *PGM061 Model Evaluation: Gain of Information in the Spatial Domain of the Geopotential*

Equal angular mean block values in terms of geoid undulations and gravity anomalies, and point geoid undulations have been computed from the spherical harmonic coefficients of the PGM055 and the PGM061 model, respectively. These values have been differenced with various data sets:

- 1° x1° geoid from two years of ERS-1 altimetry, denoted *MSS93* [*Gruber et al.,* 1993],
- 5°x5° geoid from ERS-1 (35d, 168d orbit cycle)/TOPEX altimetry, denoted *MSS95a* [*Anzenhofer et al.,* 1995],
- 5°x5° geoid from GEOS-3/SEASAT/GEOSAT altimetry, denoted *OSU92* [*Bašić and Rapp,* 1992],
- 5°x5° geoid from ERS-1/TOPEX/GEOSAT altimetry, denoted *OSU95* [*Rapp and Yi,* 1995],
- 5°x5° gravity anomalies from SEASAT altimetry, denoted *Marsh89* as provided by J. Marsh, NASA/Goddard Space Flight Center, in 1989,

74

- 5°x5° gravity anomalies from terrestrial free-air anomalies, denoted *OSU89* [*Kim and Rapp*, 1990], only values between latitudes ± 75° considered,
- set of globally distributed point geoid undulations (1261 values), denoted *DGL90*, compiled by GFZ from various sources and derived from doppler or GPS measured ellipsoidal heights minus orthometric heights observed by terrestrial levelling,
- 5°x5° geoid and 5°x5° gravity anomalies computed from the *JGM2-S* [*Nerem et al.*, 1994] satellite-only global gravity field model.

From the overall differences computed for an individual data set, the WRMS of the residuals has been calculated after adjusting for a constant bias to account for differences in the underlying reference system. A weight proportional to the cosine of latitude was adopted. In the case of the DGL90 data set, a statistical outlier procedure is applied rejecting all data points with a residual larger than twice its standard deviation.

Table 6.3 gives the results of the comparisons for the PGM055, PGM061 solutions and the American JGM2-S gravity field model. The fit to the 1°x1° geoid and to point undulations is worse than the fit to a 5°x5° geoid due to the truncation error inherent in a long-wavelength gravity field model.

75

Table 6.3: Intercomparisons with External Data Sets, WRMS (min ... max)
of Residuals After Bias Adjustment

Data Set	Data Type (unit)	Resolution	PGM055 JGM2-S	PGM061
Altimetry				
MSS93	N [m]	1°x1°	1.41(-17.1 ... 10.1) 1.39(-14.9 ... 9.9)	1.40(17.1 ... 9.8)
MSS95a	N [m]	5°x5°	0.76(-4.4 ... 3.2) 0.73(-5.7 ... 2.7)	0.75(-4.6 ... 3.1)
OSU92	N [m]	5°x5°	0.75(-4.6 ... 2.8) 0.72(-3.8 ... 2.5)	0.74(-4.6 ... 2.7)
OSU95	N [m]	5°x5°	0.79(-5.0 ... 3.0) 0.76(-6.3 ... 2.4)	0.78(-5.2 ... 2.9)
Marsh89*	Δg[mgal]	5°x5°	4.33(-22 ... 20) 4.27(-19 ... 20)	4.27(-21 ... 20)
Gravimetry				
OSU89*	Δg[mgal]	5°x5°	6.39(-27 ... 28) 6.54(-26 ... 30)	6.35(-27 ... 27)
Doppler/GPS-levelling				
DGL90*	N [m]	point values	1.56(n=943)	1.51(n=930)
Spher. harm. model				
JGM2-S	N [m]	5°x5°	0.61(-3.0 ... 4.1)	0.59(-3.0 ... 3.8)
	Δg[mgal]	5°x5°	2.30(-13 ... 13)	2.25(-13 ... 13)
PGM055	N [m]	5°x5°		0.12(-0.7 ... 0.6)
	Δg[mgal]	5°x5°		0.60(-3.8 ... 3.4)

*comparison up to l_{max} = 50 only, N - geoid undulation, Δg - gravity anomaly,
n: number of non-rejected points

76

Figure 6.6: 5°x5° Geoid Differences (Mean Block Values) Obtained from the PGM055 Induced Geoid Minus MSS95a Altimeter Geoid over the Oceans (Unit: Meter).
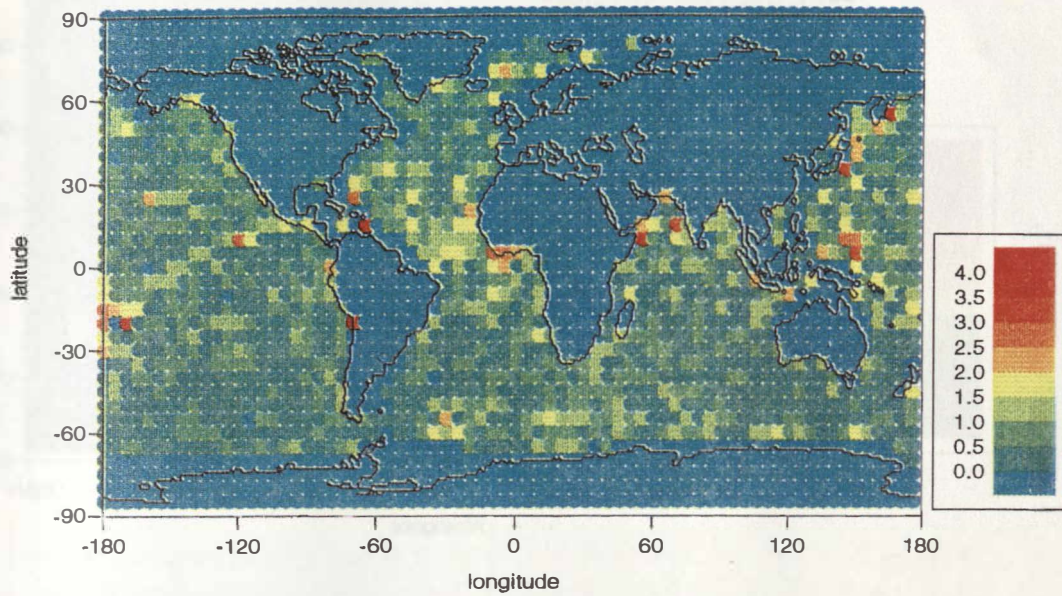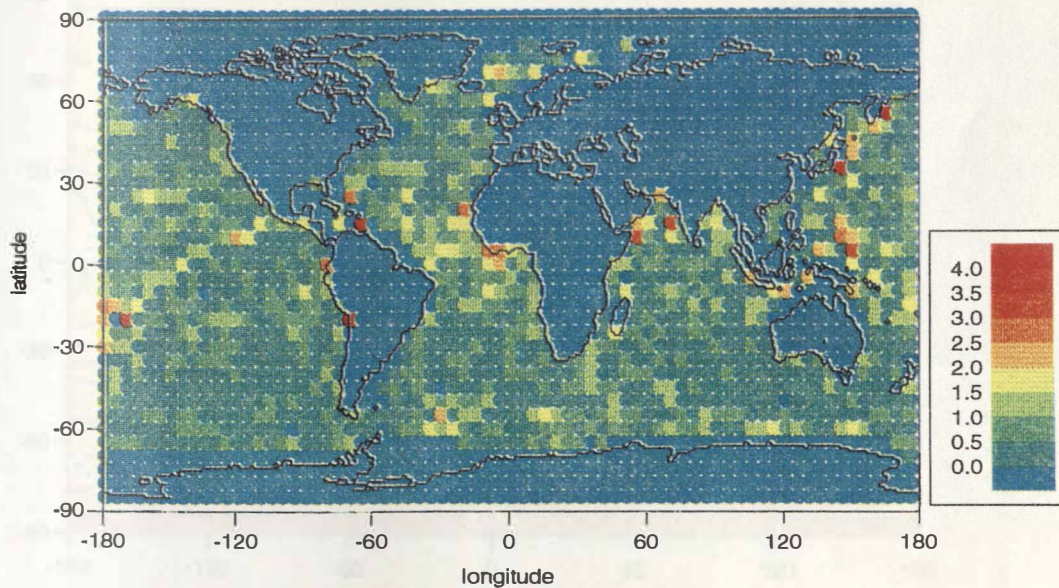

Figure 6.7: 5°x5° Geoid Differences (Mean Block Values) Obtained from the PGM061 Induced Geoid Minus MSS95a Altimeter Geoid over the Oceans (Unit: Meter).
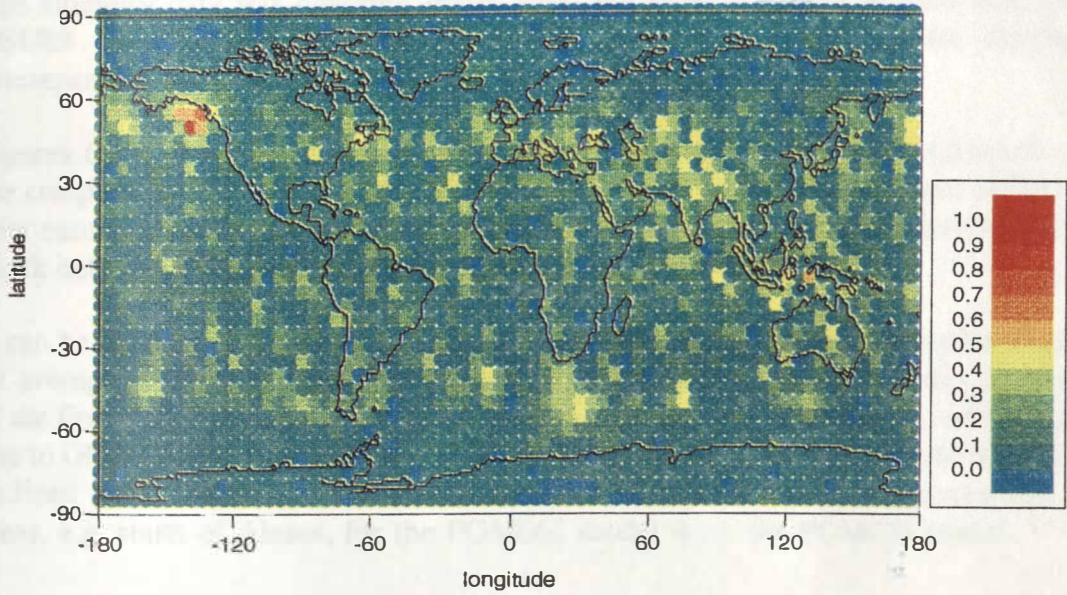
Figure 6.8: 5⁰x5⁰ Geoid Differences (Mean Block Values) Obtained from the PGM061vs.
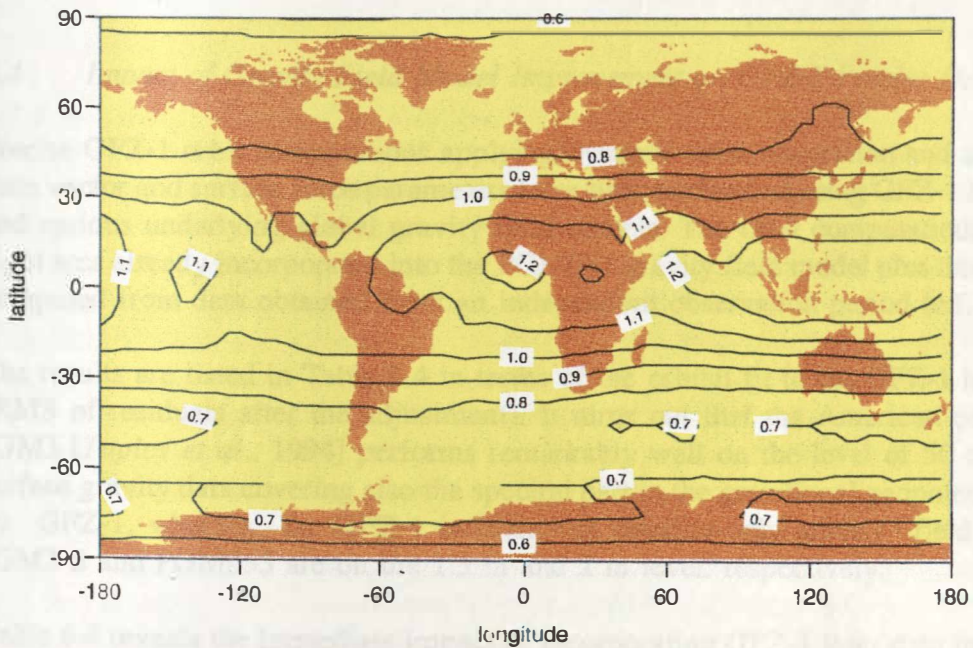PGM055 Induced Geoids (Unit: Meter, Contour Interval: 0,1m)

Figure 6.9: Standard Deviation of PGM061 Induced Geoid (Commissioning Error)

78

The altimetry data sets covering ocean areas are more homogeneous and accurate than the OSU89 data set derived from terrestrial gravimetry which reveals therefore larger discrepancies.

Figures 6.6 to 6.8 give the geographical distribution of the differences (absolute values) for the comparisons PGM055 and PGM061, respectively, vs. the oceanic geoid MSS95a (no data over continents and close to the poles), and undulation differences (absolute values) per 5°x5° block between PGM055 and PGM061.

It can be deduced from Table 6.3, that a 1 cm and 0.5 mgal improvement has been achieved on average in the global geoid and gravity field representation, respectively, by the inclusion of the first eight laser arcs of GFZ-1. Figure 6.8 clearly shows that geoid recovery differences due to GFZ-1 data nearly exclusively occur within the latitude band covered by GFZ-1's 51.6° inclined orbit. The inspection of Tables 6.6 to 6.8 reveals slight improvements in certain areas, e.g. south of Alasca, for the PGM061 model w.r.t. the PGM055 model.

For the sake of completeness, the geoid standard deviations, as computed by a rigorous error propagation from the PGM061 coefficients' variance-covariance-matrix, and a posteriori scaled by an empirically found factor of $c = 5$, are plotted in Figure 6.9 resulting in an overall mean geoid commissioning error of 1.0 m for the full degree/order 70 spherical harmonic expansion of the PGM061 model. No significant changes in the error propagation results can be stated w.r.t. the PGM055 model. This applies also if the error propagation is performed for the terms only up to degree and order 10 ($\sigma_{geoid} = 8.5$ cm) and 25 ($\sigma_{geoid} = 23.5$ cm), the very long wavelength geoid features.

6.4   Impact of Gravity Field Model Improvement on GFZ-1 Precise Orbit Restitution

Precise GFZ-1 orbit computations applying dynamic orbit integration and adjustment for the state vector and surface force parameters have been performed using GFZ-1 laser observations and various underlying global gravity field models. The orbit computations extend over the eight arcs already incorporated into the PGM061 gravity field model plus three additional arcs computed from data obtained from an independent observation period (c.f. Chapter 5).

The results are listed in Table 6.4 in terms of the orbital fit to the GFZ-1 laser observations (RMS of residuals after the adjustment). It turns out that the American combined solution JGM3 [*Tapley et al.,* 1994] performs remarkably well on the level of 50 cm, thanks to the surface gravity data covering also the spectral part in the gravitional geopotential being sensed by GFZ-1, whereas the GFZ-1 independent satellite-only gravity field model solutions JGM2-S and PGM055 are on the 1.5 m and 2 m level, respectively.

Table 6.4 reveals the immediate impact of incorporating GFZ-1 laser data in the gravity field normal equation system, especially improving the recovery of those spectral parts of the geopotential causing resonant (large) perturbations in GFZ-1's orbit (c.f. Figure 6.2). For the PGM061 model the orbital fit for the first eight arcs improves on average from over 2 m to below 30 cm, which partly is also due to aliasing effects of surface force modelling errors being absorbed by the gravity field solution. But this model then is capable to allow a GFZ-1 orbit restitution for arcs outside this particular observation period with a precision of about

79

1m which is a more than 50 % improvement w.r.t. to the GFZ-1 independent PGM055 gravity field model.

Test arc computations performed for other higher altitude satellites like ERS-1, LAGEOS and STARLETTE do not reveal any significant changes in the resulting orbital fits except for STARLETTE with a slight improvement of 2 mm (8.9 cm with PGM055 vs. 8.7 cm with PGM061).

Table 6.4: GFZ-1 Test Arc Computations Based upon Gravity Field Models with
and without GFZ-1 Laser Data, Resp.
(RMS of Laser Range Residuals after Orbit Adjustment)

orbital fit	PGM055	PGM061 (=PGM055 + GFZ-1 arcs 1-8)	JGM2-S	JGM3
arcs 1-8	205 cm	28 cm	142 cm	48 cm
arcs 9-11	264 cm	93 cm	164 cm	60 cm
arcs 1-11	223 cm		148 cm	51 cm

arc lengths: 3 to 7d,
adjusted parameters: state vector, 1 c_r, 1 to 4 c_d per day, ¹/rev along track

6.5 Conclusion

The exploitation of 42 days of GFZ-1 laser data with all together about 5000 data points has resulted in the new satellite-only gravity field model PGM061 based upon the PGM055 solution deduced from 2.8 Mio. tracking observations obtained on 34 other satellites. The spherical harmonic expansion of the PGM061 gravitational model is complete up to degree and order 70.

In spite of the relatively small number of observations, the gain in information, especially around the GFZ-1 resonant orders 15, 31 and 46 within the gravitational spectrum is quite remarkable and leads to a GFZ-1 orbit restitution precision improvement from initially about 2 m to 1 m. The GFZ-1 contribution to a global 5°x5° geoid and gravity field representation is moderate but visible with an 1 cm and 0.05 mgal consistent improvement on a level of 75 cm and 5 mgal, respectively. Due to the sparse laser tracking, up to now no significant improvement in the modelling of the very long-wavelength features of the geoid, being important for oceanographic applications, can be recognized. Data covering the whole 3 to 5 years mission duration of GFZ-1 must be accumulated and evaluated to enlarge the effect of GFZ-1 laser data on global gravity field recovery.

7. SUMMARY AND CONCLUSIONS

The scientific objective of the GFZ-1 mission is to improve the accuracy and the resolution of Earth's gravity field models. GFZ-1 will be sensitive to the gravitational geopotential up to degree 100 at interesting orders of 31, 46, 62, 77, and at sidebands thereof. During the mission the altitude will decrease and solar activity will increase. Both effects multiply the drag forces exerted on GFZ-1. Therefore POD in view of separating the gravity signal from the drag signal will become more difficult.

GFZ-1 was launched from space station MIR on April 19, 1995 at an initial altitude of appr. 400 km into a near circular, 51.6° inclination orbit. GFZ-1 is designed as Lageos and other geodetic satellites. The massive spherical body covered with laser retro reflectors features an optimum area-to-mass ratio minimizing drag perturbations. Depending on solar activity, the lifetime estimates vary between 3.5 and 5 years.

60 special cube corners were selected showing a two-spot far field reflection pattern. The reflector array is formed by 20 triads of reflectors arranged so that a mean velocity aberration is accounted for at random orientation of the satellite. The CoM was estimated by 3 independent methods and institutions, the results agree within 2 mm. This precision is better than required in view of recent orbital model errors.

The low altitude of GFZ-1 introduced a new class of requirements into SLR station hardware: at high elevations the angular velocity may exceed the limits of the mount and the small signal time of flight may exceed the limits of the transmit-receive switch. The design of the satellite enables daylight tracking at multi-photon level using wide beams in case of degraded orbit predictions.

A minimum number of meetings took place between GFZ and the main contractor, the KT company in Munich, and the Russian sub-contractors in the design, construction and test phase of the mission. The bulk of information flow went through phone and fax. A quite early trade-off was made using the launch opportunity via space station MIR. A trade-off had also to be made in deploying GFZ-1 with no dedicated rotation in space. In preparation of the mission major concern was given to the enhancement of SLR acquisition tools and to radar tracking backup.

Before launch tracking requests were sent out to the SLR network. At a number of scientific meetings the mission was promoted. The general response from the SLR stations was positive despite of the expected acquisition problematics.

A training campaign with space station MIR as optical target in the months before launch produced experience at the stations for low altitude target tracking and at GFZ/D-PAF for radar tracking element conversion. The campaign provided also an opportunity to introduce the drag function which had to be developed as a new tool in SLR aquisition to handle residual drag perturbations in station orbit integrations. The transformation of radar tracking based twoline orbital elements provided by USSpaceCom has to account for reference frame and orbit perturbation model differences w.r.t. SLR orbit prediction elements. An iterative least squares procedure was implemented to overcome incompatibilities.

81

The cargo spacecraft PROGRESS M-27 being launched on April 9, 1995, carried GFZ-1 to space station MIR where it arrived on April 11. For the controlled orbit injection of GFZ-1 from the MIR airlock a simple and robust separation mechanism was constructed. The date of the separation was optimized w.r.t. the acquisition conditions for the SLR network under the restrictions of the MIR mission. GFZ-1 was separated from MIR on April 19, 1995 at 19:12 UT shortly before crossing the west coast of South America. At that time the MIR crew had good visibility conditions to track GFZ-1 by the onboard laser distance meter and to record the separation with the video camera which was live transmitted to the control center in Oberpfaffenhofen, Germany.

Due to bad weather over Europe the SLR stations there were not able to get laser returns from GFZ-1 during its first revolutions. The first confirmed returns were acquired by the NASA station Greenbelt on April 20, 1995 at 00:21 UT.

Orbit predictions for GFZ-1 are generated mainly from laser tracking data analyses and supplied in appropriate forms to the SLR network. The orbit prediction products consist of the tuned IRVs, the drag functions, the time bias functions, the SAO-elements and the GFZ/D-PAF twoline elements. A mail tool has been installed at EDC that serves for the quick exchange of time bias values observed at the stations.

Besides the orbit predictions a weekly report named "GFZ-1 Post" is distributed to the SLR community. It contains the SLR tracking status and the orbit prediction generation status as well as other GFZ-1 related topics depending on necessity.

GFZ-1 tracking becomes particular difficult during daylight. There are monthly periods between day and nighttime tracking with opposite day/nighttime periods for the stations on the Northern and on the Southern hemisphere. As the bulk of the stations is located on the Northern hemisphere, the few Southern stations play an important role in keeping acquisition alive. Though the tracking record showed initially an unexpected success, tracking amount decreased to zero in the first Northern daylight phase. The following Northern daylight phases could well be covered by observations thanks to an increased number of stations participating including the Australians and thanks to improved acquisition procedures. Geographically a lack of data in the Southern Pacific and South Africa can be noted.

GFZ-1 orbit prediction accuracy heavily depends on the occurence of geomagnetic storms and on the accuracy of geomagnetic and solar activity predictions. A practical way to keep the time bias low are frequent orbit prediction updates.

In the POD process particular emphasis is put on the set-up of the empirical drag coefficients (c_d) intended to account for atmospheric model errors. It turns out that the c_d parameters also compensate for parts of the gravity field model errors. Gravity model errors are also causing saw-tooth effects in the c_d time series. The accuracy of the c_d estimates is depending on the data distribution in time. Estimates of empirical radiation coefficients (c_r) are drastically affected by the gravity model errors, but hardly influence the orbital fit.

The atmospheric models CIRA'86 and DTM model the density variations of the atmosphere in a similar way, but deviate in mean density at the height of GFZ-1 by about 25%. Both models can equally be used in the POD process if a proper parametrization can be based on

82

sufficiently dense data.

Combined gravity field models as f.i. the GRIM4-C4 model or the JGM3 model deliver orbital fits down to the half meter level, where the satellite-only models as f.i. the GRIM4-S4 model are good to only about 2 m for GFZ-1 POD.

GFZ-1 laser ranging data of 42 days comprising appr. 5000 data points were processed and incorporated into the latest GRIM4-S satellite-only model called PGM055 resulting in the new model PGM061. The gain in information within the gravitational spectrum around orders 15, 31 and 46 is quite noticeable. The orbital fit in POD improves from 2 m to better than 1 m. The contribution of GFZ-1 to a global 5° x 5° geoid representation improvement is moderate but visible. Up to now a significant improvement of the long-wavelength features of the geoid can not be recognized, but may be expected by accumulating the data of the whole GFZ-1 mission.

83

REFERENCES

Anzenhofer, M., Gruber, Th., and M. Rentsch: *Global High Resolution Mean Sea Surface Based on ERS-1 35- and 168- Day Cycles and Topex Data*. Proceedings IAG Symposium G3 of IUGG General Assembly, Boulder, submitted 1995

Arnold, D.A.: *Method of Calculating Retroreflector-Array Transfer Functions*. SAO Special Report 382, 1978

Barlier, F., Berger, C., Falin, K.L., Kockarts, G., and G. Thuillier: *A thermospheric Model based upon satellite drag data*. Annales Geophysicae 34, pp. 9-24, 1978

Bašic, T., and R.H. Rapp: *Oceanwide Prediction of Gravity Anamalies and Sea Surface Heights Using Geos-3, Seasat, and Geosat Altimeter Data and ETOPOSU Bathymetric Data*. Report No. 416, Deptartment of Geodetic Science and Surveying, Ohio State University, Columbus, Ohio, 1992

Bosworth, J., Degnan, J., Jessie, L., McGarry, J., Crooks, H., Murdoch, A., Wetzel, S., and J. Horvath: *Support of the GFZ-1 and ERS-2 Missions by the NASA SLR Stations and Network Operations Center*. Handouts, March 17-22, GFZ/D-PAF, Oberpfaffenhofen, Germany, 1995

Brouwer, D.: *Solution of the Problem of Artificial Satellite Theory without Drag*. Astronomical Journal 64, pp. 378-397, 1959

Chen, Z., and R. König: *Drag function for GFZ-1 IRVs*. In: Sinclair, A.T. (Ed.), Proceedings of Annual Eurolas Meeting, Munich, March 1995, pp. 85-88, Royal Greenwich Observatory, Cambridge, 1995

Egger, D.: *GFZ-1 Center of Mass - Korrektur bestimmt aus der Simulation von Laserentfernungsmessungen*. Report Munich, 1995

Gruber, Th., Anzenhofer, M., and M. Rentsch: *The 1995 GFZ High Resolution Gravity Model*. In: Proceedings of IAG Symposium Global Gravity Field and its Temporal Variation, Boulder, Colorado, Springer Verlag, 1996, in print

Gruber, Th., Massmann, F.-H., and Ch. Reigber (eds.): *ERS-1 D-PAF Global Products Manual*. GeoForschungsZentrum Potsdam, 1993

Hedin, A.E.: *A revised Termospheric Model Based on Mass Spectrometer and Incoherent Scatter Data: M.S.I.S.-83*. Journal of Geophysical Research 88, A12, pp. 10170-10188, 1983

Hoots, F.R., and R.L. Roehrich: *Models for Propagation of NORAD Element Sets*. Spacetrack Report No. 3, compiled by TS Kelso 1988, Defense Documentation Center, Alexandria VA, 1980

Jelalian, A.V.: *Laser radar systems*. Artech House, Boston/London, 1992

Jessie, L.S.: *NASA Satellite Laser Ranging Support Plan for the GFZ-1 Mission*. Doc.No. NSLR-03-0021, NASA, Goddard Space Flight Center, Greenbelt, Maryland, 1995

Kaula, W.M.: *Theory of Satellite Geodesy*. Blaisdell, Waltham, Massachusetts, 1966

Kim, J.-H., and R. H. Rapp: *The Development of the July 1989 1°x1° and 30' x 30' terrestrial mean free-air anomaly data base*. Report No. 403, Deptartment of Geodetic Science and Surveying, Ohio State University, Columbus, Ohio, 1990

König, R.: *Predictions for ERS-1*. In: Veillet, C. (Ed.), Proceedings of 7th International Workshop on Laser Ranging Instrumentation, pp. 385-392, Grasse, 1989

König, R.: *GFZ-1 Acquisition and Campaign*. Satellite Laser Ranging Newsletter, SLR Subcommission of the CSTG, June 1995, pp. 17-19, Goddard Space Flight Center, NASA, 1995

König, R., and Z. Chen: *Probable Qualities of GFZ-1 Orbit Predictions*. In: Proceedings of 9th International Workshop on Laser Ranging Instrumentation, Canberra 1994, in print

König, R., Li, H., Massmann, F.-H., Raimondo, J.C., Rajasenan, C., and Ch. Reigber: *On the Accuracy of ERS-1 Orbit Predictions*. In: Degnan, J.J. (Ed.), Proceedings of 8th International Workshop on Laser Ranging Instrumentation, pp. 9.1-9.8, NASA Conference Publication 3214, 1993

Nerem, R.S., Lerch, F.J., Marshall, J.A., Pavlis, E.C., Putney, B.H., Tapley, B.D., Eanes, R.J., Ries, J.C., Schutz, B.E., Shum, C.K., Watkins, M.M., Klosko, S.M., Chan, J.C., Luthcke, S.B., Patel, G.B., Pavlis, N.K., Williamson, R.G., Rapp, R.H., Biancale, R., and F. Nouel: *Gravity Model Development for TOPEX/POSEIDON: Joint Gravity Models 1 and 2*. Journal of Geophysical Research 99, C12, 24421-24447, 1994

Neubert, R.: *An Analytical Model of Satellite Signature Effects*. In: Proceedings of 9th International Workshop on Laser Ranging Instrumentation, Canberra 1994, in print

Rapp, R.H., Wang, Y.M., and N.K. Pavlis: *The Ohio State 1991 Geopotential and Sea Surface Topography Harmonic Coefficient Models*. Report No. 410, Department of Geodetic Science and Surveying, Ohio State University, Columbus, Ohio, 1991

Rapp, R.H., and Y.Yi: *The OSU MSS 1995*. Personal communication and Poster paper at the SWT meeting, JPL, May 1995

Reigber, Ch., Kaniuth, K., Cuno, J., Müller, H.,Wakker, K.-F., Aardoom, L., Nouel, F., Barlier, F., Paquet, P., and Ph. Hartl: *POPSAT System Study - Final Report*. ESA Contr. No 4 591/80/F/DD/SC, Munich, 1982

Reigber, Ch., and R. König: *Gravity and Atmosphere Aspects by the Low Altitude Target GFZ-1*. In: Proceedings of 9th International Workshop on Laser Ranging Instrumentation, Canberra 1994, in print

Reigber, Ch., and R. König: *The GFZ-1 mission status*. In: Sinclair, A.T. (Ed.), Proceedings of Annual Eurolas Meeting, Munich, March 1995, pp. 89-90, Royal Greenwich Observatory, Cambridge, 1995a

Reigber, Ch., and R. König: *The Gravity Regimes Sensed by GFZ-1*. Annales Geophysicae 13 (Suppl. I), Abstracts EGS XX Gen. Ass. Hamburg, C154, 1995b

Reigber, Ch., König, R., and F.-H. Massmann: *The GFZ-1, the ERS-2 and the ERS-1/2 Tandem Mission*. In: Proceedings of 9th International Workshop on Laser Ranging Instrumentation, Canberra 1994, in print

Schulte, W., Wulf, E., Lemke, N., Reigber, Ch., and R. König: *GFZ-1: A Geodetic Microsatellite Launched from Space Station MIR*. In: Proceedings AIAA/USU Conference on Small Satellites, Logan, Utah, September 1995, submitted

Schwintzer, P.: *Sensitivity Analysis in Least Squares Gravity Field Modelling by Means of Redundancy Decomposition of Stochastic A Priori Information*. Internal Report PS/51/90, Deutsches Geodätisches Forschungsinstitut, Abt. 1 (DGFI), München, 1990

Schwintzer, P., Reigber, Ch., Barth, W., Massmann, F.-H., Raimondo, J.C., Gerstl, M., Bode, A., Li, H., Biancale, R., Balmino, G., Moynot, B., Lemoine, J.M., Marty, J.C., Barlier, F., and Y. Boudon: *GRIM4 - Globale Schwerefeldmodelle*. Zeitschrift für Vermessungswesen 117, 227-247, 1992

Schwintzer, P., Reigber, Ch., Bode, A., Kang, Z., Zhu, S.Y., Massmann, F.-H., Raimondo, J.C., Biancale, R., Balmino, G., Lemoine, J.M., Moynot, B., Marty, J.C., Barlier, F., and Y. Boudon: *Long-Wavelength Global Gravity Field Models, GRIM4-S4, GRIM4-C4*. Journal of Geodesy, in preparation 1995

Schwintzer, P., Reigber, Ch., Massmann, F.-H., Barth, W., Raimondo, J.C., Gerstl, M., Li,H., Biancale, R., Balmino, G., Moynot, B., Lemoine, J.M., Marty, J.C., Boudon, Y., and F. Barlier: *A New Earth Gravity Model in Support of ERS-1 and SPOT-2, GRIM4-S1/C1*. Final Report to the German Space Agency (DARA) and the French Space Agency (CNES), DGFI/GRGS, München/Toulouse, 1991

Shargorodsky, V.: *GFZ-1, Scientific-Technical Note for the User*. Moscow, 1995a

Shargorodsky, V.D.: *Experimental testing of level of a signal reflected from the device GFZ-1 in the conditions of space flight*. Technical note, Moscow, 1995b

Tapley, B.D., Watkins, M.M., Ries, J.C., Davis, G.W., Eanes, R.J., Poole, S.R., Rim, H.J., Schutz, B.E., Shum, C.K., Nerem, R.S., Lerch, F.J., Pavlis, E.C., Klosko, S.M., Pavlis, N.K., and R.G. Williamson: *The JGM-3 Gravity Model*. Annales

Geophysicae, Part 1 Solid Earth Geophysics & Natural Hazards, Supplement to Volumne 12 (Abstracts of XIX. Gen. Assembly of EGS in Grenoble, April 1994), C 192, 1994

Zhu, S.Y., and Ch. Reigber: *The German PAF for ERS-1 - ERS-1 Standards Used at D-PAF.* Doc.No. ERS-D-STD-31101, Deutsches Geodätisches Forschungsinstitut, Abt. 1 (DGFI), München, 1991

Appendix A.1: Format and Description of IRVs

Form:

```
DSIDP GFZ1.ORB.PRD   IRVS              C 950725
GFZ_FITXYZ_950221_IRVS
  1995  7 25  0  0  0.0    -5918942.859520     156387.662942    3262286.104422
  8001    26     1        -2759.442781345   -4939.288345272   -4743.497714168
     286    293      0           10634.0    -2500269.092155  -12442.228840785
GFZ_FITXYZ_950221_IRVS
  1995  7 26  0  0  0.0     6375147.498178    2255520.910332     170782.574013
  8001    26     2        -1579.561218004    3972.570673638    6021.361704955
     285    290      0           10632.0     8801450.982523    8414.371160589
GFZ_FITXYZ_950221_IRVS
  1995  7 27  0  0  0.0    -4287098.132589   -3834997.775226   -3576360.605934
  8001    26     3         5511.789147892   -2022.822116091   -4449.181144435
     284    286      0           10629.0   -11698456.513750    -960.214112634
GFZ_FITXYZ_950221_IRVS
  1995  7 28  0  0  0.0      430748.002799    4228482.801600    5248295.659864
  8001    26     4        -7333.583632869    -243.168953934     796.048246372
     284    283      0           10628.0     9907526.464263   -6780.704340431
GFZ_FITXYZ_950221_IRVS
  1995  7 29  0  0  0.0     3659607.856523   -3526573.177959   -4477772.802238
  8001    26     5         6190.459989980    2324.728021569    3235.918132446
     283    279      0           10625.0    -4344738.123673   11751.106143994
GFZ_FITXYZ_950221_IRVS
  1995  7 30  0  0  0.0    -6314591.525447    1863223.315513    1546698.122790
  8001    26     6        -2560.071538985   -3846.909122247   -5760.745296580
     282    276      0           10623.0    -2904670.087144  -12167.725957812
GFZ_CONDOI_921001_IRVS
  1995  7 31  0  0  0.0     6429095.502195     336546.417711    2067491.216000
  8001    26     7        -2029.059032990    4435.695466763    5545.352720000
     282    272      0           10621.0     8833133.135906    7951.989153773
```

Explanations:

1. Record (data set identification): DSIDP is the data set ID parameter. The "C" is a quality flag (A = good, B = not so good, C = poor, X = unknown) where the application of the drag function is considered. "950725" is the date of determination and dissemination of the data set.

2. Record (state vector header): Identifier of the IRV generation program.

3. Record (epoch and position record): The epoch is given in ordinary date i.e. year, month, day, hour, minute, and second, and in the UTC time scale. The position at the epoch is given in X, Y and Z pseudo body-fixed coordinates (unit: meter).

4. Record (velocity record): The first three parameters are satellite ID, ephemeris number, and the IRV sequence number. The 4th - 6th parameters are the velocity components in X, Y, Z direction (unit: m/s).

5. Record (information and checksum record): The first two parameters are X-, Y- component of polar motion (unit: mas). The third parameter is the change in Earth rotation rate (unit: 10^{-14} rad/s). The 4th - 6th parameters are the check-sum of all values excluding position and velocity, the check-sum of all position components, and the check-sum of all velocity components.

6.- 9. Record: Next IRV

88

Appendix A.2: Format and Description of the Drag Function

Form:

```
DSIDP GFZ1.ORB.PRD   DRAG FUNCTION    A 950725
IRV SET 950725   EPHEM NO 26   SATELLITE 8001  MAXEPOCH 1
EPOCH -1621.5 DRAG FRCO 0.0 13.3 0.4 NMAX  6
```

Explanations:

1. Record (data set identification): DSIDP is the data set ID parameter. The "A" is a quality flag (A=good, B=not so good, C=poor, X=unknown). "950725" is the date of determination and dissemination of the data set.

2. Record (relations and expansion): IRV set "950725" was disseminated at that date; can be found in the DSIDP record of the IRV set. The ephemeris number can be found in line 3 of each individual IRV. "8001" is the satellit ID in the IRVs. MAXEPOCH is the number of EPOCH records following. Usually MAXEPOCH will be 1. It might be necessary to increase it in periods of high solar and geomagnetic activity.

3. (+MAXEPOCH-1). Record (Fourier function parameters): The EPOCH of the drag function is given in JD2000 days and in the UTC time scale. The coefficients following DRAG FRCO are the coefficients a, b and c of the drag function as explained below. NMAX is the degree of the Fourier expansion recommended.

The drag time bias (TB) is given by the Fourier function

$$\text{drag } TB = a + b*[-\cos x + \cos(2x)/4 - \cos(3x)/9 \ldots$$
$$+- \cos(NMAX*x)/(NMAX*NMAX)]$$
$$+ c*[-\sin x + \sin(2x)/2 - \sin(3x)/3 \ldots$$
$$+- \sin(NMAX*x)/NMAX]$$

where
$$x = 2*pi*(t-0.5)$$

with drag TB in ms and t in days since epoch.

In the above example the coefficients are a=0.0, b=13.3, c=0.4. The drag TB for July 26th, 1995, reads f.i.:

```
at  0:00 UTC = -1620.50  JD2000 = 49924 MJD: drag TB =  20 ms
at  6:00 UTC = -1620.25  JD2000              : drag TB =  -3 ms
at 12:00 UTC = -1620.00  JD2000              : drag TB = -11 ms
at 18:00 UTC = -1619.75  JD2000              : drag TB =  -3 ms
at 24:00 UTC = -1619.50  JD2000              : drag TB =  20 ms
```

89

Appendix A.3.: Format and Description of the Time Bias Function

Form:

```
DSIDP GFZ1.ORB.PRD   TIME BIAS          B 950726.2
IRV SET 950725    EPHEM NO 26   SATELLITE 8001
EPOCH -1621.5 TB COEFF -8.34 26.74 0.000 0.000
```

Explanations:

1. Record (data set identification): DSIDP is the data set ID parameter. The "B" is a quality flag (A=good, B=not so good, C=poor, X=unknown). "950726" is the date of determination and dissemination of the data set. ".2" is the number of the released TB function at the dissemination day. If the release number is "1" then ".1" is omitted.

2. Record (relations): IRV set "950725" was disseminated at that date; can be found in the DSIDP record of the IRV set. The ephemeris number can be found in line 3 of each individual IRV. "8001" is the satellit ID in the IRVs.

3. Record (function parameters): The EPOCH of the TB function is given in JD2000 days and in the UTC time scale. The coefficients following TB COEFF are the coefficients a, b, c, and d of the TB function as explained below.

The time bias (TB) is given by the polynomial function

$$TB = a + b*t + c*t^2 + d*t^3$$

with TB in ms and t in days since epoch.

In the above example the coefficients are a=-8.34, b=26.74, c=0.000, d=0.000. For July 27th, 1995, 0:00 UTC = -1619.5 JD2000 = 49925 MJD, the TB reads f.i.:

$$TB = -8.34 + 26.74*(-1619.5-(-1621.5)) = 45.14 \text{ ms}$$

90

Appendix A.4: Format and Description of the SAO Elements

Form:

```
DSIDP GFZ1.ORB.PRD    SAO_ELEMENTS        C 950725
GFZ_FITSAO_950510
(ORBMESS)
XYEL    1 SATELLITE 8601795
GTHF    2 EPOCH 49923 0.
YINY    3 POLY 2 4 6 8 12
BXHQ    4 ELEMENTS
XEJB    5  66.7833502867 3.7937309033
YDUY    6  326.5845999680 -5.0289697424
MYQX    7  51.6483533523 -0.0000886341
RWLQ    8  0.0004543571 -0.0000023015
NCXD    9  0.2085441129 15.6010222265 0.2271E-04 0.5175E-08
KBQK   10 LP 1
WEYS   11 LPTERMS
HBDG   12  0.0000000E+00 0.0000000E+00 0.0000000E+00
LFQK   13  0.0000000E+00 0.0000000E+00 0.0000000E+00
SWUO   14  0.0000000E+00 0.0000000E+00 0.0000000E+00
WAYZ   15  0.0000000E+00 0.0000000E+00 0.0000000E+00
AECD   16  0.0000000E+00 0.0000000E+00 0.0000000E+00
GQGX   17  0.1140000E-02
PQFU   18END
```

Explanations:

1. Record (data set identification): DSIDP is the data set ID parameter. The "C" is a quality flag (A = good, B = not so good, C = poor, X = unknown). "950725" is the date of determination and dissemination of the data set.

2. Record (state vector header): Identifier of the SAO elements generation program.

3. Record (SAO format parameter set start of information): String (ORBMESS).

4. Record (satellite identification): consists of four parameters: checkword, line sequence number, the string 'SATELLITE', satellite ID.

5. Record (epoch): consists of five parameters: checkword, line sequence number, the string 'EPOCH', epoch in modified Julian days, and the fractional part of the epoch in the UTC time scale.

6. Record (polynominal expansion information): consists of eight parameters: checkword, line sequence number, the string 'POLY', sum of coefficients for expansion of ω, ditto plus Ω, ditto plus i, ditto plus e, and ditto plus $M, n, \dot{n}, \ddot{n}$.

7. Record (coefficients start of information): consists of three parameters: checkword, line sequence number and the string 'ELEMENTS'.

8. - 12. Record (coefficients for polynominal expansion): each record consists of 2 to 4 parameters:

record-no.	col. 1	col. 2	col. 3	col. 4	col. 5	col. 6
8	checkword	line seq. no.	ω_0 [deg]	ω_1 [deg/d]	--	--
9	"	"	Ω_0 [deg]	Ω_1 [deg/d]	--	--
10	"	"	i_0 [deg]	i_1 [deg/d]	--	--
11	"	"	e_0	e_1 [1/d]	--	--
12	"	"	M_0 [rev]	n [rev/d]	$\dot{n}$ [rev/d^2]	$\ddot{n}$ [rev/d^3]

where index 0 represents constant terms and index 1 secular rates of change.

13. Record (long period terms information): consists of four parameters: checkword, line sequence number, the string 'LP' and the indicator 1 if long period terms follow or 2 if not.

14. Record (long period terms start of information): consists of three parameters: checkword , line sequence number and the string 'LPTERMS'.

15.-20. Record (coefficients of long period terms): each record consists of 1 to 3 parameters:

record-no.	col. 1	col. 2	col. 3	col. 4	col. 5
15	checkword	line seq. no.	$B_{1,1}$	$B_{1,2}$	$B_{1,3}$
16	"	"	$B_{2,1}$ [deg]	$B_{2,2}$ [deg]	$B_{2,3}$ [deg]
17	"	"	$B_{3,1}$ [deg]	$B_{3,2}$ [deg]	$B_{3,3}$ [deg]
18	"	"	$B_{4,1}$	$B_{4,2}$	$B_{4,3}$
19	"	"	$B_{5,1}$ [rad]	$B_{5,2}$ [rad]	$B_{5,3}$ [rad]
20	"	"	$\Delta \eta_0$	--	--

21. Record (data set end): consists of three parameters: checkword, line sequence number and the string 'END'.

Appendix A.5: Format and Description of D-PAF Twoline Elements

Form:

```
DSIDP GFZ1.ORB.PRD    TWO_LINE_ELEMENTS B 950725
GFZ_POLSBR_950510
1 23558U 86 17 JE 95206.00000000 0.00000739  00000-0  00000-0 0    10
2 23558   51.6482 326.5861 0005938   67.0147   74.8047 15.60128403 15019
```

Explanations:

1. Record (data set identification): DSIDP is the data set ID parameter. The "B" is a quality flag (A = good, B = not so good, C = poor, X = unknown). "950725" is the date of determination and dissemination of the data set.

2. Record (state vector header): Identifier of the twoline elements generation program.

3. Record (1st line of element data): consists of 13 parameters: line-number (always 1), satellite ID, element classification (U = unclassified, C = confidential, S = secret), the last two digits of the launch year, the launch number of the year, the piece of launch, epoch year (last two digits of the year), epoch (day and fractional days of the year), first time derivative of the mean motion $\dot{n}$ in [rev/d^2], second time derivative of mean motion $\ddot{n}$ in [rev/d^3], drag term, ephemeris typ, element number, check sum (modulo 10, last digit in line).

4. Record (2nd line of element data): consists of ten parameters: line number (always 2), satellite ID, i [deg], Ω [deg], e, ω [deg], M[deg], n [rev/d], revolution number at epoch, check sum (modulo 10, last digit in line).

93

GLOSSARY

AFIT	Air Force Institute of Technology, USA
APD	Avalanche photo diode
ATSC	AlliedSignal Technical Services Corporation
CDDIS	Crustal Dynamics Data Information System
CoM	Center of mass correction
COSPAR	Committee on Space Research
CSTG	International Coordination of Space Techniques for Geodesy and Geodynamics
D-PAF	German Processing and Archiving Facility for ERS. D stands for "Deutschland" (Germany)
EDC	European Data Center
ERS-1	First European Remote Sensing Satellite
EUROLAS	European consortium of satellite laser ranging organisations
EVA	Extra vehicular activity, or space walks
FGAN	Radar facility of the Forschungsgesellschaft für angewandte Naturwissenschaften, Wachtberg-Werthoven, Germany
FWHM	Full width at half maximum
GFZ	GeoForschungsZentrum Potsdam
GSFC	Goddard Space Flight Center, Greenbelt, Maryland, USA
H/W	Hardware
IRV	Inter-range vector
KT	Kayser-Threde company, Munich, Germany
MCP	Micro channel plate
MOBLAS	Mobile laser ranging system
MTLRS	Mobile transportable laser ranging system
NASA	National Aeronautics and Space Administration, USA
NORAD	North American Aerospace Defense, USA
NPO Energia	see RKK Energia
PMT	Photo multiplier tube
POD	Precise orbit determination
Q/L	Quick-look
RKK Energia	Russian space corporation, formerly NPO Energia; Moscow, Russia
RMS	Root mean sum of squares
RNIIKP	Russian institute of space device engineering, Moscow, Russia
RSS	Root sum of squares
R&D	Research and development
SAO	Smithsonian Astrophysical Observatory
SAR	Synthetic Arperture Radar
SLR	Satellite laser ranging
S/C	Spacecraft
S/W	Software
USSpaceCom	US Space Command, formerly NORAD
w/o	without
WRMS	Weighted root mean sum of squares

GLOSSARY